Sondage de Canal SIMO à l'intérieur des bâtiments et formation de faisceaux numérique utilisant des techniques de traitement de signal à haute résolution et corrélateurs cinq-ports

A. Judson Braga

TELECOM PARIS
école nationale supérieure des télécommunications

Ecole Doctorale d'Informatique, Télécommunications et Électronique de Paris

Thèse

présentée pour obtenir le grade de docteur
Ecole Nationale Supérieure des Télécommunications
Spécialité : Electronique et Communications

Adoniran Judson de Barros Braga

Sondage de canal SIMO à l'intérieur des bâtiments et formation de faisceaux numérique utilisant des techniques de traitement de signal à haute résolution et corrélateurs Cinq-Ports

Soutenue le 18 septembre 2006 devant le jury composé de:

Ghais El-Zein, INSA Rennes	Président
Jean-François Diouris, Polytech. Univ-Nantes	Rapporteurs
Aziz Benlarbi-Delaï, IEMN Univ-Lille	
Glaucio Siqueira, CETUC-PUC Rio de Janeiro	Examinateur
Bernard Huyart, ENST Paris	Directeurs de thèse
Jean-Christophe Cousin, ENST Paris	

Ecole Nationale Supérieure des Télécommunications

TELECOM PARIS
école nationale supérieure des télécommunications

Ecole Doctorale d'Informatique, Télécommunications et Électronique de Paris

PhD thesis

Ecole Nationale Supérieure des Télécommunications
Communications and Electronics department

Adoniran Judson de Barros Braga

SIMO channel sounding in indoor environments and digital beamforming using high-resolution signal processing and Five-Port techniques

Defense date: 09, 18 2006

Committee in charge:

Ghais El-Zein, INSA Rennes	Chairman
Jean-François Diouris, Polytech. Univ-Nantes	Reporters
Aziz Benlarbi-Delaï, IEMN Univ-Lille	
Glaucio Siqueira, CETUC-PUC Rio de Janeiro	Examiner
Bernard Huyart, ENST Paris	Advisors
Jean-Christophe Cousin, ENST Paris	

Ecole Nationale Supérieure des Télécommunications

In memoriam

Dalva, Helena, Helba and Samuel Barros

Your respectable lives have marked my own and those of my future descendants.

Acknowledgments

I would like to acknowledge the help of many people during my study. First of all, Dr. Bernard Huyart, for helping to supervise me, providing resources and subjects, and offering direction and criticism; Dr. Jean-Christophe Cousin, for passing onto me many leads during the thesis; Dr. Xavier Begaud, for providing vital information about antennas; and Dr. Eric Bergeault, for his sense of humour in the laboratory.

Thank-you to my examiners: Dr. Ghais El-Zein, Dr. Jean-François Diouris, Dr. Aziz Benlarbi-Delaï and Dr. Glaucio Siqueira, for managing to read the whole manuscript so carefully and offering me relevant comments and suggestions about my work.

In the RF and microwave laboratory: specially to Yem Van Vu, for being a wonderful partner during 3 years sharing doubts and successes; Sofia Martinez, for helping to do measurements in the last months of the thesis and being a good friend as well; Fernando Rangel, for giving me technical support and motivation when I was starting my PhD. Thank-you to my colleagues and friends: Ghalid Abib, Sara Chakra, Guillaume Neveux, Antoine Khy, Kaïs Mabrouk, Souheil Bensmida, François Ziade, Hajar Elarja, Ludovic Schreider, Akiko Kohmura, Alfred El Kik, Anne-Claire Lepage, Mohamed

Bahouche, Charif Mohamed, Haroun Romdane, Beatriz Garcia, Mohammed Vadhani and Ihssen Masri.

Thank-you to my friends at ENST who have made Paris a very special place over all these years: Pau Soler, Antonio Cipriano, Ioannis Krikidis, Carlos Palavicini, Joseph Topomondzo, Korinna Lenz, Maya Badr, David and Maria de la Rosa, Fausto Agis, Ghassan Kraidy, Anis Latiri, Sami Mekki, Ryan Mina, Hassan Teimoori, Richard Singama, Qing Xu, Sheng Yang, Chantal Cadiat, Ana Kosman, Lorna Monahan and Peter Weyer-Brown.

Special thanks to my Brazilian friends at ENST: Marcia Silva, Joao Negrão, Celina Takemura, Rodrigo de Souza, Daniel Souza, Denis Franco, Roberta Barros, Rex Medeiros, Eric and Joana Bouton, André Cardoso, Leocarlos and Ana Lima, for everything we have done together. I love you so much and I will take you with me in my heart wherever I go.

My friends outside work: Celso Ishida, Alejandra Mansilla, Fabiana Geraldine, Najla Benevides, Patricia Lira and Francisca Cartano. My roommates, Sergio Queiroz, Rodolpho Bastos and Eliana Bogea. From the church: Fred and Audrey Biancucci, Martial Kpochan, Tamara Imhof, and Laurette Dade. Thank-you for being truly friends.

Special thanks to my entire family and friends in Brazil, for their patience, loyalty and love. I would also like to thank my parents: Edilson and Lidia Braga, for creating an environment in which following this path seemed so natural.

And finally, thanks to God through Jesus for his sacrifice on the cross.

Résumé

Le développement de systèmes de communication mobile large bande demande une connaissance des caractéristiques du canal mobile comme celles du profil de puissance, l'angle d'arrivée et le décalage Doppler des signaux liés aux trajets multiples. Un sondeur de canal peut réaliser une caractérisation multidimensionnelle du canal à petite échelle afin de l'appliquer à la modélisation stochastique de canal ou à l'évaluation des performances d'un système de communication dans un environnement donné. Ce travail décrit la réalisation d'un sondeur de canaux de propagation SIMO (Single Input Multiple Output) à l'intérieur des bâtiments. Ses caractéristiques essentielles sont l'utilisation de réflectomètre cinq-port utilisé comme démodulateur homodyne de signaux RF et de techniques d'estimation à haute résolution comme MUSIC. Un système de formation de faisceaux qui peut réaliser un filtrage spatial pour de nombreuses applications est aussi implémenté utilisant la plupart de ces outils. Le réflectomètre cinq-port réalise une conversion directe des signaux RF et utilise un troisième mixeur de redondance pour diminuer la dépendance du système au déséquilibre de phase et amplitude de l'oscillateur local. La procédure d'estimation de la réponse spatio-temporelle du canal est basée sur les algorithmes MUSIC et lissage spatial sur deux dimensions (2D-

SS). Le traitement simultané des données sur les domaines de l'espace et de la fréquence nous permet l'estimation conjointe de l'angle d'arrivée et du retard des trajets multiples même en présence des signaux corrélés. La technique de tracé de rayons est implémentée afin de comparer les paramètres du canal calculés de façon déterministe avec ceux déterminés par le sondage de canaux.

Abstract

The development of wideband mobile communication systems requires a better knowledge of the characteristics of the mobile channel as described by its power delay profile, directions of arrival and Doppler shifts of scatterers. A channel sounder can perform a multidimensional small-scale characterization of channels for stochastic modelling or communication system evaluation, such as allowable data rates. The aim of the present study is to assemble a number of instruments that are able to perform the sounding of SIMO propagation channels in indoor environments. Direction finding and beamforming systems are also implemented by using most of these tools, in particular, the five-port circuit used as a homodyne demodulator of RF signals and high-resolution estimation techniques such as MUSIC. Five-port discriminators use a third redundant mixer to decrease the system dependency from the phase and amplitude unbalance of local oscillators. The directional angle resolved channel impulse response is jointly estimated in the angle and time delay domains by extending the MUSIC algorithm associated with the enhanced 2D-SS technique. The ray-tracing technique is implemented to compare channel parameters resolved deterministically to estimated parameters of an indoor propagation channel resolved by channel sounding. In regard

to the beamforming system, its performance is tested by measuring the bit error rate for a different number of antenna array elements. We demonstrate the ability of the proposed system to perform spatial filtering and provide higher gain and smaller BER in the useful signal direction even in presence of a strong interference level.

Contents

List of Figures

List of Tables

Résumé Étendu

INTRODUCTION

La demande croissante des services de communications sans fil large bande et la limitation du spectre fréquentiel engendrent un défi continu aux opérateurs de tels services qui cherchent à réduire le niveau des interférences des signaux et les pertes d'énergie dans l'environnenement de propagation, afin d'augmenter la capacité du système. Une des solutions est d'exploiter les propriétés spatiales, telles que la formation de faisceaux, les systèmes à multi entrées et multi sorties (MIMO), la diversité spatiale, etc.

Le succès de nouveaux systèmes dépend de la connaissance des phénomènes de propagation, ce qui justifie le besoin d'un sondeur de canal de propagation. Ceci permet de connaître les limites de capacité d'un système pour un environnement donné. Il est aussi utilisé pour aider la conception de techniques de diversité comme la diversité spatiale, la diversité de polarisation et des techniques d'antennes intelligentes. La connaissance de la réponse du canal de propagation, ce qui pratiquement consiste à établir un modèle, est aussi utilisée pour décider le type de modulation et des stratégies de codage et d'égalisation.

Du point de vue de la modélisation du canal, on distingue les modèles

stochastiques des modèles déterministes. Les premiers sont basés sur l'estimation des paramètres du canal par la mesure. Les deuxièmes sont obtenus par calcul comme par exemple la méthode du tracé de rayon. Des modèles stochastiques peuvent être établis à l'aide d'un sondeur de canal. Le sondeur peut être défini comme étant bande étroite ou large bande, monodimensionnel ou multidimensionnel dépendent des paramètres du canal qu'on désire estimer.

La contribution de cette thèse est la conception et la réalisation d'un sondeur de canal à une entrée et multiples sorties (SIMO), soit une antenne en émission et plusieurs antennes en réception, destiné au sondage à l'intérieur de bâtiments à la fréquence 2.4 GHz. Les caractéristiques principales de ce sondeur sont l'utilisation de la technique fréquentielle pas à pas (step CW) et une architecture parallèle en réception, c'est à dire que chaque antenne est associée à un récepteur homodyne de type réflectomètre cinq-port [1].

L'implémentation d'une plateforme expérimentale de formation numérique de faisceaux est aussi proposée, où le traitement de signal est réalisé en bande de base et non pas par de déphaseurs et atténuateurs RF, et des réflectomètres cinq-port sont utilisés à la place de démodulateurs classiques I/Q.

Caractérisation à petite échelle d'un canal de propagation variant dans temps

Les fluctuations à petite échelle d'un canal de propagation sont observées sur des petits intervalles de temps et espace de sorte que des variations à grande échelle peuvent être ignorées. Ces phénomènes proviennent du grand nombre d'obstacles et d'irrégularités du milieu de propagation, à travers de

mécanismes de propagation comme la réflexion, la diffraction et la diffusion.

La caractérisation à petite échelle du canal de propagation est très importante car les dispersions temporelles et fréquentielles sont les principaux responsables de la sélectivité en fréquence et de l'évanouissement rapide du canal. En supposant une distribution gaussienne des trajets multiples dans un canal stationnaire au sens large à diffuseurs non-corrélés (WSSUS), les paramètres variables dans le temps du canal de propagation sont aléatoires mais peuvent être représentés par leurs moyennes et écarts types dès que ces moments de premier et deuxième ordre soient constants pendant un petit intervalle de temps et de fréquence [2].

Les paramètres de dispersion et de corrélation d'un canal WSSUS peuvent être déduits en utilisant les fonctions de densité de puissance temps/retard $P_h(\Delta_t, \tau)$, Doppler/fréquence $P_G(\nu, \Delta_f)$, retard/Dopller $P_D(\tau, \nu)$ et la fonction d'autocorrelation temps/fréquence $R_H(\Delta_t, \Delta_f)$. Ces fonctions sont reliées par la transformé de Fourier comme la montre la Fig. 1.

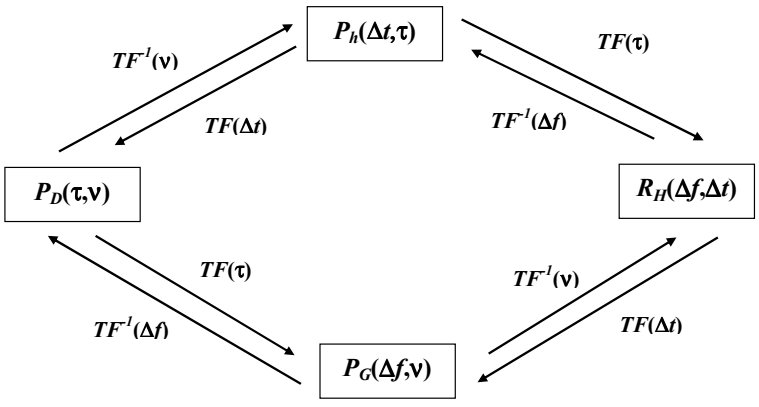

Figure 1: Fonctions caractéristiques d'ordre 2 d'un canal WSSUS.

Ces fonctions de densité de puissance peuvent être estimés par sondage

de canal. Le sondage d'un canal de propagation au domaine fréquentiel est réalisé par la mesure directe de sa fonction de transfert. Des réflectomètres cinq-port sont utilisés pour réaliser ces mesures au domaine fréquentiel.

Corrélateur à cinq portes

Comme le montre la Fig. 2, le système cinq-port en technologie micro ruban est composé d'un anneau interférométrique à cinq branches qui joue le rôle d'additionneur des signaux RF (Radio Fréquence) et OL, de trois détecteurs de puissance à diodes Schotky HSMS 2850 [3] et d'autant de filtres passe-bas (RC) à la sortie de chaque diode. Le rapport complexe $x(t)$ entre les deux ondes d'entrée (signal RF et signal OL) qui correspond à l'enveloppe complexe du signal RF modulé est défini comme étant une combinaison linéaire des puissances (P_3, P_4, P_5) des signaux à la sortie des filtres passe-bas. Autrement dit, $x(t) = a_{cal}P_3 + b_{cal}P_4 + c_{cal}P_5 + d_{cal}$, où a_{cal}, b_{cal}, c_{cal} et d_{cal} sont des constantes de calibrage. Ce rapport complexe $x(t)$ est déterminé après un traitement numérique.

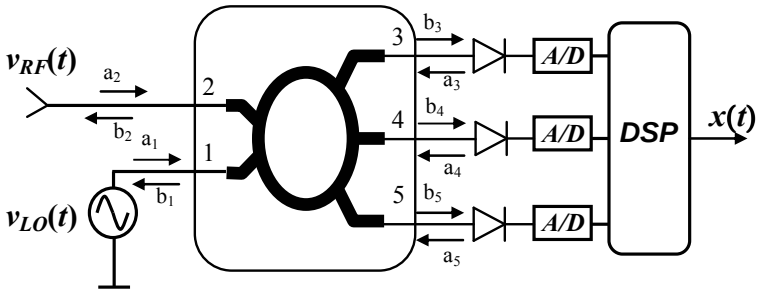

Figure 2: Réflectomètre cinq-port utilisé comme récepteur homodyne. $x(t) = \frac{a_2}{a_1} = I(t) + jQ(t)$.

Comme les systèmes I/Q, le réflectomètre cinq-port réalise lui aussi une

conversion directe des signaux RF, tout en profitant d'une redondance de mélangeurs et d'une base de 120° au lieu d'un système cartésien. Cette redondance entraîne que le système cinq-port est plus robuste au dépareillement de phase et amplitude de l'oscillateur local et, est par conséquence, moins sensible à l'EVM (error vector magnitude) par rapport aux systèmes I/Q [4].

Les inconvénients du circuit cinq-port sont surtout liés au détecteur de puissance. Un offset de tension DC apparait en sortie et ce phénomène est intrinsèque à ce démodulateur en raison du comportement quadratique des mélangeurs. Par ailleurs, un circuit résistif est utilisé pour adapter le détecteur de puissance ce qui entraîne une perte de sensibilité due à l'augmentation du facteur de bruit du système. Le circuit équivalent de sortie du détecteur de puissance [5] peut être modélisé comme la montre la Fig. 3, où R_V correspond à la résistance vidéo du détecteur.

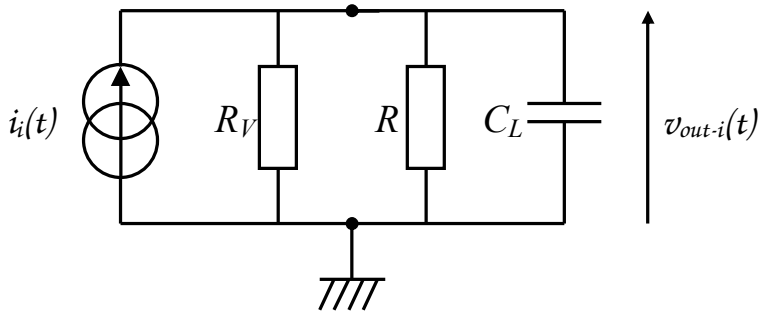

Figure 3: Le circuit équivalent de sortie du détecteur de puissance.

Les résisteurs R_V et R et la capacité C_L produisent un court-circuit au signal HF à la sortie de la diode se comportant comme un filtre passe-bas de premier ordre.

En utilisant des réflectomètres cinq-port pour mesurer le rapport com-

plexe entre les signaux d'entrée et de sortie d'un canal de propagation SIMO, la fonction de transfert associée à chaque récepteur est obtenue et traitée en bande de base pour l'estimation des paramètres du canal.

Traitement de signaux

Si l'on suppose des ondes RF arrivant sur un réseau linéaire d'antennes (voir Fig. 4) avec des directions d'arrivée données dans un milieu homogène et en faisant l'approximation de champ lointain, le modèle du signal peut être écrit par:

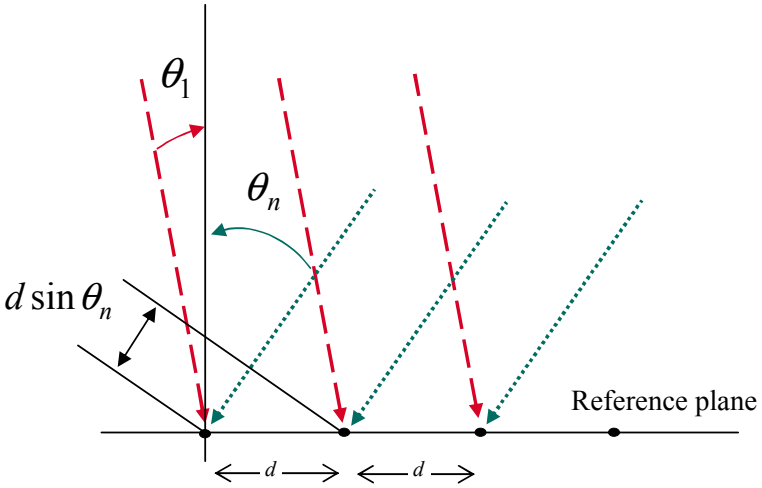

Figure 4: Modèle d'onde plane sur un réseau linéaire de capteurs.

$$x[k] = As[k] + n[k] \tag{1}$$

où $x[k]$ est le vecteur des enveloppes complexes mesurées à la sortie des capteurs, $n[k]$ est le vecteur bruit supposé spatialement décorrelé, $s[k]$ est le vecteur signal et A représente la matrice de concaténation des vecteurs directionnels qui portent les informations géométriques et électriques du système.

Le vecteur directionnel est composé par les rapports de phase entre les antennes du réseau et une antenne de référence et est calculé en fonction de la longueur d'onde λ, de l'angle d'arrivée θ et de la position des éléments dans l'espace.

$$a(\theta_n) = a_1(\theta_n) \left[1;\ e^{-j2\pi d \sin(\theta_n)/\lambda};\ \ldots\ ;\ e^{-j(M-1)2\pi d \sin(\theta_n)/\lambda}\right]^T \tag{2}$$

$(.)^H$ dénote le transposé, d est la distance entre deux éléments consécutifs, $a_1(\theta)$ est la réponse du premier capteur et M corresponds au nombre de capteurs.

On estime la matrice de covariance du vecteur des enveloppes complexes X_M composé de T échantillons.

$$\hat{R}_x = \frac{1}{T} X_M X_M^H \tag{3}$$

$(.)^H$ dénote le transposé conjugué complexe et X_M est la concaténation de T vecteurs $x[k]$. Après avoir réalisé une décomposition de $\hat{R}_x$ en valeurs propres λ_i et vecteurs propres e_i, l'une des techniques d'estimation de la direction d'arrivées (DDA) des signaux RF peut être appliquée.

Pour des signaux non-cohérents incidents sur le réseau, on peut séparer les vecteurs propres en deux sous-espaces. Les vecteurs propres associés aux valeurs propres les plus importantes représentent le sous-espace signal E_S, tandis que les vecteurs propres associés aux valeurs propres les plus faibles représentent le sous-espace bruit E_N. On suppose que ces deux sous-espaces sont orthogonaux et que le vecteur directionnel représente lui aussi le sous-

espace signal et donc il est aussi orthogonal au sous-espace bruit. Cette orthogonalité est la clé de la plus part de méthodes basées sur la théorie de sous-espaces, comme Min-Norm et MUSIC. L'algorithme MUSIC [6, 7] peut être représenté par :

$$P_{MUSIC}(\theta) = \frac{1}{a^H(\theta) E_N E_N^H a(\theta)} \tag{4}$$

Puisque le vecteur directionnel et le sous-espace bruit sont orthogonaux, la fonction $P_{MUSIC}(\theta)$ sera maximale dans la direction d'incidence des ondes et donc les pics identifiés dans le spectre MUSIC représentent les directions d'arrivées de ces sources. Par contre, en présence de sources cohérentes, cette orthogonalité n'est plus valable et une procédure de décorrelation est nécessaire.

Pour l'estimation du retard de propagation des trajets multiples τ, on doit réaliser une extension du vecteur directionnel au domaine de la fréquence. L'information du rapport de phase entre les enveloppes complexes correspondantes à différentes fréquences est utilisée en tant que vecteur temporel.

$$a(\tau_n) = a_o(\tau_n) \left[1, e^{-j2\pi\Delta f \tau_n}, ..., e^{-j2\pi(l-1)\Delta f \tau_n}, ..., e^{-j2\pi(L-1)\Delta f \tau_n}\right]^T \tag{5}$$

où $a_o(\tau)$ est la réponse du ton de référence (au domaine de la fréquence), Δf est le pas de fréquence entre deux tons consécutifs et L est le nombre de tons.

Lorsque qu'on exploite au même moment les deux domaines, le spatial et le fréquentiel pour une estimation conjointe de la direction d'arrivée et du

retard des trajets multiples, les données associés aux enveloppes complexes sont rangées de la façon suivante :

$$x[k] = [x_{1,1}, x_{1,2}, ..., x_{1,L}, x_{2,1}, ..., x_{M,L}]^T \tag{6}$$

Le modèle du signal reste le même, et le vecteur spatio-temporel sera une fonction de la variation de phase dans le domaine fréquentiel et dans le domaine spatial et doit être organisé comme le vecteur des enveloppes complexes $x[k]$. Le vecteur spatio-temporel peut être exprimé par:

$$a(\theta_n, \tau_n) = a_o(\theta_n, \tau_n)[a_{1,1}, a_{1,2}, ..., a_{1,L}, a_{2,1}, ..., a_{M,L}]^T \tag{7}$$

où $a_o(\theta_n, \tau_n)$ est la réponse du ton de référence au premier capteur du réseau et :

$$a_{m,\ l} = e^{-j\frac{2\pi f_l}{c}(m-1)\sin\theta_n} e^{-j2\pi(l-1)\Delta f\tau_n} \tag{8}$$

où c représente la vitesse de la lumière.

Après, une technique de séparation de sources doit être utilisée pour estimer les paramètres du canal de propagation, notamment, les angles d'arrivée et le retard des trajets multiples.

Une extension au réseau planaire d'antennes est aussi réalisée afin d'estimer les angles azimut et élévation des signaux RF. Pour une onde plane qui arrive au réseau d'antenne, le rapport de phase entre un point quelconque dans l'espace et les capteurs peut être exprimé par :

$$a_{yz} = e^{j(k_{y,n}+k_{z,n})} = e^{-j\frac{2\pi}{\lambda}[(y-1)\Delta y\cos\phi_n\sin\theta_n+(z-1)\Delta z\sin\phi_n]} \tag{9}$$

Cette relation de phase dépend de la longueur d'onde λ, des angles azimut θ et élévation ϕ et de la position des capteurs, où Δz et Δy représentent la distance entre deux éléments consécutifs dans les axes Z et Y, respectivement. Avec cette information, l'on peut construire le vecteur directionnel afin d'estimer les deux composants angulaires :

$$a(\theta_n, \phi_n) = a_o(\theta_n, \phi_n)[a_{11}, a_{12}, ..., a_{1M_z}, a_{21}, ..., a_{M_yM_z}]^T \tag{10}$$

Le modèle du signal, le rangement des données dans la matrice et le traitement des signaux restent les mêmes.

Pendant ces années de thèse on a implémenté des techniques de traitement de signal appliquées au sondage de canal. Pour la détection du nombre de sources la technique MDL [8] a été utilisée, et pour l'estimation de la puissance on a utilisé une technique proposée par Schmidt [7].

Afin d'estimer les angles d'arrivée et le retard des trajets multiples, on a implémenté les techniques MUSIC, Esprit et Fourier. Les deux premières techniques sont connues comme des techniques à haute-résolution mais elles ne sont pas robustes à la présence de sources corrélées. Par contre la technique Fourier reste robuste aux sources cohérentes mais sa résolution est faible.

Entre MUSIC et Esprit, selon quelques auteurs [9] et nos résultats de simulations, la technique ESPRIT présente une meilleure résolution, tandis que MUSIC apparait plus robuste aux erreurs de modélisation comme, par exemple, la mauvaise connaissance du vecteur directionnel.

Du point de vue du calcul, pour des systèmes à 2 ou 3 dimensions,

l'estimateur MUSIC prend beaucoup de temps pour calculer son spectre, ce qui est un désavantage. Dans le cas de sources cohérentes, le lisage spatial [10] ou la technique de Forward/Backward averaging [11] sont utilisés pour décorréler la matrice de covariance. Le lissage spatial s'est montré plus performant tandis que FB averaging s'est montré très utile pour des réseaux d'antennes de petite taille.

Résultas de mesure du sondeur de canal proposé

Le sondeur de canal proposé utilise de réflectomètres 5-ports et la technique fréquentielle de sondage, mode pas à pas. Une bande de 200 ou 400 MHz au tour de 2.4 GHz est utilisée pour exciter le canal de propagation. La fréquence d'échantillonnage est de 10 KHz et les techniques de lissage spatial, MDL et MUSIC sont utilisées pour l'estimation conjointe des paramètres du canal.

On peut voir dans le schéma électrique (voir Fig. 5) un générateur qui réalise un balayage en fréquence. Les signaux qui excitent le canal de propagation sont utilisés en même temps comme référence de l'oscillateur local.

Les signaux reçus par le réseau d'antennes sont amplifiés et transposés en fréquence par le système cinq-port. Puisque le cinq-port calcule le rapport complexe entre ses entrées, la réponse fréquentielle du canal pour chacune des antennes est mesurée. Pour convertir en numérique tous les canaux de sortie du cinq-port en utilisant peu de CAN, un système composé d'échantillonneurs bloqueurs est utilisé.

Après le traitement numérique des signaux mesurés, les paramètres du canal de propagations sont estimés.

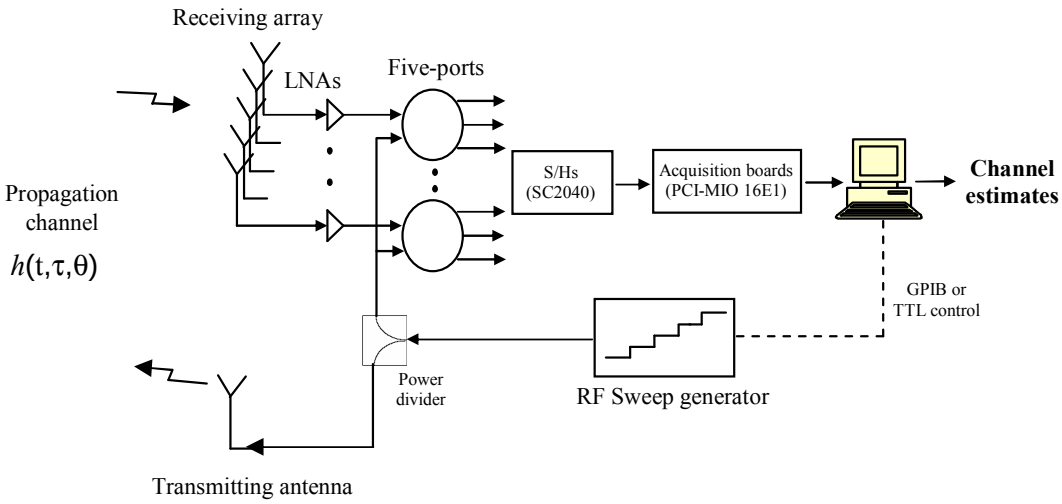

Figure 5: Sondeur de canal SIMO utilisant des réflectomètres cinq-port.

Avant la réalisation d'un sondage de canal, plusieurs essais ont été réalisés pendant ces années de thèse. De simulations avec de câbles et déphaseurs ont été réalisés pour vérifier la performance du système de mesure en estimant la direction d'arrivée et le retard de trajets virtuels. Puis, la complexité des systèmes a été augmentée.

Des antennes quasi-Yagi à faible couplage et large-bande sont utilisées. Les antennes sont placées en polarisation verticale et les LNAs sont intégrés sur le même substrat que les antennes. L'ouverture de l'antenne dans le plan H est plus importante que dans le plan E.

Pour estimer les angles azimut et élévation de 3 sources cohérentes à 2.4 GHz, un réseau planaire de 14 antennes est utilisé en réception. Le milieu est non-réflectif et le lissage spatial est utilisé avant MDL et MUSIC pour décorreler les sources.

Le spectre MUSIC et les valeurs théoriques sont affichés dans la Fig. 6.

Une erreur maximale de 4.5° est observée dans la coordonnée élévation. Cela est expliqué par la petite ouverture du réseau d'antennes dans l'axe vertical.

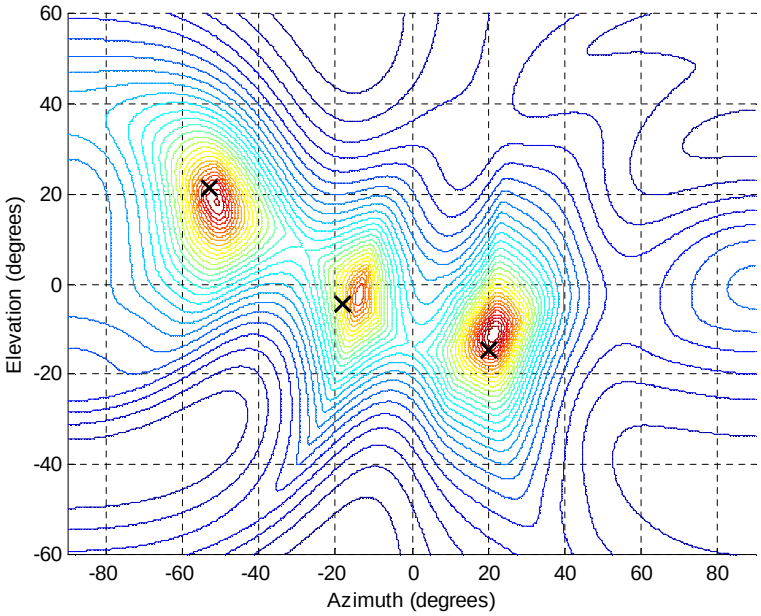

Figure 6: Estimation des angles azimut et élévation de 3 sources cohérentes. $M_y = 7$, $M_z = 2$, $sub_{M_y} = 4$ et $sub_{M_z} = 2$. $T = 100$. ($\times$) Valeurs theoriques. (Spectre) Valeurs estimés.

Pour l'estimation conjointe des angles azimut et élévation, le retard et la puissance des trajets multiples, un essai avec 4 signaux cohérents incidents sur un réseau planaire a été réalisé. 16 antennes et 101 points de fréquence sont utilisés pour une bande de 200 MHz.

Apres avoir calculé le spectre 4D a l'aide de MUSIC, un algorithme est implémenté pour chercher les pics du spectre. La Fig. 7 montre le profil de puissance, où le retard et la puissance associés à chaque trajet sont affichés. On remarque une estimation adéquate avec une erreur maximale de 2 dB.

Après avoir simulé le canal de propagation par des antennes directives,

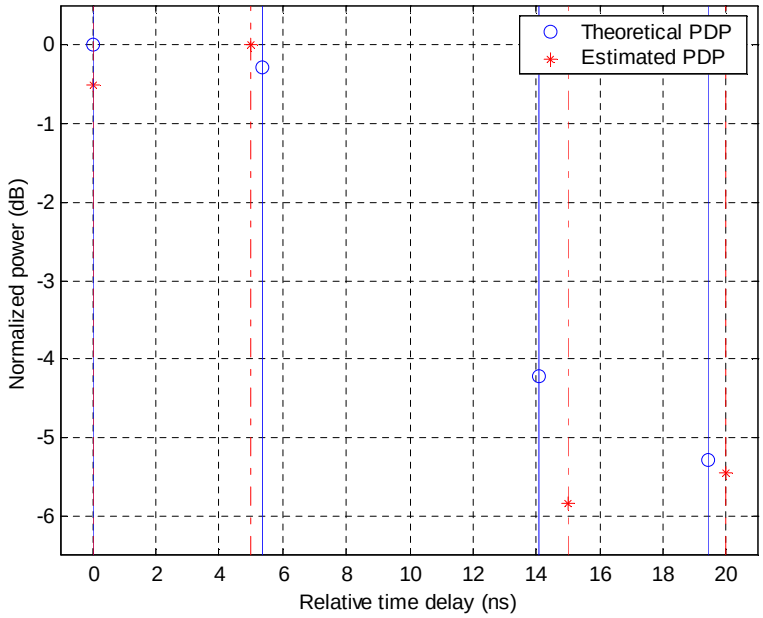

Figure 7: Le profil de puissance (PDP) d'un canal de propagation simulé par des antennes directives utilisant 3D SS et MUSIC. $M_y = 8$, $M_z = 2$, $L = 101$, $sub_{M_y} = 4$, $sub_{M_z} = 2$, $sub_L = 61$, $B_w = 200$ MHz, $T = 48$ échantillons. ($\circ$) Valeurs theoriques. (*) Valeurs estimés.

le sondage d'un canal de propagation à l'intérieur d'un couloir à l'Ecole Nationale Supérieure des Télécommunications est réalisé. Deux essais expérimentaux ont été réalisés. Pour le premier, l'émetteur était en vision directe avec le récepteur, tandis que pour le deuxième essai, l'émetteur n'était pas en vision directe avec le récepteur. Un émetteur directif a été utilisé et les murs du couloir sont métallisés.

Pour le premier essai, la connaissance de la géométrie nous a permit d'implémenter la technique de tracé de rayon, afin de comparer les résultas estimés avec les trajets théoriques.

Un réseau linéaire de 8 capteurs a été utilisé et 201 tons excitent le canal pour une bande balayée de 400 MHz. Les techniques de lissage spatial, MDL

et MUSIC sont utilisées. On peut observer dans la courbe d'estimation conjointe Direction d'arrivée/Retard (Fig. 8) une concordance entre les trajets estimés et théoriques. Par contre, pour chaque trajet estimé, deux trajets théoriques sont observés. Cela est dû à la limitation de résolution du système. On peut voir que l'un des trajets n'a pas été estimé. Cela est du au fait que des trajets ayant d'abord été réfléchis par le mur inférieur du couloir sont moins favorisés puisque l'émetteur directif pointe vers le mur supérieur. Puis, deux trajets à moins de 15° en azimut sont retrouvés. Cela peut être expliqué par des réflexions au sol ou bien au plafond.

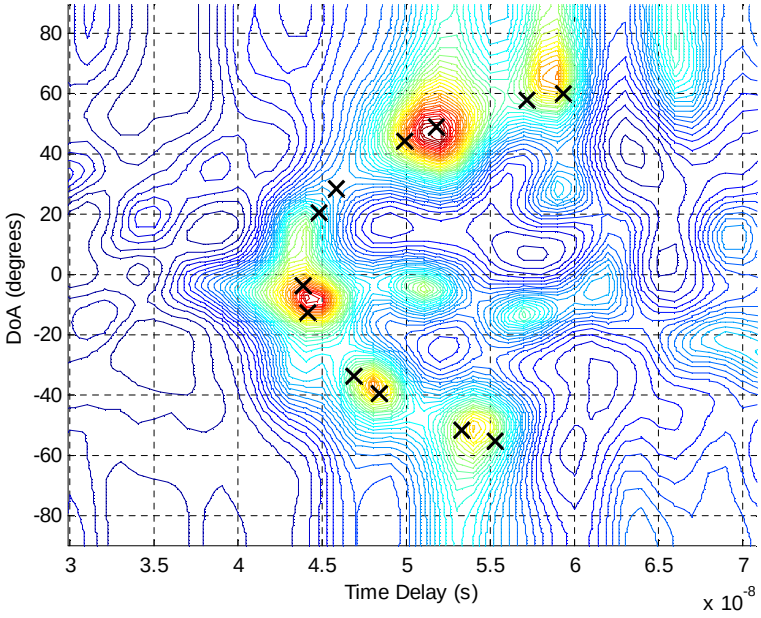

Figure 8: Cas LoS - Estimation conjointe retard/DoA des trajets multiples d'un canal de propagation utilisant 2D SS et MUSIC. $M = 8$, $L = 201$, $sub_M = 5$, $sub_L = 101$, $B_w = 400$ MHz, $T = 100$ échantillons.

Pour l'essai sans vision directe entre l'émetteur et le récepteur, la même configuration du réseau est maintenue. Le spectre MUSIC dans ce cas est

comparé au spectre Fourier. Huit trajets sont estimés par le sondeur de canal (voir Fig. 5.19 dans le Chapitre 5). En comparant les spectres MUSIC et Fourier, on observe une concordance entre les deux sur la distribution de l'énergie. Malgré la mauvaise résolution du spectre Fourier, il s'est montré très utile pour comparer la distribution d'énergie affichée par le spectre MUSIC et pour calculer la dynamique de puissance des trajets.

Système de formation de faisceaux

Les systèmes d'antennes intelligentes permettent de bien exploiter la dimension spatiale du canal de propagation mobile. Nous présentons un système de formation de faisceaux en réception en utilisant la technique cinq-port. La formation de faisceaux est faite en bande de base.

Le modèle de formation de faisceaux choisi suppose que le canal soit stationnaire donc il n'est pas nécessaire de faire les calculs en temps réel. Après l'estimation de la direction d'arrivée des signaux, le vecteur des constantes de pondérations $\hat{w}$ est alors calculé à partir de la relation entre la matrice des vecteurs directeurs des signaux d'interférence $\hat{A}_I(\theta)$, le vecteur directeur du signal utile $\hat{a}_{US}(\theta)$ et le vecteur distribution des sources de ligne $h(\varsigma)$ [12, 13].

$$\hat{w} = (\hat{A}_I(\theta)\hat{A}_I(\theta)^H)^{-1}\,[\mathrm{diag}(\hat{a}_{US}(\theta))h(\varsigma)] \tag{11}$$

Les DDAs sont calculées par l'algorithme MUSIC. Pour des signaux en bande étroite, la largeur du lobe principal ainsi que les niveaux des lobes secondaires du diagramme de rayonnement dépendent de la distribution des valeurs des constantes de pondération. Cette pondération est faite en

déplaçant les zéros de la fonction diagramme de rayonnement. La distribution $h(\varsigma)$ choisie est celle de Taylor [13]. Elle est définie en fonction de la position ς des éléments du réseau d'antennes par :

$$h(\varsigma) = S(0) + 2\sum_{u\in\Omega} S(u)\cos\left(\frac{2u\pi\varsigma}{Md}\right) \tag{12}$$

où $u = \frac{Md}{\lambda}\sin\Phi$, et $S(u)$ est le facteur spatial de champs lointain d'une distribution de Taylor défini par:

$$S(u) = \frac{\sin\pi u}{\pi u}\prod_{u\in\Omega}\frac{1-u^2/u_n^2}{1-u^2/n} \tag{13}$$

Les valeurs u_n représentent les η zéros de la fonction $S(u)$. Le vecteur de données $x[k]$ est pondéré par le vecteur $\hat{w}$, ce qui donne en sortie le signal pondéré $x_w[k]$:

$$x_w[k] = w^H x[k] \tag{14}$$

Trois antennes directives qui émettent respectivement le signal utile et les interférences sont orientées vers un réseau linéaire d'antennes de réception. Elles sont placées à 6 mètres de la base du réseau avec différents angles azimutaux. En réception, à chaque élément est connecté un LNA suivi par un cinq-port dont les signaux sont transposés. En bande de base, le DSP réalise la démodulation du signal et la formation de faisceaux. Finalement, les symboles QPSK sont retrouvés et comparés avec les symboles du signal utile en émission.

L'estimateur MUSIC est utilisé pour réaliser la détection des DDAs. La distribution des sources de ligne contrôle le niveau des lobes secondaires ainsi

que la largueur du faisceau. Pour contrôler le niveau des lobes secondaires, les antennes sont alimentées par d'amplitude différent e avec des niveaux plus importants au centre du réseau et moins importants aux extrémités du réseau.

Deux essais expérimentaux ont été réalisés dans un environnement qui n'entraîne pas de trajets multiples. Pour le premier, les puissances des signaux d'interférence à l'entrée du réseau d'antennes sont égales à -62,5 dBm et à -57,8 dBm. Celle du signal utile varie entre -67,5 dBm et -64,5 dBm. Les émetteurs localisés à 36° et à -31,5° par rapport l'axe orthogonal du réseau d'antennes du récepteur correspondent aux brouilleurs et celui à 18° correspond au signal utile. Les antennes quasi-Yagi utilisées assurent un faible niveau de couplage entre les éléments.

La Fig. 9 montre la courbe du taux d'erreur binaire (BER) en fonction du rapport signal sur interférence plus bruit (SINR) lorsque l'on utilise le modèle présenté en (11) et 7 éléments du réseau en réception. La courbe montre la bonne performance du système de formation de faisceaux présenté même en présence de fort niveau d'interférence.

Pour le deuxième essai expérimental, la même configuration est maintenue à l'exception des interférences qui sont enlevées. Le BER en fonction de la puissance du signal à l'entrée des antennes pour des réseaux de 1, 3 et 5 éléments est montré dans Fig. 10. Comme prévu, de meilleures performances sont observées pour des réseaux plus larges car le gain du réseau d'antenne est directement proportionnel au nombre d'éléments.

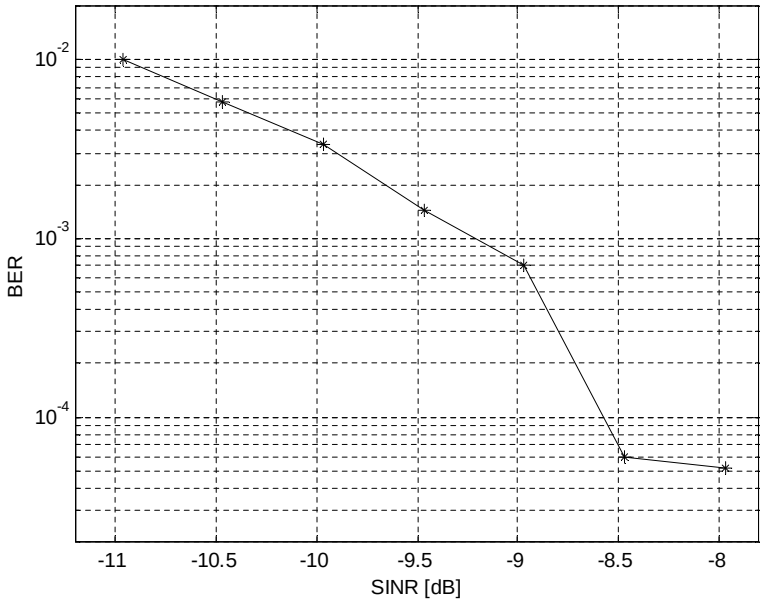

Figure 9: BER vs. SINR - Puissance des interférences: $P_{jam1} = -62.5$ dBm et $P_{jam2} = -57.8$ dBm. Puissance du signal utile : de -67.5 dBm à -64.5 dBm.

Conclusions

Dans ce travail, une plateforme expérimentale permettant l'implémentation des algorithmes de formation de faisceaux et la mesure du taux d'erreur binaire est présentée. Le filtrage spatial est réalisé en bande de base et des réflectomètres cinq-port sont utilisés au lieu de démodulateurs I/Q. La direction d'arrivée des signaux est bien estimée, et les courbes de BER montrent la performance du système, même en présence de forte interférence.

L'implémentation d'un sondeur de canal SIMO est aussi réalisée. Le sondeur est composé d'antennes quasi-Yagi, LNAs, réflectomètres cinq-ports et un système d'acquisition bande étroite. Afin de tester la performance du système de mesure, des essais sont réalisés dans un environnement non-

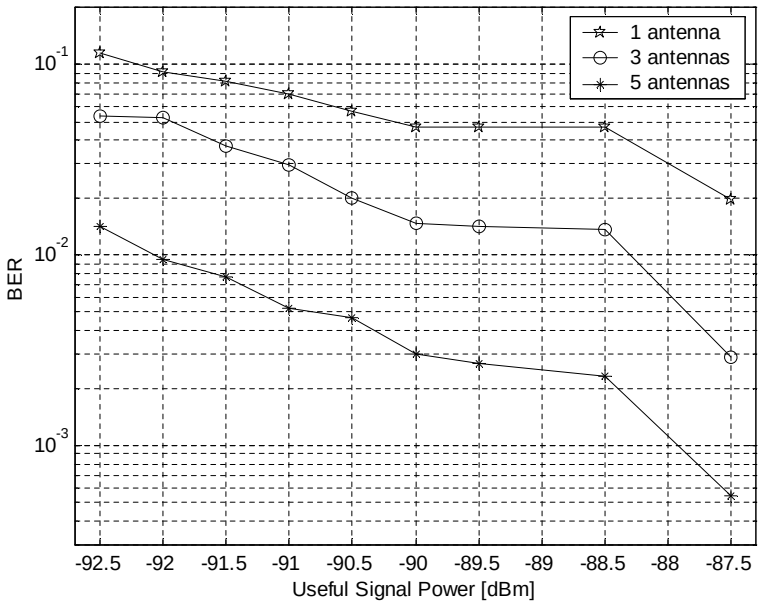

Figure 10: BER vs. Puissance du signal utile. 1, 3 et 5 capteurs. Puissance du signal utile : de -92.5 dBm à -87.5 dBm.

réflexif où les trajets multiples d'un canal de propagation sont simulés par des antennes directives. Le retard de propagation et les angles azimut et élévation des trajets simulés sont estimés de façon conjointe avec une précision adéquate.

Deux essais expérimentaux sont réalisés dans le couloir d'un bâtiment afin de sonder des canaux de propagation avec et sans vision directe entre l'émetteur et le récepteur. Les résultats d'estimation des paramètres du canal des deux essais ont été cohérents, malgré le coût de traitement de données élevé de l'estimateur MUSIC à deux dimensions. A cause du grand nombre de tons de fréquence, un nombre de trajets comparable au nombre d'antennes peut être estimé sans la connaissance préalable du nombre de sources.

Les contributions de ce travail sont résumées comme suit : 1) Rassemblement des techniques de traitement de signal et de circuits RF pour le sondage

de canal SIMO à l'intérieur des bâtiments et pour la formation de faisceaux ; 2) Estimation conjointe à N dimensions des paramètres d'un canal de propagation ; 3) Adaptation du système de conversion analogique-numérique pour des mesures bande étroite de canaux parallèles à faible coût.

Introduction

Since the early 1990s, the world has seen an explosive growth in the mobile telecommunication market. It is estimated there were 2.17 billion connections to mobile services in 2005 [14]. This corresponds to a third of the world's population, and the total will pass 3 billion in 2008. New wireless systems are expected to provide a data rate of over 10 Mbps in dense urban and indoor environments to support wideband services such as wireless sharing of large multimedia files.

The ability of operators to meet the expected high demands on network capacity using a limited licensed bandwidth is indispensable for the achievement of modern mobile systems. Substantial research efforts have been motivated by this challenge of increasing capacity, especially regarding spatial properties of channels, where major improvements still can be attained. Beamforming and MIMO communication systems, as well as schemes using RAKE receivers and systems exploiting spatial diversity, are examples of widely researched modern techniques with this intent.

The successful implementation of such systems implies detailed knowledge on the mobile propagation channel. This knowledge is available by means of the development of theoretical channel models and extensive channel mea-

surements.

If data is transmitted using wideband signals, small-scale characterization is needed to quantify frequency-selective fading, which can be calculated from the delay profile of the channel. Moreover, if the directional parameters of the channel are employed, as in smart antennas systems, they should also be included in the models. A channel sounder can perform small-scale characterization by estimating propagation channel parameters such as the power delay profile (PDP), direction of arrival (DoA) and Doppler-shift of multipath.

The aim of the present study is to assemble a number of instruments that are well known in the literature and able to perform the sounding of SIMO propagation channels in indoor environments. Direction finding and beamforming systems are also implemented by using most of these tools, in particular, the five-port circuit [1] used as phase/amplitude discriminator of RF signals and high-resolution estimation techniques such as MUSIC [6, 7].

The thesis has five main chapters. In Chapter 1, the propagation channel aspects are discussed. Physical mechanisms and the best known propagation models are reported, as well as channel representations for small-scale characterization. Techniques for measuring the channel impulse response (CIR) are presented, including the chosen scheme for the ENST channel sounder. Chapter 2 presents a detailed description of the estimation procedure of the DoA, time delay, power and number of RF signals. The high resolution estimation methods MUSIC and Unitary-Esprit are depicted, along with the Spatial Smoothing decorrelating technique. Extensions to more complex structures (2D and 3D) are detailed and simulation trials evaluate algorithm perfor-

mance.

Chapter 3 is dedicated to the five-port discriminator implemented in microstrip technology. Its operating principle is depicted, followed by the circuit implementation. A fitting procedure is used to correct baseband signals outside the linear zone of the power detectors and a calibration procedure used for compensating the five-port defaults.

In Chapter 4, the proposed digital beamforming system is presented. In order to maximise the gain of the system in the look direction and to attenuate strong interference, the baseband complex envelopes associated to the array elements are weighed according to a specific model. An abstract of the best known beamforming techniques, particularly LCMV and unconstrained beamformer, are studied. Taylor tapering is used for reducing the interference level by controlling the sidelobe level and beamwidth of radiation patterns.

In the last chapter of this study, the proposed SIMO channel sounder used for characterizing propagation channel in indoor environments is introduced. Measurements of simulated propagation channels are performed before sounding real channels. The measurement system is made up of quasi-Yagi elements that form the antenna array, low-noise amplifiers (LNA), five-port discriminators and a set of algorithms, such as Spatial Smoothing and MUSIC. Finally, the relevance of the results and guidelines for further work are discussed in the thesis conclusions.

This research study was developed at the *Radio Fréquences et Micro-ondes* (RFM) group of the communications and electronics department at *Ecole Nationale Supérieure des Télécommunications*, Paris-France.

This work was supported in part by the CAPES (*Coordenação de Aperfeiçoamento de Pessoal de Nível Superior*), Brazilian Government, Brasilia 70359-970, Brazil. This work was also supported by the COMELEC Department, GET - Telecom Paris, Paris 75013, France, UMR 5141, *Centre National de la Recherche Scientifique* (CNRS).

Chapter 1

The mobile radio propagation channel and measurement techniques

INTRODUCTION

In a wireless system, the transmitted wave interacts with the physical environment in complex ways, and arrives at the receiver along a number of paths, referred to as multipath. Multipath propagation results in the spreading of power in time delay and angle dimensions. Movement of the transmitter, receiver, or any other object in the physical channel also causes spreading in the Doppler frequency dimension [2] and makes the channel time-variant. The investigation of these propagation channel parameters and their effects on system performances is essential for channel modeling, as well as for designing and optimisation of communication systems.

A radio propagation channel is the propagation path between a radio

transmitter antenna and a receiver antenna. In telecommunications, the definition of a radio channel often covers the full interface with antennas. However, in the present work the radio interface covers a single channel input at the transmitter and the propagation channel itself, as well as multiple channel outputs at the receiver with some assumptions that simplify channel modeling. These suppositions encompass the neglecting of mutual coupling between array elements, bandlimited signals, wide-sense stationary uncorrelated scattering (WSSUS) propagation channel, far-field and homogeneous medium conditions and presence of additive white Gaussian noise (AWGN).

In this chapter, after presenting the conditions for modeling we address the physical phenomenon in radio propagation channels and mathematic representations of these channels. A brief state-of-the-art of existing channel models and channel sounding techniques are then introduced.

1.1 Modeling suppositions

In the present work some assumptions are used to simplify channel modeling, reducing the number of constraints and complexity. These assumptions take into consideration real conditions of measurement campaigns and their employed circuits and instruments. The neglecting of mutual coupling is justified since antenna array elements are carefully chosen to perform low mutual coupling levels. Although the polarisation of transmitted electromagnetic fields may change before reaching the receiver, this investigation is restricted to vertical polarisation, as both transmitter and receiver use only vertically polarized antennas. Antenna descriptions are given in Chapter 5.

1.1.1 Radio electric noise - Supposition of AWGN

Radio electric noise comprises the set of signals that carry no useful information and disturb the desired signal. These random disturbances are independent on the transmitted signal and are generated in the propagation medium (external noise) and electronic devices used in receivers (internal noise) [15, 16]. Atmospheric and galactic parasites as well as multi-user interference are some examples of external noise sources. The first two sources of noise can be ignored for high frequencies (from VHF band) [2], and the interference is thought to be bandpass filtered or well below the internal noise. Internal noise origins can be explained by the Brownian movement of electrons in the electronic components of the receiver and depend on temperature and signal bandwidth. This random and independent movement enables modeling internal noise as a Gaussian process according to the central limit theorem [17].

Other important source of noise in mobile communication is the noise radiated by electrical equipment of various kinds. The major source of impulsive noise is associated to the ignition system of vehicles. According to [2], the ignition noise level in urban environments is low for frequencies higher than the VHF band and can be ignored for higher frequencies.

Assuming the internal noise preponderant in the present system for multiple antenna applications, we may suppose that noise related to a given antenna is uncorrelated to the noise from each other antenna and thus corresponds to white noise in space. The noise used in the present work is therefore modelled as a white Gaussian random process with mean equal to

zero where noise is uncorrelated between samples in space, frequency and time domains. This white noise assumption is very important for the modeling of the covariance matrix of the measured data explained in Chapter 2.

1.1.2 Bandlimited sounding signals - Sinc(x) effects

Due to legal and technical reasons, the spectrum of a sounding signal must be restricted to a certain transmission bandwidth B_w. As a result, traditional Fourier-based methods used for impulse response reconstruction can lead to severe sidelobes that cause estimation confusion over a given resolution. Limiting the bandwidth of the frequency information is equivalent to filtering the transmitted signal by a sinc function that leads to sidelobe effects and resolution limitation. The use of high resolution techniques of time/frequency estimation is frequently used to overcome this limitation [18].

1.1.3 WSSUS condition

The electromagnetic waves impinging from different directions with different time delays are uncorrelated when the propagation channel (including transmitter and receiver) is in motion [2]. Over a period of time (or small spatial distances), the radio channel can be considered quasi-stationary or wide-sense-stationary uncorrelated scattering (WSSUS) [19]. The coherence time depends on the propagation channel and can be calculated according to different expressions [20].

In practice, the WSSUS condition is never fully satisfied. This can be

attributed to small scale fluctuations and reflections by the same physical object resulting in correlations between different multipath components. In reconstruction of channel impulse response (CIR) and direction of arrival (DoA) of multipath, this correlation can strongly affect the estimation robustness of some high resolution methods such as MUSIC, CAPON, ESPRIT, etc. [21].

1.1.4 Far-field condition

Theoretically, the angular field distribution in far-field regions is essentially independent of distance from the source. The far-field region is commonly taken to exist at distances greater than $2D^2/\lambda$ from the source, λ being the wavelength and D being the maximum overall dimension of the receiving antenna array.

For a plane wave impinging on an uniform liner array (ULA), the time delay between a reference antenna and the mth array element can be modeled as:

$$\tau_m^{far} = (m-1)\frac{d\sin\theta^{far}}{c} \tag{1.1}$$

where d is the inter-element spacing, c is the speed of light in air and θ^{far} is the far-field direction of arrival. This relation is illustrated in Fig. 1.1.

In reality, incident waves are never plane even in far zones and phase shift between consecutive array elements is non-linear. Near field approaches are more complicated and distance-dependent. Thus, far-field approximation is also considered for modeling simplifications.

The modeling suppositions depicted above are important for characteriz-

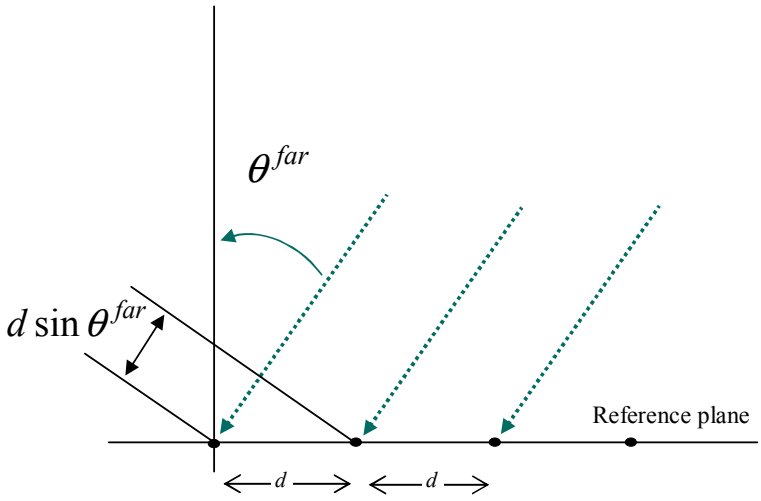

Figure 1.1: Phase shift between array elements of a plane wave signal impinging on a ULA.

ing the wave propagation medium between transmitter and receiver in realistic conditions of measurements. This zone is known as radio propagation channel.

1.2 Radio propagation channel

The interactions of waves with various objects in the environment, such as the ground, buildings, walls, vegetation, etc., are commonly referred to as propagation mechanisms [22]. Free space path loss, reflection/refraction, diffraction and scattering are the dominant propagation mechanisms. Supposing omni-directional antennas, the power radiated by the transmitting antenna spreads in all directions and thus only part of it can be collected by the receiving antenna. Free path loss quantifies this energy fraction by relating the transmitted power to the received power as a function of wavelength,

the distance between transmitting and receiving antennas and the effective aperture of the receiving antenna [23]. In reality, punctual antennas do not exist and, consequently, the radiation patterns of transmitting and receiving antennas must be taken into account.

Specular reflection takes place when a wavefront encounters a flat, infinite plane surface. The incoming wave splits up into reflected and transmitted (refracted) waves of which magnitudes can be computed from Fresnel's formula [20]. Even thought there are no perfectly flat infinite plane surfaces in reality, specular reflection is an adequate approximation if the surface is sufficiently large (at least 20 times the wavelength) and not too rough. If the surface has considerable roughness, reflected energy scatters in all directions instead of one specular direction.

When a radio wave encounters the edge of a large object, part of the wave appears to bend into shaded areas behind the edge. This phenomenon is called diffraction, and is more significant at lower frequencies, but not negligible at 2-3 GHz. Diffracted fields can be computed through the geometric theory of diffraction (GTD) [21] and uniform theory of diffraction (UTD) [24]. Scattering is a general interaction process between electromagnetic waves and an irregularly shaped object of small size in comparison to wavelength and results in the re-radiating of energy in many different directions. Trees, lampposts and irregularities in office walls may produce scattering.

From these propagation mechanisms, radio propagation channels can be characterised as a function of fluctuations of the received mean power for a given receiver displacement. Smooth fluctuations over tens of meters characterise large-scale phenomenon, whereas small-scale phenomenon is observed

when strong mean power variation is seen over short receiver displacement [20].

When the received mean power is mainly composed of refracted electromagnetic waves, the propagation channel undergoes a shadowing fading. Besides the path-loss mechanism, the shadowing fading appears as the main agent of large-scale phenomenon and may be related to a propagation flat fading. This smooth variation can be described as a log-normal distribution [20].

Small-scale fluctuations are observed over a sufficiently small period of time and spatial displacement so that large-scale variations can be ignored (Fig. 1.2). These phenomena emerge by means of some of the propagation mechanisms mentioned above, such as reflection, diffraction and scattering, as a consequence of a large number of obstructions and irregularities in the characteristic terrain of the propagation medium [25]. Multipath interaction at the receiver is performed in both constructive and destructive manners. The main consequences of this with regard to the signal are variations in the received signal envelope, random frequency modulation due to the dynamic variation of propagation conditions and signal time dispersion related to the time delay of echoes. This time dispersion may cause a frequency selective fading and will be reported in Section 1.2.4.

1.2.1 Propagation models

The optimisation and performance evaluation of radio communication systems require simulations with models including the relevant characteristics

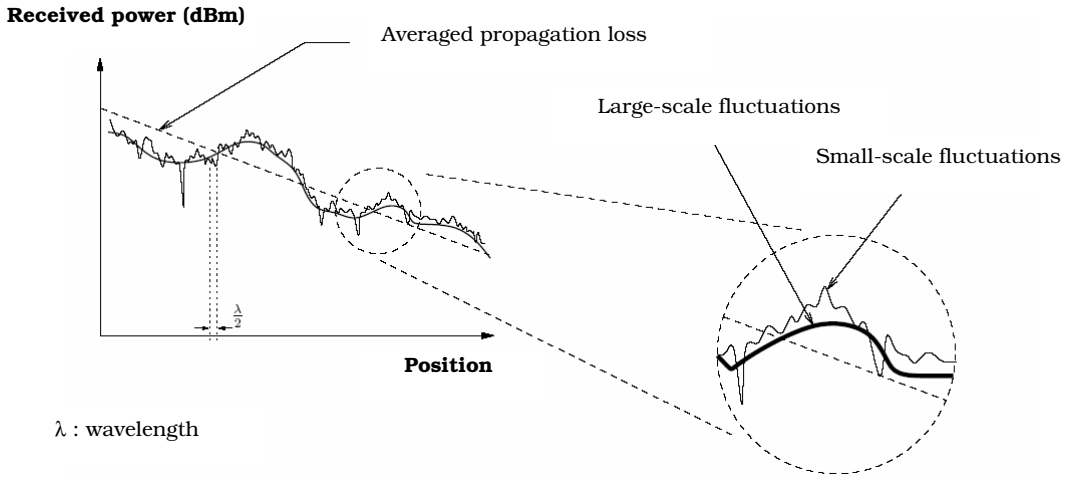

Figure 1.2: Received power as a function of position. Propagation loss, large and small scale fluctuations.

of the radio propagation in the effective environment. Propagation models can be classified as deterministic and stochastic models [26].

Propagation models are defined as "deterministic" if they are intended for reproducing the actual physical radio propagation process for a given environment (rural, urban, suburban, indoor etc). Examples are ray-tracing and stored measurement data that can be replayed any time. The former, as with other site-specific models, uses geometric knowledge of the scenario and techniques stemming from solving Maxwell's equations [27]. The ray-tracing technique launches rays from the transmitter in several directions, covering the full 4π solid angle and traces them until they reach the receiver or fall below a threshold field strength [28]. The latter concerns simplified path-loss models based on measurements (i.e. empirical models) and takes into account a number of physical properties of the environment. Probably the best-known path-loss model is the Okumura-Hata model, which is

based on measurements Okumura took in and around Tokyo and was later approximated by Hata using a set of formulas [29]. The model is valid in the frequency range from 150 MHz to 1000 MHz and takes into account the type of environment.

In view of the multitude of possible propagation environments, deterministic modeling of the channel parameters, such as ray-tracing, is not feasible and simplified path-loss models are limited for narrowband and unidimensional radio channel models. In contrast, all possible channel configurations can be reduced into a small number of classes described by a few parameters, such as DoA and time delay of propagation paths, when stochastic approaches are employed. From a systems engineering standpoint, this information enables the evaluation of modulation schemes, allowable data rates, diversity and smart antenna techniques, coding strategies and equalisation techniques; whereas from the standpoint of radio propagation modeling, such information allows us to relate multipath phenomena to local conditions, making possible a classification in terms of propagation environments.

Stochastic models aim to describe on average the propagation phenomena. Stochastic models are classified as geometry-based and non-geometric models. The term geometry-based refers to the fact that the modelled impulse response is related to the geometric location of transmitter, receiver, scatterers and other interacting objects. Their location is chosen stochastically in geometry-based stochastic channel models (GSCM). The model parameters need to be tuned to feature the characteristics of a given environment. This tuning is usually based on propagation channel measurements [30].

Non-geometric stochastic models describe paths from the transmitter to

the receiver by statistical parameters only, without reference to a physical layout. An example of stochastic non-geometric models is the extended Saleh-Valenzuela model [31] which operates on clusters of multipath components. The Saleh-Valenzuela model uses one exponentially decaying profile to characterize the power of a multipath cluster. The clusters made up of individual multipath components are then characterized by a second exponential decay with a steeper slope. The power delay profile is modeled by this double exponential decay model achieved with a Poisson process.

According to Zwick model [32], channel fading arises from relative phase changes of the combination of multipath components closely spaced in time of arrival. To model these changes, a geometric interpretation of the scenario is employed to describe the motion of the transmitter, receiver and scatterers. This mechanism is employed for all indirect multipath components in order to evaluate the channel fading.

Several models have been developed that include the time dispersion of the wideband channel by describing it as the sum of weighted and delayed Dirac responses. Examples of this type of model are the COST207 model [33] and its successors, the CODIT [34] and ATDMA [35] models. The weights are stochastic processes with parameters fitted to measurement data in different types of environments. Using a simpler approach, Braun [36] determines a statistical description of the radio channel in parameterised form by using estimates of the amplitudes, phases and time delays to evaluate a discrete simplified model. Once we have several "snapshots" of these estimates they can be averaged to derive the statistical description.

Other models encountered in the literature are known as analytical mod-

els, such as the Kronecker model, Weichselberger model, maximum entropy model, etc. Such models are usually used for MIMO channel characterisation and will not be discussed in this thesis.

As seen previously, measurements of the propagation channel parameters can be used to tune stochastic models in order to create variability within a fixed environment type. Other models directly use measurement data to derive the statistical distribution of a few parameters and consequently characterise the radio propagation channel. Further measurements including the DoA of multipath are required to verify the realism of existing ray-tracing models. In view of this, a channel measurement system or channel sounder is of great importance for actual radio channel propagation modeling.

Stochastic propagation models need to include only the received power and fading distribution for narrowband applications due to the complex summation of multipath amplitudes. For wideband applications, the time dispersion of the channel has to be included as well. Furthermore, with the introduction of techniques depending on spatial channel properties, angle information also needs to be modelled [37]. These parameters can be characterised from a system point of view by using a time-variant linear filter as the radio channel.

1.2.2 Time-variant linear filter

The radio propagation channel between a pair of antennas is illustrated in Fig. 1.3. The time-variant signal $s(t)$ is transmitted by the TX antenna and part of the transmitted energy reaches the RX antenna after propagating

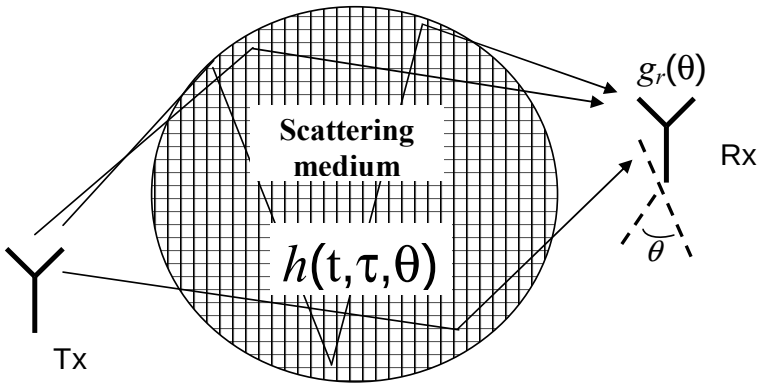

Figure 1.3: Radio propagation channel between a pair of antennas.

through different paths in the scattering medium. Thus, the signal at the output of the RX antenna consists of the sum of multiple attenuated, phase-shifted and time-delayed replicas of $s(t)$ and is given by [20, 38]:

$$y(t,\tau) = \sum_{n=1}^{N(t)} \{\alpha_n(t) e^{j\Psi_n(t)} \delta(t - \tau_n(t)) s(t)\} = h(t,\tau) \otimes s(t) \qquad (1.2)$$

In (1.2), $N(t)$ denotes the number of multipaths at a given time instant, and $\alpha_n(t)$, $\Psi_n(t)$ and $\tau_n(t)$ are the amplitude, phase and propagation delay corresponding to the nth path, respectively. $h(t,\tau)$ is called the time-variant channel impulse response (CIR) and $\otimes$ denotes the convolution operator.

When the spatial characterisation of the channel is required, the angle dependence from receiving signals is added to the filter model and the impulse response in (1.2) becomes:

$$h(t,\tau,\theta) = \sum_{n=1}^{N(t)} \alpha_n(t) e^{j\Psi_n(t)} \delta(t - \tau_n(t)) \delta(\theta - \theta_n(t)) \qquad (1.3)$$

The CIR can be decomposed into the integral of the directional angle

resolved CIR (DCIR) at the receiving antenna weighted by the complex radiation pattern of the antenna $g_r(\theta)$ over all directions of arrival θ in the azimuthal dimension [39]:

$$h(t,\tau) = \int_{\theta} h(t,\tau,\theta) g_r(\theta) d\theta \tag{1.4}$$

The input/output relation of the propagation channel described in (1.2) can be investigated in bandpass.

$$\tilde{y}(t) = Re\{y(t)e^{j2\pi f_o t}\} + n(t) \tag{1.5}$$

where f_o is the carrier frequency, $n(t)$ is a random noise and $y(t)$ can be expressed from (1.2). $\tilde{y}(t)$ is found after bandpass filtering and depending on its bandwidth and the channel mobility, a small scale characterisation is necessary.

1.2.3 Small-scale characterisation

The small-scale characterisation of the propagation channel is the main interest of this work, as temporal and Doppler dispersions are the most important agents of frequency selectiveness and channel fast fading, respectively. The complex CIR enables the joint survey of channel effects in time, time delay, frequency, Doppler frequency, space and direction of arrival domains. Representations are available with double dependence and can be easily associated to each other by means of Fourier transform [19].

The Doppler shift is obtained from the function $G(f,\nu)$. This is the

dual function of the channel impulse response $h(\tau, t)$ with respect to frequency and Doppler frequency domains. $G(f, \nu)$ enables direct identification of Doppler shifts in the frequency domain and is also useful for characterising the frequency selectiveness of the channel, as the spectrum of transmitted and received signals is directly related to $G(f, \nu)$.

$$Y(f) = \int_{-\infty}^{\infty} S(f - \nu) G(f, \nu) d\nu \tag{1.6}$$

$S(f)$ and $Y(f)$ are, respectively, the frequency domain representation of $s(t)$ and $y(t)$. $G(f, \nu)$ is related to the impulse response from a double Fourier transform:

$$G(f, \nu) = \int_{-\infty}^{\infty} \int_{-\infty}^{\infty} h(t, \tau) e^{-j2\pi f\tau} e^{-j2\pi\nu t} dt d\tau \tag{1.7}$$

The $H(f, t)$ function consists of relating the temporal signal at the filter (channel) output to the spectrum of the input signal:

$$y(t) = \int_{-\infty}^{\infty} S(f) H(f, t) e^{j2\pi ft} df \tag{1.8}$$

$H(f, t)$ is a channel transfer function and is obtained from the direct Fourier transform of $h(t, \tau)$.

$$H(f, t) = \int_{-\infty}^{\infty} h(t, \tau) e^{-j2\pi f\tau} d\tau \tag{1.9}$$

As $G(f, \nu)$, this function enables the survey of frequency selectiveness of the propagation channel. A time delay/Doppler frequency description is

performed by the function $D(\tau, \nu)$. This function is related to the impulse response as follows:

$$D(\tau, \nu) = \int_{-\infty}^{\infty} h(t, \tau) e^{-j2\pi\nu t} dt \tag{1.10}$$

The received signal at the filter output is:

$$y(t) = \int_{-\infty}^{\infty} s(t-\tau) \left\{ \int_{-\infty}^{\infty} D(\tau, \nu) e^{j2\pi\nu t} d\nu \right\} d\tau$$

$$y(t) = \int_{-\infty}^{\infty} \int_{-\infty}^{\infty} s(t-\tau) D(\tau, \nu) e^{j2\pi\nu t} d\nu d\tau \tag{1.11}$$

Unidimensional propagation channels can be represented by the four functions depicted above, namely, $h(t, \tau)$, $H(f, t)$, $G(f, \nu)$ and $D(\tau, \nu)$. These functions were proposed by Bello [19] and are related to one another as shown in Fig. 1.4.

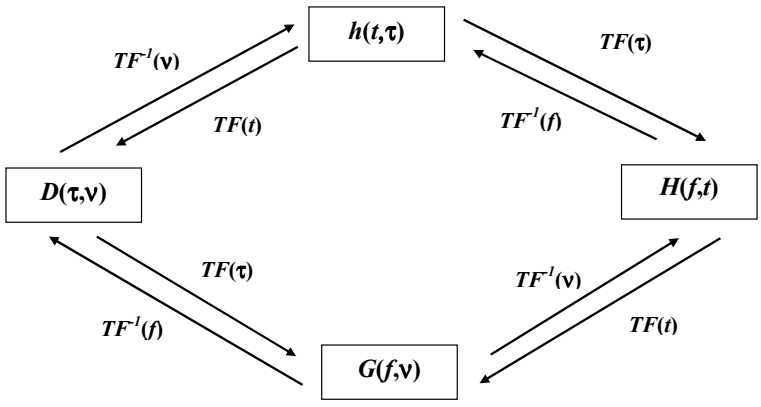

Figure 1.4: Representation of Bello's functions of a unidimensional propagation channel. TF means direct Fourier transform and TF^{-1} means inverse Fourier transform.

The Bello's functions represented above are limited to time-invariant channels. They are useful to characterize deterministic processes where function parameters are known. Since time-variant channels are random and the causes of that variability are numerous and complex, the treatment of Bello's functions becomes unrealistic. However, assuming a random behaviour of the channel (Gaussian distribution) and WSSUS (see section 1.1.3), the fading statistics do not change over a short interval of time and frequency, and thus the channel can be represented by the first and second moments of its scattering parameters.

In terms of the channel model composed of a number of elemental scatterers each producing delay and Doppler shift, WSS channels give rise to uncorrelated contributions from elemental scatterers if they produce different Doppler shifts, and US channels give rise to uncorrelated complex scattering amplitudes if the scatterers produce different time delays. The combination of both hypotheses (WSSUS) can be interpreted as follows: The time-varying transfer function is a bidimensional wide sense stationary process over an interval of time and frequency. The autocorrelation functions are as follows:

$$R_h(t,\tau;t',\tau') = \delta(\tau'-\tau)P_h(t'-t,\tau)$$

$$R_H(t,f;t',f') = R_H(t'-t,f'-f)$$

$$R_G(f,\nu;f',\nu') = \delta(\nu'-\nu)P_G(\nu,f'-f)$$

$$R_D(\tau,\nu;\tau',\nu') = \delta(\tau'-\tau)\delta(\nu'-\nu)P_D(\tau,\nu) \tag{1.12}$$

The presence of the unit impulse $\delta(.)$ means that contributions of elemental

scatterers are uncorrelated in the domain under study. $P_h(\Delta_t, \tau)$, $P_G(\nu, \Delta_f)$, and $P_D(\tau, \nu)$ are the time/delay, frequency/Doppler and delay/Doppler cross power spectrum density, and $R_H(\Delta_t, \Delta_f)$ is the time/frequency autocorrelation function. These functions are related to one another using the Fourier transform as illustrated in Fig. 1.5. Using these functions, the dispersion and correlation parameters of a WSSUS channel can be deducted.

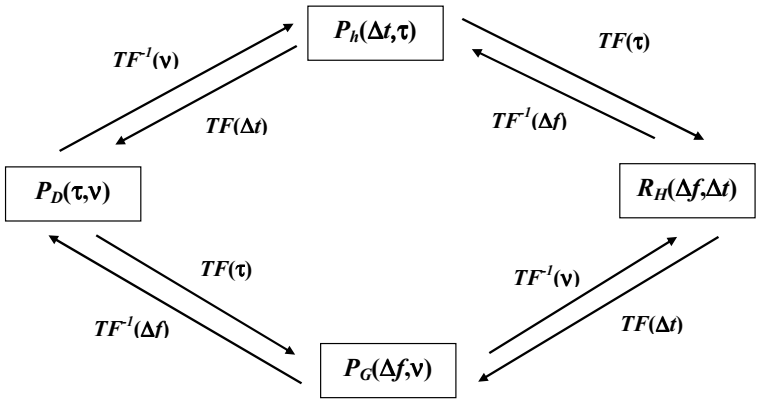

Figure 1.5: Second moment characteristic functions of a WSSUS channel.

When an antenna array is involved, a multidimensional propagation channel can be characterized in the angle domain, which is specifically related to DoA of RF signals in the present case. The function $V(\theta, f)$ contains DoA (azimuth) information that is dual to the spatial information $M(m, t)$ (antenna location) by means of classical Fourier-based spectral analysis [18].

$$V(f, \theta) = \int_{-\infty}^{\infty} M(m, t) e^{-j2\pi f t} dt \tag{1.13}$$

$M(m, t)$ describes the impulse response of the medium between a reference antenna and the other elements. This impulse response is only dependent

on the problem geometry, i.e. propagation conditions (homogeneous medium and far field) as well as location of sources and array elements. It does not depend on the nature of the input signal and can be modeled as (1.1).

Angular characterisation can be also evaluated through the examination of channel mobility and Doppler shift. The Doppler shift ν_n can be related to the velocity component v in the radial direction by $v = \lambda\nu_n$ and the direction of arrival can be calculated from the spectral values of the Doppler-shifted signals [40]. Parson [2] shows the RF power spectrum in Doppler shift domain as a function of DoA using different scattering models.

Other propagation channel representations have been developed in recent years. Guillet [41] present mathematic representations relating polarisation components of both transmitted and received signals, transmitter and receiver positions, the direction of departure (DoD) and direction of arrival (DoA) of RF signals. The author proposes equivalent equations relating one another by means of Fourier transform in which physical phenomena, transverse plane waves and polarisation properties are taken into account. This type of approach is not of interest in the present work.

1.2.4 Time dispersion parameters

Time dispersion in propagation channels may cause in wideband signals the effect of a symbol to spread to adjacent symbols when the RMS delay spread of the channel is large. The resulting intersymbol interference (ISI), degrades the performance of the communication system. The knowledge of coherent bandwidth B_c and use of equalization techniques minimize the effect of ISI

[20]. The equivalent effect of ISI in frequency domain is the Frequency Selective Fading which is observed when the coherence bandwidth is smaller than the bandwidth of transmitted signal [25].

Furthermore, the mere fact that the received signal strength changes over short time/distance due to multipath (small-scale fluctuations) causes channel flat fading even in narrowband signals. Time dispersion depends only on the relative amplitude of multipath components and their corresponding time delay, and is commonly represented by the RMS delay spread. The mean excess delay is as follows:

$$\bar{\tau} = \frac{\sum_{n}^{N} a_n^2 \tau_n}{\sum_{n}^{N} a_n^2} = \frac{\sum_{n}^{N} P(\tau_n)\tau_n}{\sum_{n}^{N} P(\tau_n)} \tag{1.14}$$

where a_n, τ_n and $P(\tau_n)$ are, respectively, the relative amplitude, time delay and power of the nth path. The RMS delay spread can be evaluated using:

$$\sigma_\tau = \sqrt{\bar{\tau^2} - \bar{\tau}^2} \tag{1.15}$$

where

$$\bar{\tau^2} = \frac{\sum_{n}^{N} a_n^2 \tau_n^2}{\sum_{n}^{N} a_n^2} = \frac{\sum_{n}^{N} P(\tau_n)\tau_n^2}{\sum_{n}^{N} P(\tau_n)} \tag{1.16}$$

Typical RMS delay spreads is on the order of microseconds for outdoor environments and nanoseconds for indoor [42]. If the coherent bandwidth is defined as the bandwidth over which the frequency correlation function is

above 0.9, then the coherent bandwidth is approximately [20]:

$$B_c \approx \frac{1}{50\sigma_\tau} \tag{1.17}$$

If the frequency correlation function is above 0.5:

$$B_c \approx \frac{1}{5\sigma_\tau} \tag{1.18}$$

The physical mechanisms and phenomena found in propagation channels are studied in order to characterise the radio interface between transmitting and receiving antennas. The need for small-scale characterization for wideband systems motivates the implementation of a channel sounder in this work.

1.3 Channel sounding and measurement techniques

As seen above, the measurement of channel parameters is needed to predict communication system performance and limits, which enables the evaluation of modulation schemes, maximum data rates, smart antenna techniques, equalisation and coding techniques. From a modeling point of view, stochastic models use such information to relate multipath phenomena to local conditions.

The best choice of measurement method depends on the type of environment, type of channel (unidimensional or multidimensional in transmission

and/or reception) and if the communication system is narrow or wideband (which determines whether multipath characterisation is needed). The multipath characterisation of a SIMO propagation channel for only indoor environments is the aim of the present work.

Channel impulse response can be directly measured in time domain or estimated from the channel frequency response by applying IFFT over the chosen frequency band. A CIR ($h(\tau, t)$) is theoretically represented by Dirac impulses $\delta(t)$ shifted in time over different time-delays. In practice, it is impossible to obtain an ideal Dirac in the channel input. Thus, several methods are employed to measure $h(\tau, t)$ of a radio channel by approximating the impulse function. These techniques are based on time or frequency domain measurements and are classified as follows:

- Direct impulse measurement technique
- Pseudo noise (PN) sequence measurement technique
  - Direct correlation
  - Sliding correlation
  - Convolution matched-filter
  - Wideband acquisition (Spread Spectrum)
- Frequency domain measurement technique
  - Chirp
  - Step
  - Multi frequency

Depending on the type of environment to be characterised, high time-resolution is demanded which is directly proportional to bandwidth of the transmitted signal. Another important parameter in channel sounding is the period of time between successive snapshots. This period decides the maximum Doppler bandwidth and thus, the possibility of sounding WSSUS channels. As the sampling frequency depends on both parameters (bandwidth and sampling period), there exist a trade-off between system cost and maximum Doppler bandwidth (especially for PN sequence techniques). Besides the bandwidth-dependent resolution in time delay domain, the reduction of sampling period results in growth of bandwidth of the transmitted signal which increases the needed bandpass of acquisition board and consequently its cost. On the other hand, the reduction of bandwidth affects the measurement time and thus the maximum frequency shift.

For frequency domain techniques, another important parameter of measurement is the minimum sweep-time of the RF signal generator. As the frequency response is measured in the time domain, the RF signal generator must guarantee sweeping over all frequency points (tones) in a shorter period than the coherent time of the propagation channel. This generator constraint limits the allowable environment type for using this technique. In contrast, a narrower bandpass for acquisition boards is required when frequency domain techniques are used.

1.3.1 Time domain techniques

Despite existing in different forms, time domain techniques are based on one common point: the transmitted signal has a wider band compared to frequency domain techniques. Several methods have been developed according to this principle. We present the most-cited sounding techniques in the literature, beginning with direct impulse sounding, which was first used by Young and Lacy [43] at 450 MHz in 1950.

Direct impulse sounding

The goal is to transmit an impulse RF signal and to observe its different echoes in reception. In reality, the impulse generator is switched on for a short period of time, thereby exciting the propagation channel. Direct detection of CIR is then performed by demodulating the complex envelope of the received RF signal. An envelope detector followed by a digital oscilloscope can be used instead of the homodyne demodulator, but the Doppler spectrum is not evaluated in this case [20]. The operation principle of this measurement technique is shown in Fig. 1.6. $s(\tau)$ represents the transmitted pseudo-impulse, where T_c and T_p are respectively the time resolution and impulse period. The latter defines the maximum measurable distance or time delay of the channel (without ambiguity). $h(\tau)$ represents the real CIR, while the power delay profile (PDP) corresponds to the measured CIR information, where τ_n and p_n are the time delay and relative power of the nth path.

The system realisation is simple. The PDP is quickly obtained with no signal processing efforts, using an RF switch, a signal generator and an

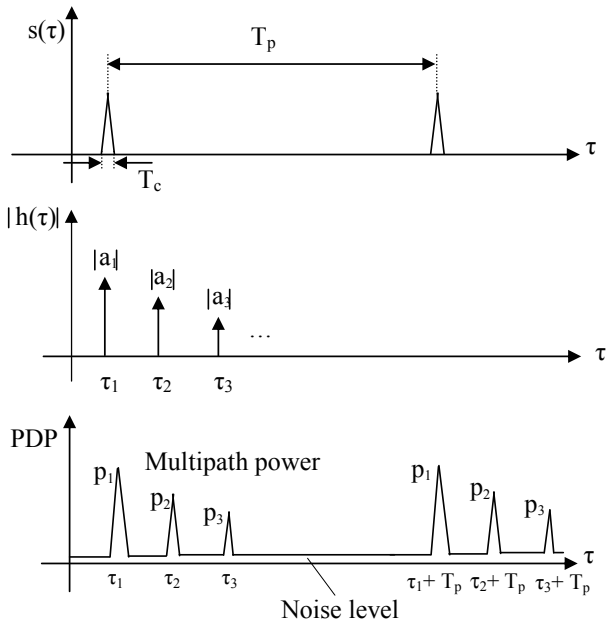

Figure 1.6: Operating principle of the direct impulse technique.

impulse generator. As a result, good resolution can be obtained with fast measurement time. The drawbacks of this technique are the need for a fast RF switch and impulse generator as well as a wideband acquisition board in reception. Besides, the impulse generator must support a very high peak power to guarantee the high dynamic range of the system. The fact that the system is wideband in transmission as well as in reception makes it more sensitive to noise and interference from other systems, which limits its dynamic range.

An alternative solution to alleviate the acquisition system is proposed by Rieser [44] (Virginia Polytechnic Institute). The sampling swept time delay short pulse (SSTDP) technique performs a sliding acquisition in the time domain in order to reduce the number of snapshots and, consequently, the

sampling frequency of the analogue-to-digital converter (ADC).

Direct correlation technique

This technique [45, 46] uses a white noise sequence $n_s(t)$ to excite the radio channel. The code is modulated onto the carrier frequency and transmitted across the channel. Some distance away, a receiver demodulates the signal and performs the correlation between channel output and an identical white noise sequence $n_s(t-\zeta)$ delayed by ζ seconds. The correlator is made up of a mixer followed by an integrator. The cross-correlation between the channel output and the white noise delayed in time is as follows:

$$R_{yn}(t,\zeta) = \int_0^\infty h(t,\tau) E\left[n_s(t) n_s^*(t-\zeta)\right] d\tau \tag{1.19}$$

Assuming the code with only real values, the conjugation of the second element in the expectation operator may be neglected and thus, (1.19) may be represented as a function of the autocorrelation between the two white noise variables $R_{nn}(\zeta)$. Thus:

$$R_{yn}(t,\zeta) = \int_0^\infty h(t,\tau) R_{nn}(\zeta) d\tau = \int_0^\infty h(t,\tau) N_0 \delta(\zeta) d\tau$$

$$R_{yn}(t,\zeta) = N_0 h(t,\zeta) \tag{1.20}$$

where N_0 is the power spectrum density of the white noise. The ζ values that maximize R_{yn} are used to determine a response proportional to the CIR. In fact, the replica of the white noise is not feasible, thus a pseudo noise (PN)

sequence with a maximum length linear shift register (MLSR) is used instead, as it has similar autocorrelation proprieties to a white noise process.

The HUT (Helsinki University of Technology) channel sounder [47] uses the direct correlation technique to estimate CIR. It performs complete spatial characterisation thanks to a spherical antenna array. However, this spherical geometry and the employed estimation method (Beamforming) lead to low resolution in the angle domain, even for the joint time delay/DOA estimation.

Sliding correlation

As with the previous technique, the sliding correlator channel sounder [48, 49, 50] clocks the PN sequence at very high frequencies to fill a wireless channel with noise-like content. After transmitting and channel filtering, a receiver demodulates the signal and performs the "sliding correlation". Contrary to the direct correlation technique, the received PN code with frequency f_t is mixed with an identical PN code clocked by the receiver at a slightly slower frequency f_r. Because this frequency shifting, the received sequence slides past the slower receiver-generated code in time. When the faster code slides past the slower code such that they are momentarily perfectly aligned, auto-correlation between the sequences will be very large. A series of alignments due to the multipath environment will generate a series of triangular peaks in the cross-correlation (integrator output). This effectively is the impulse response of the channel. At the correlator output, the signal is as follows:

$$R_{yn}(t,\tau) = \int_0^\infty h(t,\tau) E\left[n_s(t) n_s^*(t - \frac{f_r}{f_t} t)\right] d\tau \tag{1.21}$$

Since the sequence has only real values, the expectation term in (1.21) is the autocorrelation between received and receiver-generated codes $R_{nn}\left(\frac{f_r}{f_t}t\right)$. Thus, $R_{yn}(t,\tau)$ becomes:

$$R_{yn}(t,\tau) = \int_0^\infty h(t,\tau) R_{nn}\left(\frac{f_r}{f_t}t\right) d\tau \tag{1.22}$$

After the CIR reconstitution, the channel frequency response may be found by computing its Fourier Transform. Fig. 1.7 shows the block diagram of both the correlation and sliding correlation techniques, which differ from one another in only the clock frequencies of the codes. $n_s(t)$ is the transmitted code whereas $n'_s(t)$ represents the receiver-generated code.

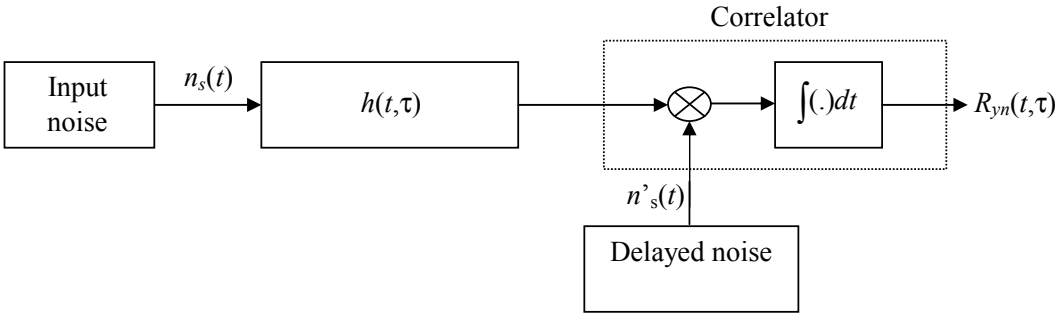

Figure 1.7: Block diagram of correlation-based techniques.

This technique enables a time scale increase (or frequency compression) corresponding to a factor k_s.

$$k_s = \frac{f_r}{f_t - f_r} \tag{1.23}$$

For example, if a channel sounder uses a PN code clocked to 100 MHz at the transmitter and 99.99 MHz at the receiver resulting in $k_s = 10000$, the

triangular peaks in the cross-correlation of 10 ns width are displayed with $100\mu s$ of width ($10 \times 10^{-9} \times 10000$).

This technique is of difficult realisation and the CIR reconstitution is complex. The time domain resolution depends on the clock period T_c, and even using frequency compression, which reduces the bandpass of the acquisition board, a high data rate PN generator is needed in transmitter. Furthermore, the PN code length must be larger than the maximum expected time-delay to assure a large dynamic range of time delay. This is critical when the factor k_s increases, since the observation window takes more time to be swept and measurements of WSSUS channels are therefore more difficult. Consequently, a trade-off between the frequency compression factor and channel coherence time is established.

In Table A.1 in Appendix A, a sliding correlation channel sounder of high dynamic range proposed by Haese [50] (INSA SC) is reported with other contemporary channel sounders.

Convolution matched filter (CMF) technique

Assuming a PN sequence $n_s(t)$ of maximum length L_s and width of code chip T_c, a filter of impulse response $h_{CMF}(t)$ is convoluted to the complex envelope $x(t)$ of the demodulated received signal.

$$x_{CMF}(t) = x(t) \otimes h_{CMF}(t) = \int_{-\infty}^{\infty} x(\tau) h_{CMF}(t-\tau) d\tau \qquad (1.24)$$

where

$$h_{CMF}(t) = \begin{cases} \frac{1}{L_s T_c}\ n(L_s T_c - t) & \forall\ t \in [0, L_s T_c] \\ 0 & \text{otherwise} \end{cases} \tag{1.25}$$

By manipulating equations [51] and due to autocorrelation proprieties of PN codes [52], the signal complex envelope at the matched filter output becomes:

$$x_{CMF}(t) = h(t, \tau) \otimes R_{nn}(\tau) \tag{1.26}$$

where $R_{nn}(\tau)$ is the autocorrelation function of the PN sequence.

$$R_{nn}(\tau) = R_{nn}(-\tau) = \frac{1}{L_s T_c} \int_{-L_s T_c}^{0} n(t) n(t - \tau) dt \tag{1.27}$$

This measurement technique results in an increase of signal to noise rate (SNR) [53]. On the other hand, it is necessary to use a fast acquisition board, since the complex envelope is wideband.

Wideband acquisition technique

In this technique [54, 55, 56], the correlation between transmitted and receiver-generated replicas of the PN code is generally carried out by a DSP processor. Indeed, the DSP performs a convolution operation between the received signal and the reverse copy of the PN code. This technique is not susceptible for intrinsic non-linearities of matched filters allowing optimal performance of the matched filter and large dynamic range. However, the main drawback remains the same: the wideband complex envelope must be digitally

converted, which raises the system cost.

According to Cosquer [51] (INSA SC), non-frequency compression is not a problem, since the wideband acquisition board is of easy access, achieving a high performing channel sounder with a dynamic range of up to 60 dB. Wilson presents a similar technique [57], except the digital convolution between the received sequence and the transmitter generated code is performed in the frequency domain. The received baseband signal is transformed to the frequency domain before convolution. The outcome is retransformed to the time domain, resulting in the CIR estimation.

1.3.2 Frequency domain techniques

Most frequency domain techniques use narrow band signals to measure channel impulse response. Wideband channel response can be evaluated by using a sequence of multitones or a wideband frequency modulated signal to excite the channel. Thus, a domain transformation is used to estimate the CIR.

Step-mode technique (Multitones)

A vector network analyser (VNA) controls a synthesised frequency sweeper, and an S parameter test set is used to monitor the frequency response of the channel. The sweeper scans the frequency band under study through discrete frequency steps, transmitting a known signal level on Port 1 and monitoring the received signal on Port 2. These signal levels allow the VNA to determine the channel response over the measured frequency range, namely, the Transfer Function. This response is a frequency domain representation of the channel

impulse response and is converted to the time domain using the Inverse Discrete Fourier Transform (IDFT), producing a band-limited version of the impulse response. Fig. 1.8 presents the multitone channel sounder using a vector network analyzer and IDFT approach.

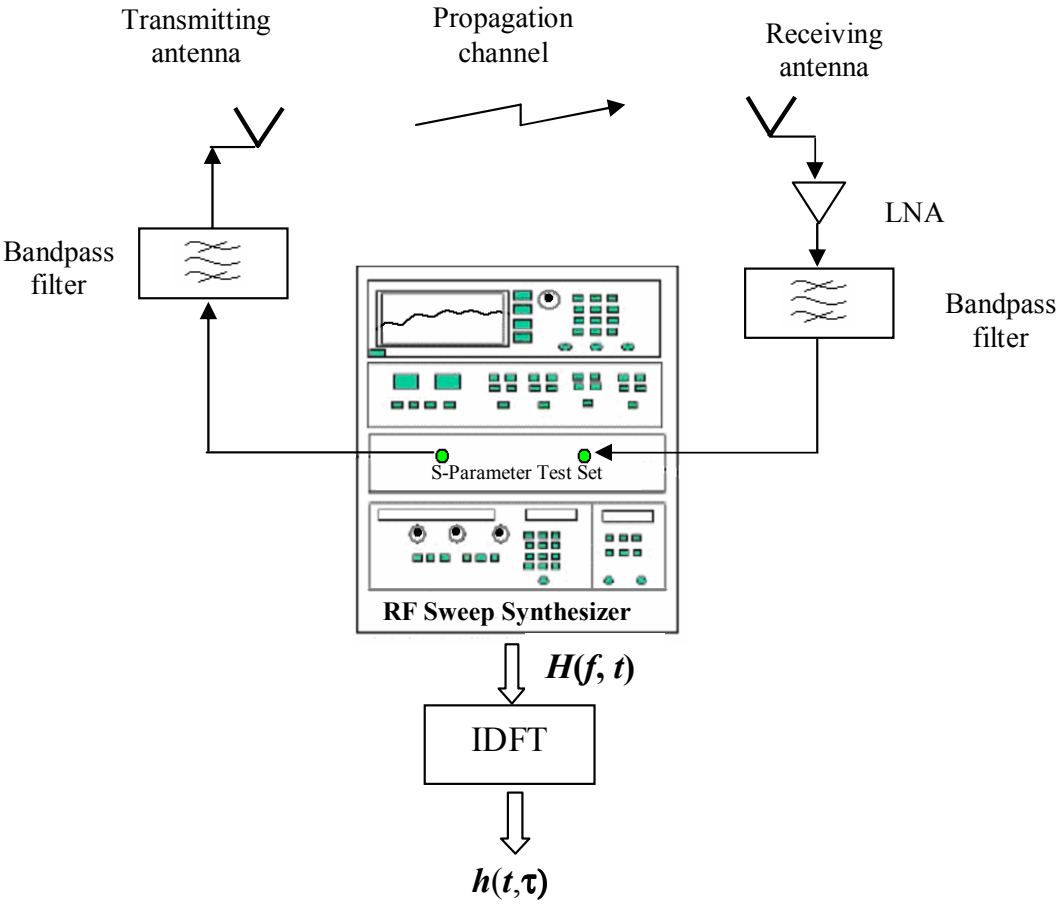

Figure 1.8: Multitone channel sounder.

The sweep bandwidth B_{sw} of the VNA impacts the time resolution $\Delta\tau$ of the impulse response as follows:

$$B_{sw} = \frac{1}{\Delta\tau} \tag{1.28}$$

For a given sweep bandwidth B_{sw} and number of frequency tones L, the frequency step Δf determines the unambiguous period T_p (observation window) of the measurement.

$$\Delta f = \frac{B_{sw}}{L} \tag{1.29}$$

$$T_p = \frac{1}{\Delta f} \tag{1.30}$$

Fig. 1.9 shows the time and frequency domains of transmitted signals and channel impulse response.

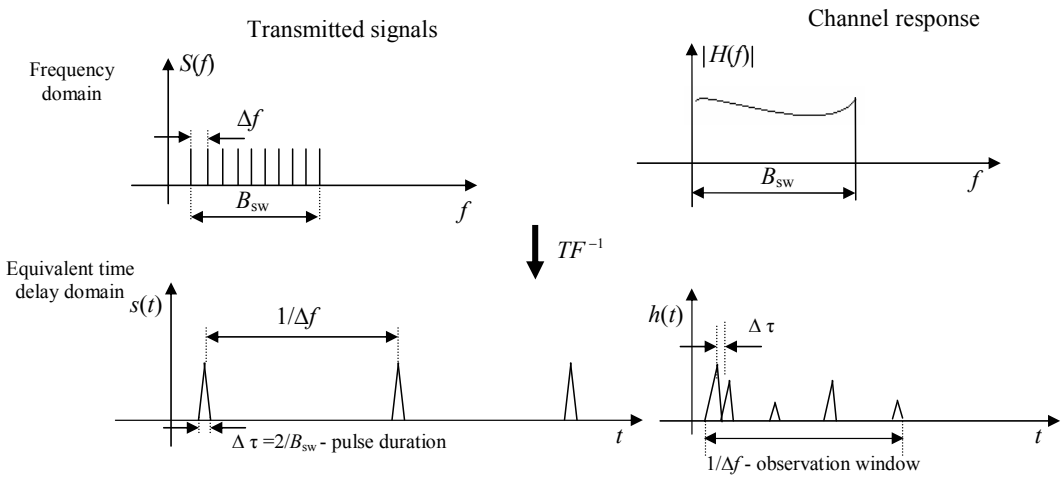

Figure 1.9: Frequency and time delay domain representations of the transmitted signals and channel response using step-mode technique.

The sweep time should be chosen such that the first and second moments of the channel scattering parameters remain invariant during the entire sweep (see Section 1.2.3). Assuming the bandwidth unchanged, a faster sweep time can be accomplished by reducing the number of frequency tones, which increases the frequency step size for a given sweep bandwidth B_{sw}. However, this reduces the excess delay range in the time domain. Thus, a balance be-

tween unambiguous range and measurement speed is required. The swept frequency domain system has been used successfully by Clavier [58] and Siqueira [59]. The ENST channel sounder [60] also uses this technique due to reasons explained at the end of section.

FMCW technique (Chirp)

The previous technique is sweep-time limited, which affects the maximum shift frequency that can be measured. An RF signal modulated in frequency [61] may be used to overcome this limitation, since frequency sweeping is performed much faster by the RF generator. As with the sliding correlation technique, this method is based on frequency compression, offering sampling frequency reduction and noise band reduction. The optimum compression factor must obey a trade-off between the Doppler frequency and the maximum bandwidth of the acquisition board. Salous presents the most important chirp channel sounders (UMIST) [62], [63] with SISO and MIMO parallel architectures.

Frequency domain correlation processing technique

Channel sounders using this technique, such as RUSK [64] and AMERICC [65], excite all frequencies simultaneously instead of sending frequency tones over time. This overcomes sweep time limits, thereby permitting measurements of high mobility.

The periodicity of the transmitted wideband signal determines the frequency spacing Δf and, consequently, the observation window. The desired bandwidth B_w is equal to the minimum sampling rate of the received signal

and specifies the number of frequency points $L = \frac{B_w}{\Delta f}$.

In Table A.1 in Appendix A, some channel sounders are depicted regarding a number of parameters, specifically, the type of channel architecture, sounding technique, carrier frequency, bandwidth, sampling frequency, signal processing technique, dynamic range, system resolution and whether joint spatio-temporal estimation is achieved. UWB channel sounders are not included in the list.

Concerning SIMO systems, channel sounder architecture is classified as parallel when system outputs are measured at the same time. Architecture is serial when only one measurement circuit is used to measure all output channels by means of a switch. Systems using virtual antenna arrays are also classified as serial architecture. Regarding the transmitter, the same reasoning is made for multiple input multiple output (MIMO) systems.

1.4 The chosen sounding technique

The step-mode technique can indirectly provide amplitude and phase information in the time domain; however it is hardware limited due to the rigorous synchronisation required between transmitter and receiver. The need for synchronisation limits the usable range of the system to short distance channel sounding measurement campaigns, such as indoor channel sounding. Moreover, the slowness of the generator frequency sweeping limits the Doppler range of measurement.

These limitations do not encumber the step-mode technique when indoor environment characterisation is considered, as the considered coherence time

is over 40 ms. Furthermore, the low cost of narrowband acquisition boards and simplicity of DOA models for narrowband signals make this technique an obvious choice for wideband characterisation. The high cost of vector network analysers can be alleviated by using homodyne demodulators, such as the five-port reflectometer shown in Chapter 3. ENST channel sounder [60] based on multitone technique and five-port reflectometer is presented in Chapter 5.

1.5 Conclusion

In this chapter, we addressed the need for precise knowledge of propagation channels, including physical phenomena and their mathematical representations, as well as the need for channel sounding to adjust stochastic models and validate deterministic models. Initially, some conditions are assumed to simplify channel modeling. Channel sounding techniques were then presented. The specification and performance of recent channel sounders are depicted in Table A.1. It seems that the frequency domain step-mode technique achieves the best trade-off between system cost and performance when SIMO channel sounding of indoor environments is considered.

Chapter 2

Estimation procedures and simulations

INTRODUCTION

In recent decades, high-resolution direction-finding (DF) techniques have been widely used in array signal processing. These techniques combine information from data collected from each array element with the known array geometry to estimate signal properties such as direction-of-arrival (DoA) and signal power. A number of these techniques have been extended to estimate channel impulse response (CIR) with better resolution performance than the classical Fourier approach [21]. An essential set of algorithms is presented for estimating the azimuth and elevation components of DoA, time delay and source strength for coherent and incoherent signals. These algorithms are used in Chapters 4 and 5 as tools to resolve channel parameters with high resolution. After describing the algorithms, their statistical performance is evaluated by means of simulation trials. In the last section, more realistic

simulations are performed to test the algorithm robustness under modeling errors.

2.1 Data model

If N plane waves from far-field sources impinge on a uniform antenna array (ULA) of $M > N$ elements at DoAs $\theta_1, \theta_2, ..., \theta_n, ..., \theta_N$ (see Fig. 2.1), the equivalent baseband data vector $x[k] \in C^{M\times 1}$ at time k is given by:

$$x[k] = As[k] + n[k] \tag{2.1}$$

where $A \in C^{M\times N}$ is the array response matrix formed by the concatenation of N steering (or mode) vectors $a(\theta_n) \in C^{M\times 1}$, and $s[k] \in C^{N\times 1}$ and $n_o[k] \in C^{M\times 1}$are the signal and noise vectors, respectively. $C^{\rho\times\varrho}$ denotes a matrix of complex values with ρ rows and ϱ columns. Noise is assumed additive, gaussian and white, with mean equal to zero. The steering vector corresponds to the antenna array response mentioned in Section 1.1.4 (1.1) and can be described as:

$$a(\theta_n) = a_1(\theta_n)\left[1;\ e^{-j2\pi d\sin(\theta_n)/\lambda};\ ...\ ;\ e^{-j(M-1)2\pi d\sin(\theta_n)/\lambda}\right]^T \tag{2.2}$$

$a_1(\theta_n)$ is the response of the first sensor, d is the inter-element spacing and λ is the wavelength.

A number of direction-finding (DF) methods use statistical information from observation data to extract DoA. The cross-spectral matrix is extensively used for this purpose [18] and, under the basic assumption that the

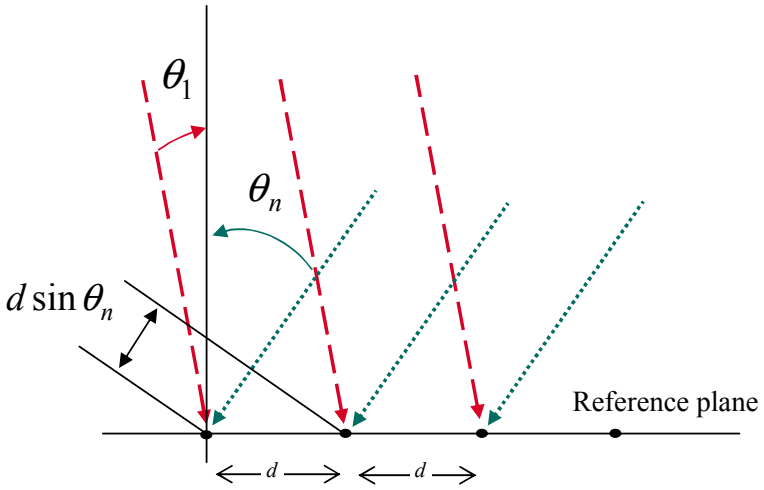

Figure 2.1: Plane-wave model on a linear array antenna.

incident signals and the noise are uncorrelated, can be represented as:

$$R_x = E\left\{x[k]x^H[k]\right\} = AR_sA^H + \sigma_o^2 I_M \quad \in \; C^{M\times M} \tag{2.3}$$

where $R_s \in C^{N\times N}$is the correlation matrix for the signal vector, σ_o^2 is the noise power at each array element and I_ϱ is a $\varrho \times \varrho$ identity matrix. Estimation over a finite duration of the cross-spectral matrix can be attained by computing the covariance matrix of the empiric data for T samples:

$$\hat{R}_x = \frac{1}{T} X_M X_M^H \tag{2.4}$$

$(.)^H$ denotes a complex conjugate transpose and $X_M \in C^{M\times T}$ is the concatenation of T data vector $x[k]$. The M eigenvectors e_i of R_x must satisfy:

$$R_x e_i = \lambda_i I_M e_i, \quad i = 1, 2, ..., M \tag{2.5}$$

where λ_i is the ith eigenvalue of R_x. The N eigenvectors related to the N strongest eigenvalues of R_x represent the signal subspace E_S, and the $M-N$ eigenvectors related to the $M-N$ weakest eigenvalues, with σ_o^2 noise power, represent the noise subspace E_N.

Since $R_x = AR_sA^H + \sigma_o^2 I_M$, we have $AR_sA^H e_i = (\lambda_i - \sigma_o^2)I_M e_i$. Clearly, when i corresponds to a noise subspace index, we must either have $AR_sA^H e_i = 0$ or $A^H e_i = 0$. That is, the eigenvectors associated to the weakest eigenvalues are orthogonal to the space represented by A.

Thus, the matrix A made-up of steering vectors can also engender the signal subspace that is orthogonal to the noise subspace. This orthogonality is the key to most subspace-based methods.

2.2 Estimation of DoA of incident signals

Most DF techniques can be classified into two main categories, namely, spectral-based and parametric approaches. In the former, one forms a spectrum-like function of the parameter of interest, for example, DoA. The locations of the highest peaks of the function in question are sought and then recorded as the DoA estimates. Parametric techniques, in contrast, offer a directly simultaneous estimate of all DoAs at the expense of increased computational complexity.

The main difficulty associated with spectral-based methods is that both computational and storage costs tend to increase quickly with the number of spatial samples (dimension of the antenna array).

Only the two most popular high resolution techniques will be depicted

in this section, namely, MUSIC and Unitary-ESPRIT, due to their relevant performance and contribution to DF system research in last twenty years. MUSIC is a spectral-based technique, while Esprit is classified as a parametric approach. Both are eigen-decomposition-based techniques and are considered consistent and statistically efficient [66].

Many other techniques are considered more efficient, such as WSF, IMP, Root MUSIC, SAGE , Matrix Pencil, etc [21, 66, 67]. However the complexity and constraints of such techniques discourage practical use in some cases. For WSF and IMP, for example, there are several parameters that need to be set subjectively by the user [9].

2.2.1 MUltiple SIgnal Classification (MUSIC) algorithm

The MUSIC algorithm [6, 7] uses the eigen-structure of the cross-spectral matrix as a basis for DoA estimation. The pseudo-spectrum $P_{MUSIC}(\theta)$ exhibits peaks in the vicinity of the true DoAs by relating the orthogonal signal and noise subspaces described in (2.2) and (2.5).

$$P_{MUSIC}(\theta) = \frac{1}{a^H(\theta) E_N E_N^H a(\theta)} \tag{2.6}$$

Compared to other high resolution techniques of low complexity, such as Capon and Min-Norm, MUSIC is considered more robust for modeling errors [68] when, for example, incident signals are non-plane waves. Huang [9] reaches the same conclusion comparing it to ESPRIT.

2.2.2 Unitary Estimation of Signal Parameters via Rotational Invariance Techniques (Unitary-ESPRIT) algorithm using TLS solution

The Unitary-ESPRIT algorithm [69, 70] assumes an antenna array made up of two identical translated subarrays. Their corresponding baseband signals form J_1 and J_2, as depicted in Fig. 2.2. M is the number of array elements

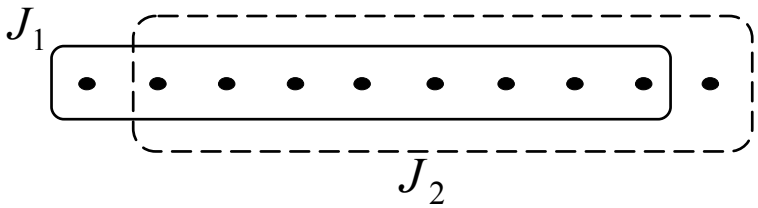

Figure 2.2: Subarray selection for a ULA of $M = 10$ elements (maximum overlap $\mu = 9$). Black dots indicate the elements of the vector x[k].

and μ is the number of elements in each subarray, respecting the condition $M \leq 2\mu$. Thus, we can define a pair of selection vectors centro-symmetric to one another, ie.,

$$J_2 = \Pi_\mu J_1 \Pi_M \tag{2.7}$$

where Π_ϱ is the $\varrho \times \varrho$ exchange matrix with ones on its antidiagonal and zeros elsewhere. These matrixes are used for estimating the spatial frequencies $\hat{k}_n$ explained below.

The complex-valued matrices X_M and $\hat{R}_x$ are mapped bijectively onto the real-valued matrices $\Psi(X_M)$ and $\Psi(\hat{R}_x)$ of the same size [71, 72]. The

real-valued matrix $\Psi(X_M)$ is as follows:

$$\Psi(X_M) \triangleq Q_M^H \left[X_M \quad \Pi_M X_M^* \Pi_T \right] Q_{2T} \quad \in \; C^{M \times 2T} \tag{2.8}$$

where $(.)^*$ denotes a complex conjugate and Q is the unitary matrix

$$Q_{2\nu+1} = \frac{1}{\sqrt{2}} \begin{bmatrix} I_\nu & 0_\nu & jI_\nu \\ 0_\nu^T & \sqrt{2} & 0_\nu^T \\ \Pi_\nu & 0_\nu & -j\Pi_\nu \end{bmatrix} \tag{2.9}$$

of odd order, whereas its equivalent of even order $Q_{2\nu}$ is obtained from (2.9) by removing the second row and second column from that matrix.

All computations can now be done with real-valued matrices. This forms the basis for the application of Unitary-ESPRIT. The first step using this technique is to estimate the real-valued signal subspace E_{S_Ψ} as the N dominant eigenvectors of $\Psi(\hat{R}_x)$. $\Psi(\hat{R}_x)$ is computed using (2.4) and $\Psi(X_M)$ as follows:

$$\Psi(\hat{R}_x) = \frac{1}{T} \Psi(X_M) \Psi(X_M)^H \tag{2.10}$$

The Unitary-ESPRIT algorithm is based on the solution Υ of the real-valued invariance equation

$$K_1 E_{S_\Psi} \Upsilon \approx K_2 E_{S_\Psi} \tag{2.11}$$

by means of Total Least Squares (TLS), where K_1 and K_2 are a special transformed matrix of J_1 and J_2 as follows:

$$K_1 = Q_\mu^H (J_1 + J_2) Q_M \tag{2.12}$$

Table 2.1: DoA estimates of 5 incoherent sources using ULA array.

Theoretical DoAs	MUSIC	ESPRIT
-78°	-77.9°	-78°
-30°	-30°	-30°
2°	2°	2.1°
13°	13°	13°
40°	40°	40°

$$K_2 = Q_\mu^H j(J_1 - J_2) Q_M \tag{2.13}$$

Thus, the estimation of the N spatial frequencies $\hat{k}_n$ is as follows:

$$\hat{k}_n = 2 \arctan(\lambda_n) \tag{2.14}$$

where the N λ_n represent the eigenvalues of Υ. Finally, the DoA estimate θ_n is determined via:

$$\theta_n = \arcsin\left\{ \frac{\lambda}{2\pi d} \hat{k}_n \right\} \tag{2.15}$$

A simulation trial intends to estimate the DoA of incident signals on a uniform linear array (ULA) with $d = \lambda/2$ using the MUSIC and Unitary-ESPRIT algorithms. 5 equipowered and incoherent sources with SNR of 10 dB and AWGN are totalled over 8 array elements. For all simulations, 500 snapshots of complex values are computed and the frequency of the narrow-band signals is set at $f = 2.4$ GHz. In Fig. 2.3, the MUSIC pseudo-spectrum is illustrated with five peaks in the vicinity of the theoretical DoA values represented by the dashed vertical lines. Table 2.1 displays DoA estimates in adequate agreement with theoretical values.

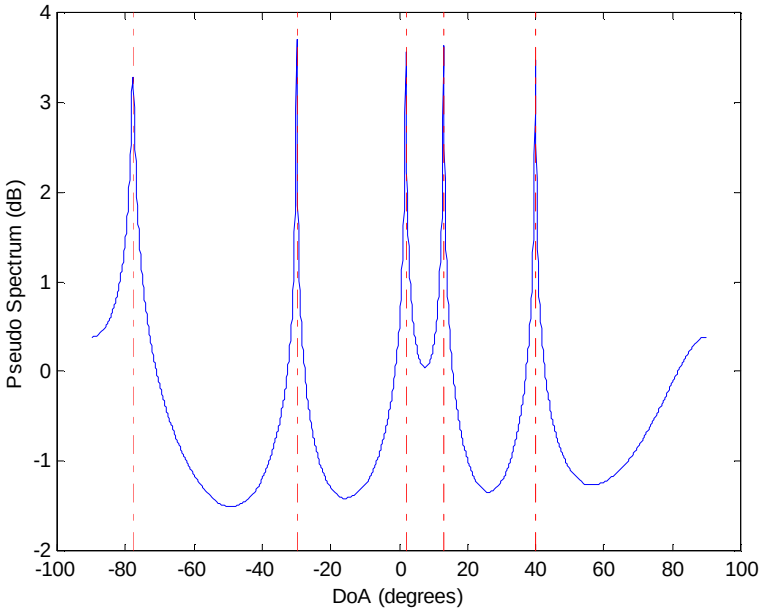

Figure 2.3: MUSIC pseudo-spectrum of a direction finding system using 1D array. 5 incoherent sources with $SNR = 10$ dB and $M = 8$.

2.2.3 MUSIC and ESPRIT algorithm performance

There are mixed opinions in the literature on ESPRIT and MUSIC algorithm performance. Stoica [73, 74] states that ESPRIT-based algorithms are significantly less efficient from a statistical standpoint than MUSIC in large samples. This is confirmed in [75, 73, 76]. On the other hand, Huang affirms that ESPRIT estimates with the TLS solution are more accurate than MUSIC estimates [9]. The author also reports that the MUSIC algorithm is not as sensitive to the model parameters when compared to ESPRIT. Thus, a small error may not lead to its defeat.

Depending on the number of array elements and the θ-step of the MUSIC spectrum, computing cost can be compromising when the MUSIC technique is used. This scenario worsens when 3-or-4-dimension spectrums must be

computed. However, Al-Ardi [77] reports a higher computing cost for the ESPRIT algorithm when an ULA array greater than 25 elements is used.

Ottersten [78] demonstrates that MUSIC estimates converge considerably slower to the limiting distribution than ESPRIT estimates. This means that ESPRIT estimates needs less snapshots to achieve theoretical values of DoA.

For a linear array in the presence of a single source, the bias increases as the source moves away broadside [79]. This is caused by the sinusoidal behaviour in (2.2), where errors in phase measurement become more critical for higher angles θ.

When white background noise in space domain (between the antennas) is not assumed, the model (2.3) is not applicable any longer and the DoA schemes perform differently. In the presence of coloured background noise, the performance of MUSIC is better than that of ESPRIT over a wide range of SNR [73]. Furthermore, Soon [76] states that MUSIC estimates are more sensitive to both sensor gain and phase errors, whereas ESPRIT depends only upon phase errors.

According to Huang [9], who simulated DF systems with 14 array elements and $d = \lambda/2$, the TLS-ESPRIT estimates can separate two sources definitely below 0 dB of SNR located at 2^o and -2^o. MUSIC can achieve the same estimation performance with SNR superior to 2 dB. According to Zhang, the resolution of a DoA system can be improved by increasing the inter-element spacing [80], thereby offering a larger antenna aperture at the expense of reducing the angular observation window.

The resolution property of MUSIC is further analyzed in [81, 82], which show how it depends upon the SNR, number of snapshots, array geometry

and separation angle of two closely spaced sources. This expression may be used to compare a high resolution method such as MUSIC to the classical Fourier approach that is widely used in the literature, especially for CIR estimation.

Many remarks and conclusions from the authors mentioned above may be extended to frequency domain processing, as the model used to describe the frequency domain is the same as that used to describe the space domain, with the exception of the mode vector, which is a linear function in the former, as will be seen in Section 2.7.

Assuming this model similarity, the MUSIC resolution $\Delta\tau_{MU} = \tau_1 - \tau_2$ for two temporally near sources may be determined by the Kaveh [82] approach:

$$SNR \approx \frac{1}{T}\{\frac{180(L-2)}{\pi^2 L}\left[1+\sqrt{\frac{\pi^2 T(\Delta\tau_{MU}B_w)^2}{15(L-2)}}\right](\Delta\tau_{MU}B_w)^{-4}\} \qquad (2.16)$$

where L is the number of frequency tones, T is the number of snapshots per tone and B_w is the bandwidth. According to Marple [83], the Fourier-approach resolution does not depend on SNR; it depends only upon the phase of incident signals, bandwidth and window used in the frequency domain. Depending on the phase of incident signals, constructive or destructive sidelobes are formed in the time delay domain, disturbing peak decisions and system resolution. The sidelobe level is 13 dB below the highest peak when one signal is incident and a rectangular window is used [68]. Under this condition, the Fourier approach resolution $\Delta\tau_{Fourier}$ comes close to the

reciprocal to the bandwidth B_w of the measurement system.

$$\Delta\tau_{Fourier} \approx \frac{1}{B_w} \tag{2.17}$$

Fig. 2.4 shows the resolution performance in the time delay domain as a function of the number of frequency tones for the classical Fourier method (DFT) using a rectangular window and the MUSIC algorithm according to (2.16). The number of samples T is 200 and the frequency step Δf is 2 MHz. The centre frequency is 2.4 GHz and the SNR varies from 3 to 27 dB. As Δf is constant, the increase of the number of frequency tones indicates the increase of the system bandwidth. As expected, the Fourier technique presents poor resolution in comparison to the MUSIC algorithm when a narrowband is swept.

Thus, we conclude that high-resolution techniques have better performance than classical Fourier methods. Comparing MUSIC to Esprit for ULA array processing, the former presents a better performance from a statistical standpoint, that is, it presents less variance over large samples, whereas TLS-Esprit is less biased and has better resolution. In contrast, MUSIC estimates seem to be less sensitive to modeling errors, such as near field condition and imprecise knowledge of the array geometry, when compared to ESPRIT.

2.3 Estimation of power

Once the directions of arrival of the N incident signals have been found, the matrix A becomes available and may be used to compute the parameters of

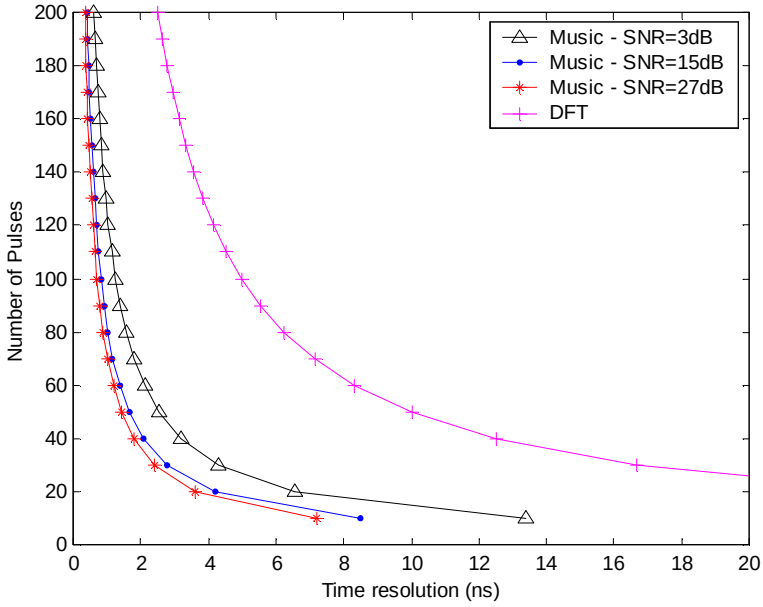

Figure 2.4: Time delay resolution as a function of the number of frequency tones for ToA estimation. MUSIC and DFT techniques are compared with SNR equal to 3, 15 and 27 dB.

incident signals. The solution for the R_s matrix is directly established from (2.3). That is, since $AR_sA^H = R_x - \sigma_o^2 I$,

$$R_s = (A^H A)^{-1} A^H (R_x - \sigma_o^2 I) A (A^H A)^{-1} \tag{2.18}$$

The elements of the correlation matrix R_s represent the power and cross-correlation between incident signals, including the radiation pattern effects of antennas. In Chapter V, power estimation of measured incident signals employs radiation pattern compensation in order to exclude such effects from the channel estimation.

2.4 Estimation of number of sources

In [7], Ralph Schmidt uses the dimension of the signal subspace to determine the number of incident signals by decomposing $\hat{R}_x$ into E_S and E_N. Perfect eigen decomposition is only possible for completely decorrelated incident signals and even the Spatial Smoothing technique cannot assure a $\hat{R}_{x_{SS}}$ matrix of full rank after decorrelating the coherent signals.

Minimum Description Length (MDL) [8] and the Akaike Information Criterion (AIC) [84] are reported as more reliable criterions for estimating the number of source. The MDL estimator [85] can be interpreted as a test for determining the multiplicity of the smallest eigenvalues. The solution is the number of sources γ that minimizes the following function:

$$P_{MDL}(\gamma) = T(M-\gamma)\log\left[\vartheta(\gamma)\right] + \frac{1}{2}\gamma(2M-\gamma)\log(T)$$

where

$$\vartheta(\gamma) = \frac{\frac{1}{M-\gamma}\sum_{i=\gamma+1}^{M}\lambda_i}{\sqrt[M-\gamma]{\prod_{i=\gamma+1}^{M}\lambda_i}}$$

2.5 Decorrelating coherent signals

Coherent signals arriving from different directions can be modelled as delayed and attenuated replicas of the same signal, whereas incoherent signals are linearly independent. Statistically, coherent signals are correlated and incoherent signals are uncorrelated, thereby influencing the statistical performance of the cross-spectral matrix. $\hat{R}_x$ is rank deficient and the eigen-decomposition fails to evaluate signal and noise subspaces when coherent

signals are incident. As a natural result of a multipath propagation effect, such a phenomenon is not uncommon.

Techniques such as Spatial Smoothing (SS) [10] and Forward-Backward (FB) averaging [11] attempt to restore the full rank property of the cross-spectral matrix $\hat{R}_x$ in the presence of coherent signals by inducing a random phase modulation. The idea of the SS technique is to split the $\hat{R}_x$ matrix into a number of overlapping subarrays (see Fig. 2.5) and to average them. In Fig. 2.5, $r_{i,j}$ is the correlation between the array elements i and j.

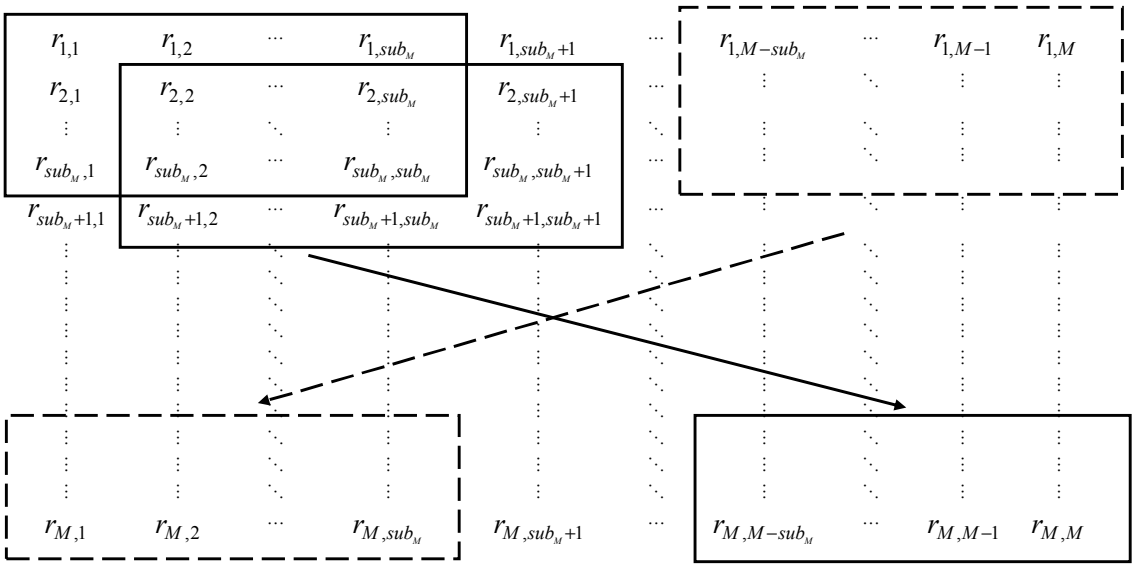

Figure 2.5: Elements of the covariance matrix of X_M. M is the number of antennas and sub_M^2 is the subarray size.

Each subarray R_{sub} differs from its neighbors by a shift of one column and one line. Several other arrangements could also be derived from $\hat{R}_x$ (not only its diagonal), as is also indicated by the dashed arrow in Fig. 2.5. The new cross-spectral matrix $\hat{R}_{x_{SS}}$ is estimated by averaging the S subarrays as

follows:

$$\hat{R}_{x_{SS}} = \frac{1}{S}\sum_{u=1}^{S} R_{sub_u} \tag{2.19}$$

However, spatial smoothing has some disadvantages. The number of detectable signals is decreased because the signal subspace is limited to the dimension of $R_{sub} - 1$. Furthermore, the SS technique reduces angular resolution. Decreasing elements of the final cross-spectral matrix is like decreasing the antenna aperture. Thus, a trade-off between the potential angular resolution and the decorrelation effect has to be established.

Gershman [86] proposes a rule for determining the subarray dimension. The idea is to find $sub_{M_{opt}}$ that maximizes the orthogonality between signal and noise subspaces. In fact, $sub_{M_{opt}}$ estimation depends on prior knowledge of DoA, which is unrealistic in practice. Thus, the Gershman approach assumes two closely spaced incident signals to deduce a DoA-independent expression:

$$sub_{M_{opt}} = 0.6(M+1) \tag{2.20}$$

Although it cannot be stated that significant incident signals are always closely spaced, this approach is helpful in determining spatial smoothing parameters.

A simulation trial with 4 coherent signals impinging upon a ULA of 8 elements and $SNR = 3$ dB is performed. The system configuration is as in Section 2.2.2, with the exception that signals are correlated. Thus, the number of sources, the relative power and the DoA of incident signals are estimated.

Fig. 2.6 shows the number of source estimation using the MDL algorithm.

Before using MDL, the covariance matrix R_x is decorrelated by means of SS. Since $M_{sub} = 5$, the number of displayed bars is 5 and the maximum number of sources that can be resolved is 4. The smaller bar at index 4 displays the correct estimation.

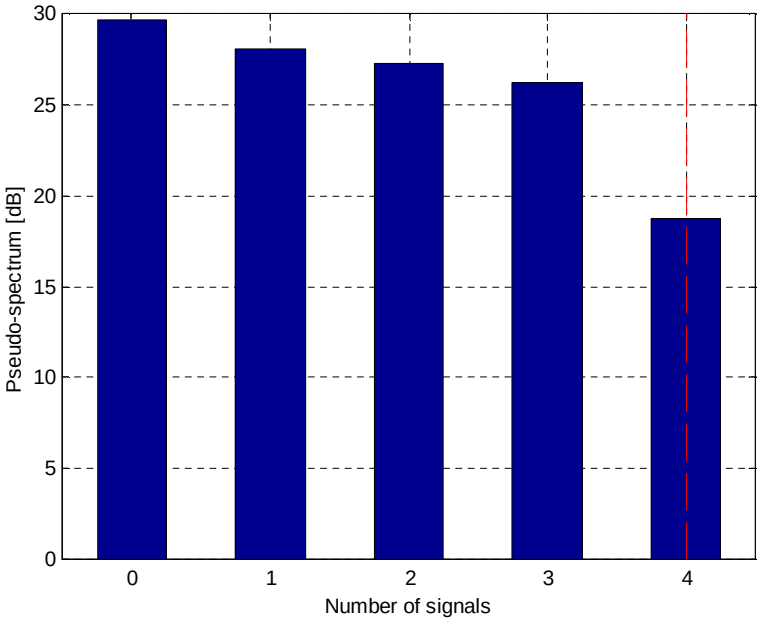

Figure 2.6: Number of source estimation using minimum description length (MDL) for 8 array elements. The theoretical and estimated number of sources is $N = 4$.

Fig. 2.7 illustrates the MUSIC pseudo-spectrum and the Unitary-ESPRIT estimates (vertical lines). Both algorithms fail to estimate DoA values properly. However, after spatial smoothing of data, $\hat{R}_x$ becomes rank efficient and the DoA of incident signals is well estimated. Table 2.2 shows the DoA and power estimates after spatial smoothing in adequate agreement with theoretical values. Source strength is computed by using the MUSIC estimates of DoA normalized to noise power in order to facilitate the performance anal-

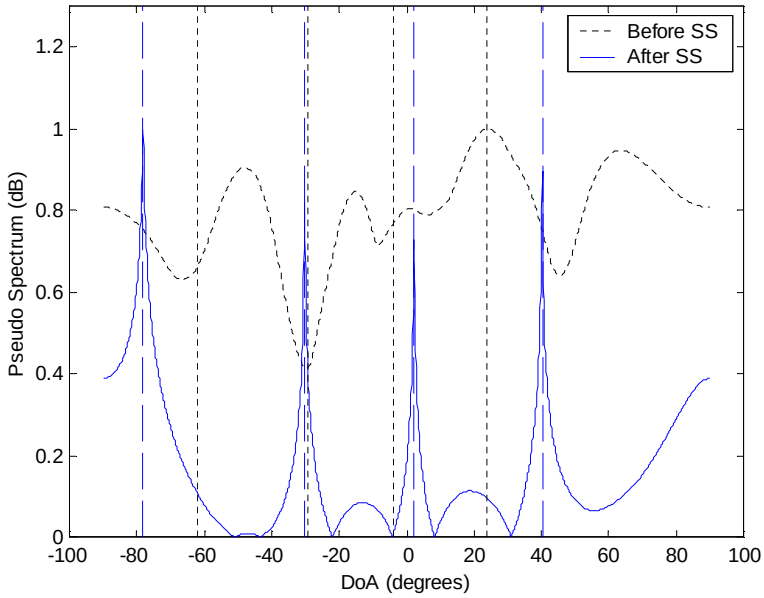

Figure 2.7: DoA estimation of coherent sources using MUSIC and Unitary-ESPRIT algorithms before and after spatial smoothing. $M = 8$, $M_{sub} = 5$ and $SNR = 3$. Vertical lines represent the ESPRIT estimates and the spectrum peaks are the MUSIC estimates

ysis. The DoA estimates is lightly biased. This is caused by the nature of coherent signals or by the SS procedure, since both estimators display a equally biased response.

Table 2.2: DoA and power estimates of 4 coherent sources using ULA array.

Theoretical DoAs	MUSIC	ESPRIT	Normalized Power
-78°	-78.2°	-78.2°	3 dB
-30°	-30.2°	-30.2°	2.9 dB
2°	2.2°	2.2°	2.9 dB
40°	40.2°	40.2°	3.1 dB

2.6 Model extension to frequency domain (for CIR estimation)

In the time domain, a channel path with time delay τ_n provokes a phase shift of $2\pi(f_l - f_o)\tau_n$ between a tone of frequency f_l and a reference tone of frequency f_o. This phase shift structure is similar to that of the antenna processing discussed above. Thus, the data model presented in Section 2.1 can be extended to time/frequency processing.

The Fourier approach is reported as having poor resolution [68, 80] for estimating the channel impulse response (CIR) when the narrowband step mode technique is used. A 1 GHz bandwidth must be swept in order to assure a time resolution of about 1 ns, making necessary the use of devices such as antenna, LNA, etc. of a wider bandwidth. High resolution techniques are proposed [87, 88] for estimating CIR with better resolution performance.

Stimulating a propagation channel with a sweep generator through L CW signals equally spaced over a bandwidth B_w, N propagation paths with different τ_n can be observed as impulse response to this channel.

The channel transfer function is formed of L frequency samples x_{f_t} from the observation data. The data model in (2.1) and the cross-spectral model (2.3) are assumed to be valid to frequency domain processing. Thus, the mode vector $a(\tau_n) \in C^{L\times 1}$ and the equivalent baseband data vector $x[k] \in C^{L\times 1}$ at time k are given by:

$$a(\tau_n) = a_o(\tau_n)\left[1, e^{-j2\pi\Delta f\tau_n}, ..., e^{-j2\pi(l-1)\Delta f\tau_n}, ..., e^{-j2\pi(L-1)\Delta f\tau_n}\right]^T \quad (2.21)$$

Table 2.3: Power delay profile of a propagation channel made-up of 5 coherent paths.

$h(\tau_n)$	PDP - MUSIC	PDP - DFT
21 ns, 0 dB	21 ns, 0 dB	20 ns, 0 dB
33 ns, -6 dB	32.9 ns, -6 dB	32.5 ns, -4.1 dB
40 ns, -9 dB	39.7 ns, -9.1 dB	40 ns, -6.6 dB
49 ns, -12 dB	48.8 ns, -11.9 dB	50 ns, -10.1 dB
74 ns, -24 dB	74 ns, -23.8 dB	75 ns, -21.7 dB

$$x[k] = [x_{f_1}, x_{f_2}, ..., x_{f_l}, ..., x_{f_L}]^T \tag{2.22}$$

where $a_o(\tau)$ is the response of the reference tone (in frequency domain) and Δf is the frequency step between consecutive tones. MUSIC, ESPRIT, Spatial Smoothing and MDL algorithms for one-dimensional processing may then be employed to estimate the time delay of multipath.

A propagation channel is simulated with 5 paths impinging coherently at the receiver by using a step-mode channel sounder. The DFT and MUSIC techniques are used to estimate the power delay profile. A hamming window is used to control the sidelobe level in DFT processing, where 201 frequency tones are swept over an 400 MHz bandwidth with a centre frequency of 2.4 GHz. The number of snapshot is $T = 200$, the SNR is 15 dB and the subarray size used in SS procedure is $L_{sub} = 120$. Spatial smoothing of data is only used for the MUSIC estimation, the results of which are displayed in Table 2.3.

As expected, the MUSIC estimates present better results especially in power estimation. However, the source strength is directly estimated from the DFT spectrum, whereas additional calculations is need for estimating power when MUSIC is used.

2.7 Model extension to 2D antenna array

To build up the necessary knowledge of the channel propagation in the space domain, it is essential to completely determine DoA of multipath. Reflections along the ceiling and floor are only observable if a 2D array is used in the measurements to support elevation angle estimation. Furthermore, the estimation of only the azimuth angle of arrival of incident signals leads to errors if the elevation angle differs from zero, as addressed in [89] and [90].

Compared to 1D array processing, the only changes in the data model (2.1) concern the steering (or mode) vector and the manner of setting elements of the data matrix X_M. Fig. 2.8 shows a plane wave impinging on a uniform rectangular array (URA) with azimuth θ_n and elevation ϕ_n direction of arrival to the plan formed by X and Y axes. The uniform array elements are vertically polarized in relation to the $X - Y$ plan and, consequently, parallel to the plan of the array $(Y - Z)$.

The phase relation between a reference array element and the (y,z)th element of the array may be modeled as a function of the spatial frequencies $k_{y,n}$ and $k_{z,n}$:

$$a_{yz} = e^{j(k_{y,n}+k_{z,n})} = e^{-j\frac{2\pi}{\lambda}[(y-1)\Delta y \cos\phi_n \sin\theta_n + (z-1)\Delta z \sin\phi_n]} \tag{2.23}$$

where y and z are, respectively, the array element indices in the Y and Z domains, and Δy and Δz are the inter-element spacing. Given the number of spatial samples in the Y domain equal to M_y and in the Z domain equal to M_z, the mode vector $a(\theta_n, \phi_n) \in C^{M\times 1}$ with $M = M_y \times M_z$ is made up of

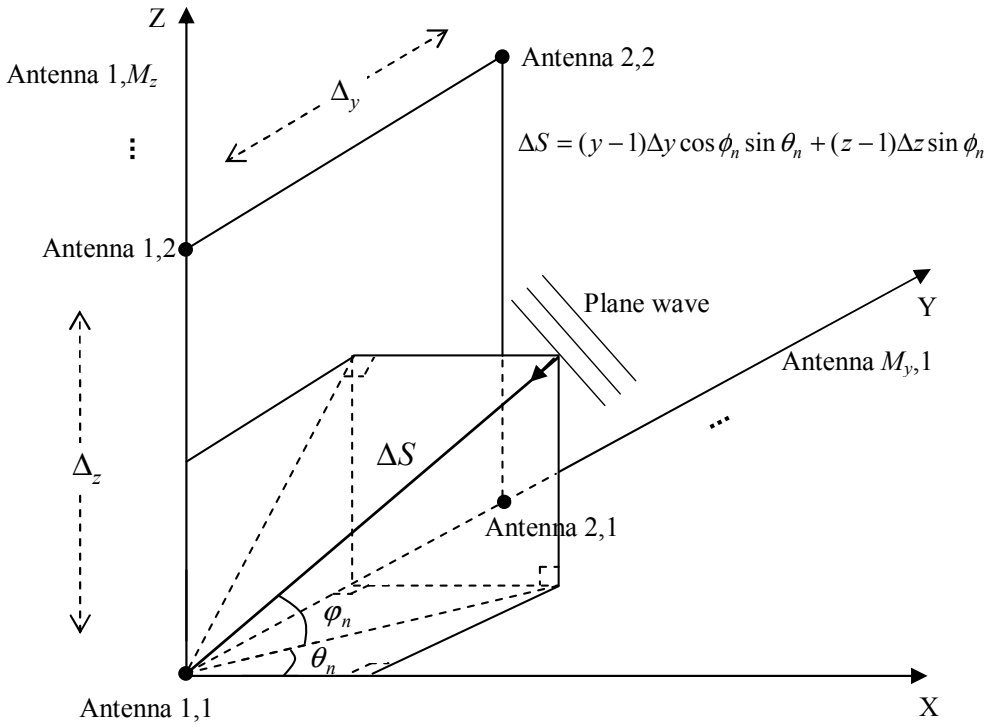

Figure 2.8: Incident signal on a URA array of plan formed by X and Y axes.

M a_{yz} complex values stacked into the column vector as follows:

$$a(\theta_n, \phi_n) = a_o(\theta_n, \phi_n)[a_{11}, a_{12}, ..., a_{1M_z}, a_{21}, ..., a_{M_y M_z}]^T \tag{2.24}$$

where $a_o(\theta_n, \phi_n)$ is the response of the reference element and $(.)^T$ denotes transpose. The equivalent baseband data vector $x[k] \in C^{M\times 1}$ at time k made up of complex values x_{yz} is similarly obtained.

$$x[k] = [x_{00}, x_{01}, ..., x_{0(M_z-1)}, x_{10}, ..., x_{(M_y-1)(M_z-1)}]^T \tag{2.25}$$

For T samples, we may construct the data Matrix $X_M \in C^{M\times T}$ by concatenating T data vectors $x[k]$. All assumptions regarding (2.3) are main-

tained and the cross-spectral matrix R_x may be estimated with (2.4).

The mode vector is swept in the azimuth and elevation domains to compute the MUSIC pseudo-spectrum using (2.6). 2D MUSIC estimates are found after searching for peaks over this spectrum. Contrarily to MUSIC, 2D Unitary ESPRIT estimates require more attention to differences with the 1D approach.

According to [91, 92], the selection matrices J_1 and J_2 are now shifted in the Y and Z domain, forming J_{y1}, J_{y2}, J_{z1} and J_{z2}, as shown in Fig. 2.2. Thus, K_{y1}, K_{y2}, K_{z1} and K_{z2} are determined using (2.12) and (2.13). After estimating the real-valued signal subspace E_{S_Ψ}, as in the 1D approach, we can find Υ in the Y and Z domains from the solution of the real-valued set of equations:

$$K_{y1}E_{S_\Psi}\Upsilon_y \approx K_{y2}E_{S_\Psi} \tag{2.26}$$

$$K_{z1}E_{S_\Psi}\Upsilon_z \approx K_{z2}E_{S_\Psi} \tag{2.27}$$

In order to assure joint estimation of the azimuth and elevation angles, the N eigenvalues λ_n of $(\Upsilon_y + j\Upsilon_z)$ are computed and the spatial frequencies in the Y and Z dimensions are then determined.

$$\hat{k}_{y,n} = 2\arctan(Re\{\lambda_n\})n = 1, 2, ..., N \tag{2.28}$$

$$\hat{k}_{z,n} = 2\arctan(Im\{\lambda_n\})n = 1, 2, ..., N \tag{2.29}$$

The estimation of the azimuth and elevation angles is achieved using the phase relation described in (2.23).

For coherent sources, the extension of the spatial smoothing technique

to the 2D array is presented in [92] for only one snapshot. We introduce a new way to select subarrays from the cross-spectral matrix $\hat{R}_x$ for 2D Spatial Smoothing in [93].

Fig. 2.9 illustrates the subarray selection from the diagram of $\hat{R}_x$. Each small square represents an element of $\hat{R}_x$. The subarrays are square matrices made-up of elements assembled according to the the subarray length in the Y domain (sub_{M_y}) and Z domain (sub_{M_z}).

The new cross-spectral matrix is then determined using (2.19).

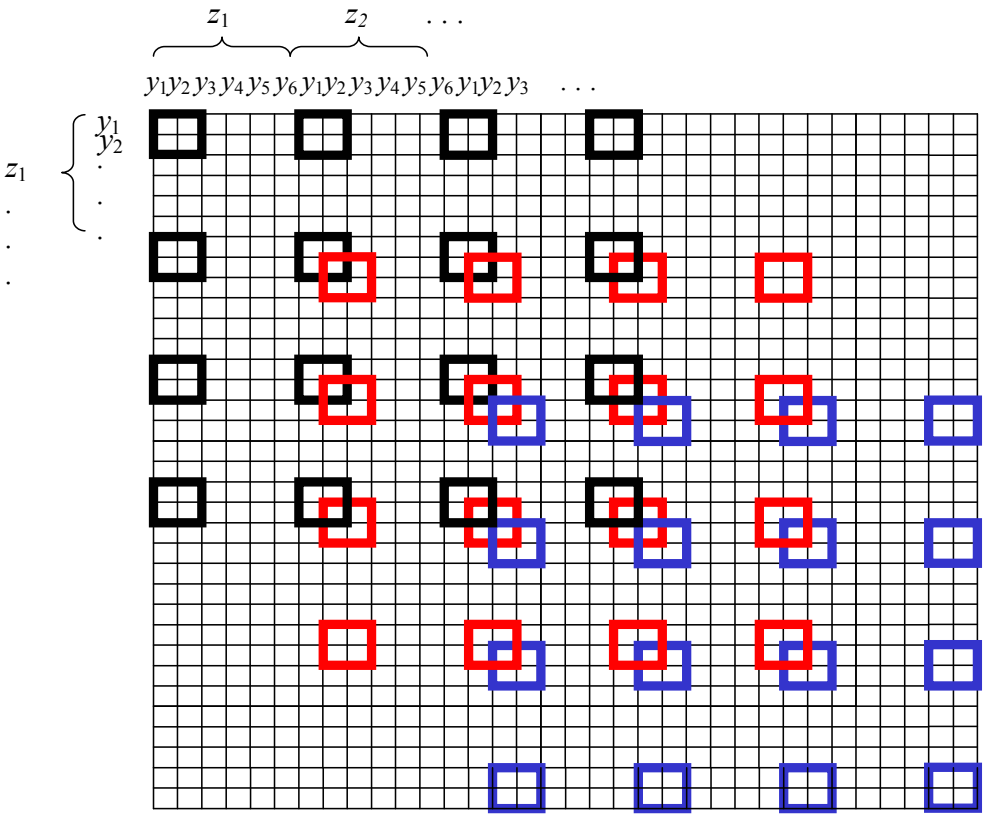

Figure 2.9: Diagram of the elements of $\hat{R}_x$ computed from data of a URA. $M_y = 6$, $M_z = 7$, $sub_{M_y} = 2$ and $sub_{M_z} = 4$.

In order to test the 2D antenna array model presented above and per-

formance of the estimators, the azimuth and elevation angles of incident narrowband signals on a URA are simulated and then estimated.

The inter-element spacing is $\Delta y = \Delta z = \lambda/2$ and the number of array elements is set at $M = M_y \times M_z = 7 \times 4 = 28$. The frequency is set at 2.4 GHz and $SNR = 3$ dB. The DoA estimates of 5 coherent sources are shown in Fig. 2.10.

MUSIC and 2D Unitary ESPRIT algorithms are used after the data spatial smoothing. The MUSIC pseudo-spectrum is plotted as a contour map where the peaks are indicated by the direction of the spectrum gradients. The marks (+) indicate the ESPRIT estimates and (×) corresponds to the theoretical DoAs. Table 2.4 displays both the theoretical and estimated values. A maximum error of 3.8° is observed when the ESPRIT estimator is

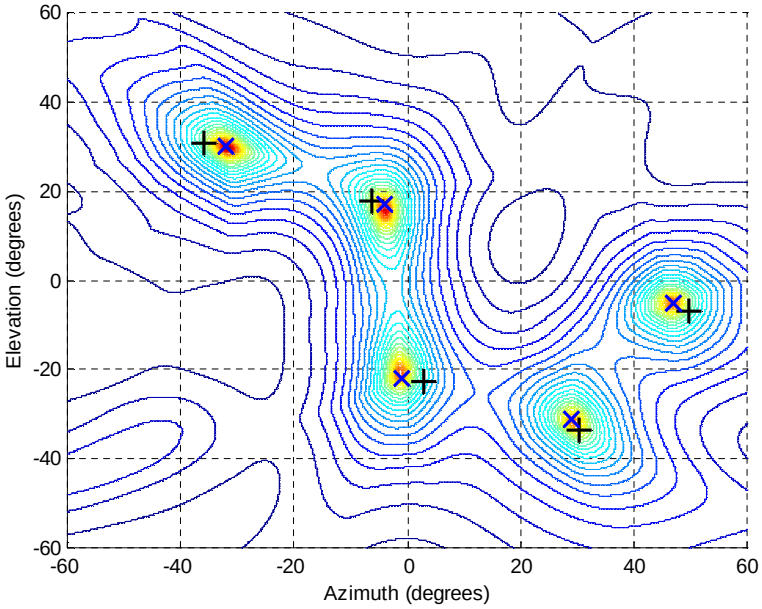

Figure 2.10: Estimation of azimuth and elevation angles of arrival of coherent sources. $M_y = 7$, $M_z = 4$, $sub_{M_y} = 5$ and $sub_{M_z} = 3$. $SNR = 3$ dB. (+) Esprit estimates; (spectrum peaks) MUSIC estimates; (×) theoretical DoAs.

Table 2.4: Azimuth and elevation angle estimation of 5 coherent signals.

Theoretical values (Azimuth, Elevation)	MUSIC estimates (Azimuth, Elevation)	ESPRIT estimates (Azimuth, Elevation)
-1°, -22°	-1.2°, -20.8°	2.9°, -22.5°
47°, -5°	46.8°, -5°	49.8°, -6.9°
-32°, 30°	-32°, 30.1°	-35.8°, 30.9°
-4°, 17°	-4°, 16°	-6.1°, 17.6°
29°, -31°	29.2°, -31.6°	30.4°, -33.5°

used and 1.2° when MUSIC is used. The better performance of the MUSIC estimator proves that this algorithm is more adequate for 2D array schemes than the Unitary ESPRIT. Furthermore, the Unitary ESPRIT seems more sensitive to the SNR level. However, the computational cost grows when the θ-step of the MUSIC spectrum is smaller and the dimension of the array increases.

2.8 Joint DoA and Time Delay estimation

Similarly to 2D antenna array processing, the joint DoA and time delay estimation is carried out by associating the complex response from the antenna array and frequency tones. It is also referred to as directional channel impulse response (DCIR).

Both MUSIC and ESPRIT estimation techniques are limited by the number of array elements for resolving N incident signals. However, joint DoA and Time Delay estimation enables a larger detectable number of sources, as the dimension of its cross-spectral matrix and consequent eigenvectors is larger. Furthermore, the SNR of $\hat{R}_x$ is increased, since it is directly proportional to the number the samples in the space and frequency domains.

Table 2.5: DCIR and Joint azimuth angle - time delay - power estimates.

$h(\tau_n, \theta_n)$	MUSIC estimates
21 ns, -1°, 0 dB	21.1 ns, -1°, 0 dB
33 ns, 47°, -6 dB	33.3 ns, 47.5°, -6.1 dB
40 ns, -32°, -9 dB	39.7 ns, -32.2°, -9.1 dB
49 ns, -4°, -12 dB	49.1 ns, -4°, -12.1 dB

Assuming M and L are the number of array elements and frequency tones, respectively, the space-time steering vector $a(\theta_n, \tau_n)$ is given in the same way as (2.24).

$$a(\theta_n, \tau_n) = a_o(\theta_n, \tau_n)[a_{1,1}, a_{1,2}, ..., a_{1,L}, a_{2,1}, ..., a_{M,L}]^T \tag{2.30}$$

where $a_o(\theta_n, \tau_n)$ is the response of the reference frequency tone at the first array element and a_{ml} is expressed as:

$$a_{m,\ l} = e^{-j\frac{2\pi f_l}{c}(m-1)\sin\theta_n} e^{-j2\pi(l-1)\Delta f \tau_n} \tag{2.31}$$

The frequency f_l is taken into account in (2.31) because DoA estimation is based on a wavelength-dependent phase shift between array elements. All algorithms used for 2D array processing may be extended to resolve joint DoA and time delay estimation. This idea may be also used to resolve an N-dimensional structure at the expense of increasing system complexity.

A trial is arranged using the model (2.30) to perform simulation and estimation of joint DoA and time delay of channel multipath, as shown in Fig. 2.11. Table 2.5 displays the DCIR and the estimated values.

The estimates presented in Table 2.5 are mostly in adequate agreement with the theoretical values. This confirms the capacity of the present algo-

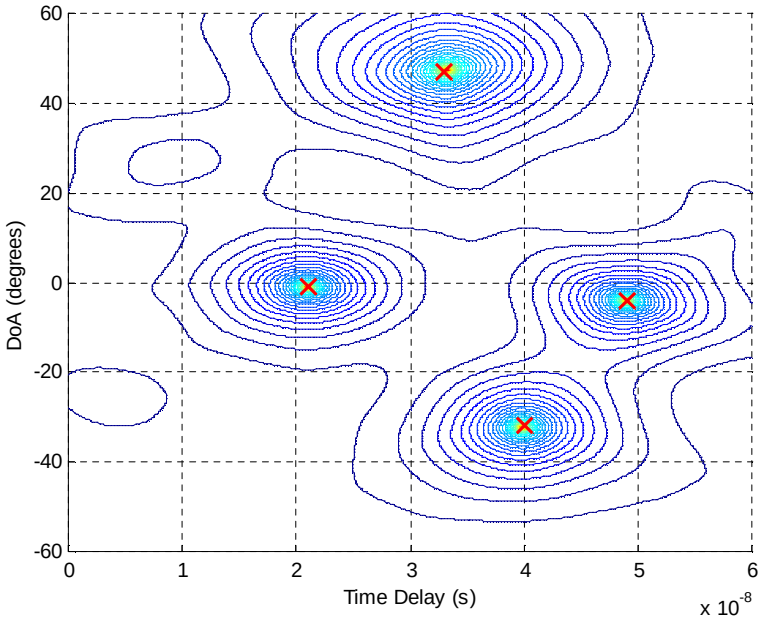

Figure 2.11: Joint estimation of azimuth angle and time delay of coherent paths. $B_w = 80$ MHz and $f_c = 2.4$ GHz. $M = 8$, $L = 41$, $sub_M = 5$ and $sub_L = 26$. $SNR = 15$. (Spectrum peaks) MUSIC estimates; ($\times$) theoretical values.

rithms for properly resolving source strength, DoA and time delay of channel multipath in the presence of AWGN and coherence between sources.

2.9 Estimation performance under modeling errors

A number of tests in the estimation system are considered important for verifying algorithm robustness under modeling errors such as the presence of non-dominant paths and non-plane waves.

Let an antenna located at the position p_s transmit RF signals toward a linear antenna array with radial distance from one another $r_s < 2R_a^2/\lambda$, where

R_a is the largest array dimension and the elements of the array are located at the position p_m. Thus, the near-field propagation model is required to generate the array response of simulated signals.

The near-field steering vector of the array is defined as a function of the radial distance $r_{m,s}$ between the signal source and the mth array element [94]:

$$a(r_{m,s}) = \frac{r_s}{e^{j2\pi r_s/\lambda}} \left[\frac{e^{j2\pi r_{1,s}/\lambda}}{r_{1,s}}, \ldots, \frac{e^{j2\pi r_{m,s}/\lambda}}{r_{m,s}}, \ldots, \frac{e^{j2\pi r_{M,s}/\lambda}}{r_{M,s}} \right]^T \tag{2.32}$$

100 different realizations of two equipowered narrowband signals with random DoAs impinging on a linear array of 8 elements and $d = \lambda/2$ are simulated. Thus, the standard deviation (STD) of DoA estimates is computed. Fig. 2.12 shows STD as a function of the the radial distance r_s between the signal source and the antenna array. The SNR is set at 10 dB and the number os snapshots is 1000 for each realization.

The vertical dashed line in Fig. 2.12 represents the far-field limit for the present array configuration. An exponential behavior is observed in both curves with a STD of 1° for $r_s = 1m$ when the MUSIC estimator is used. Saturation is observed for both curves in the far-field zone where the propagation model becomes distance-independent. The MUSIC algorithm presents better robustness under estimation errors in the near-field zone. However, the performance of both techniques becomes increasingly similar as r_s grows.

In order to test algorithm robustness from the resolution standpoint, a similar set of simulations is carried out, where STD is computed as a function of the angular spacing $\Delta\theta = \theta_1 - \theta_2$ of the two equipowered signals with

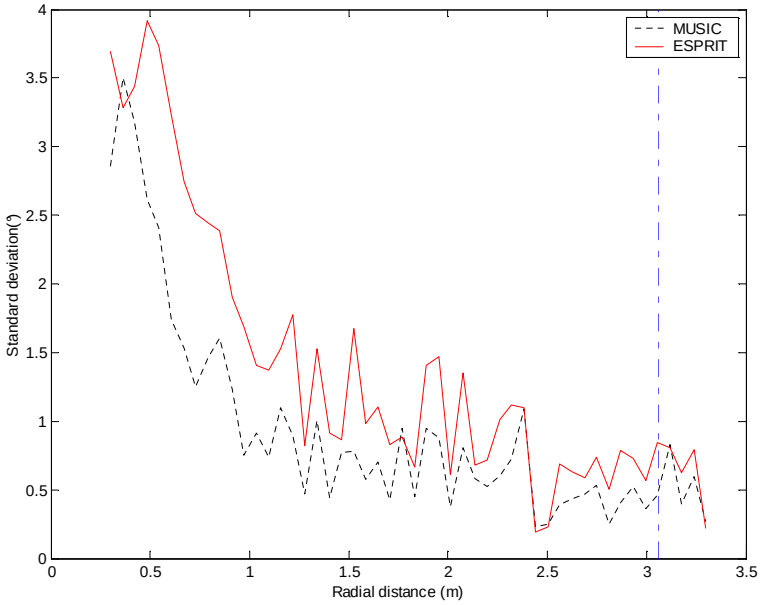

Figure 2.12: Standard deviation of DoA estimates for MUSIC and Unitary ESPRIT versus r_s of two impinging equipowered signals.

$SNR = 10$ dB. 1000 snapshots are used for each realization and the number of elements $M = 3$. This relation is illustrated in Fig. 2.13.

Fig. 2.13 shows the standard deviation below 1^o for an angle separation larger than 15° for both the MUSIC and Unitary-ESPRIT algorithms when $SNR = 10$ dB and $M = 3$. Under such condition, a maximum error of 2.5° is found for $\Delta\theta = 5°$.

For $\Delta\theta < 5°$, the STD experiences a decrease because the estimation of closely spaced sources tends to induce a single estimate located between them. This single estimate is usually not far from the source locations.

The dashed vertical line represents the theoretical resolution of the MUSIC algorithm proposed by Kaveh [82] for this configuration. The result is coherent, as the SNR is low and only 3 array elements with $d = \lambda/2$ are used,

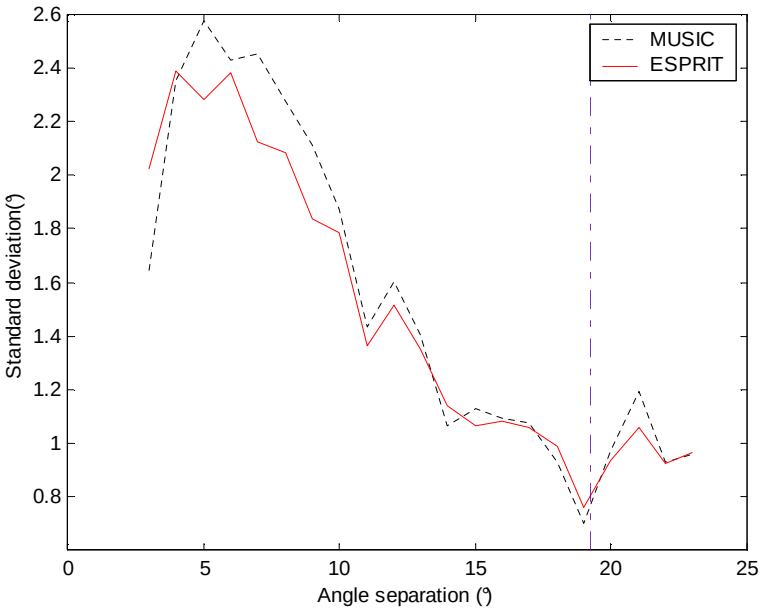

Figure 2.13: Standard deviation of DoA estimates for MUSIC and Unitary ESPRIT versus $\Delta\theta$. $SNR = 10$

corresponding to a small antenna aperture.

Both sets of trials demonstrate the robustness of the MUSIC algorithm in resolving DoA estimates even in the presence of sources of error that are not taken into account in the data model.

In [95], Wölfle states that in propagation channels only two or three rays contribute more than 95 percent of the energy on the receiving antenna, and by focusing on these dominant rays, accuracy would be sufficient. This is confirmed experimentally by Kim [96] for indoor propagation channels.

A simulation trial is carried out to test the system capability for estimating 4 dominant paths surrounded by 1000 attenuated paths. Multipath is subject to a random uniform distribution, engendering different DoAs, time delays and wavefront curvatures of incident signals. The step frequency

sounding technique and antenna array processing are used to estimate joint DoA and time delay of coherent signals, as shown in Fig. 2.14. Simulation

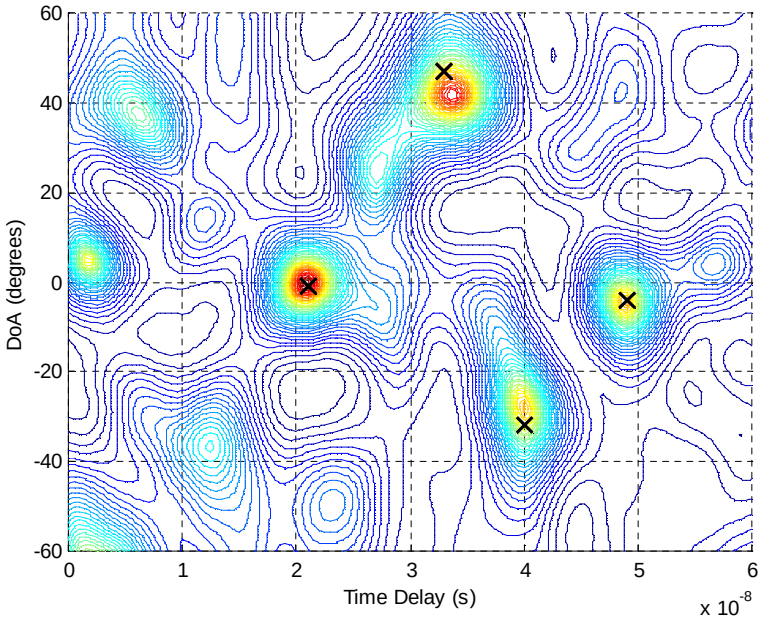

Figure 2.14: Joint DoA and time delay estimation of four coherent paths surrounded by 1000 attenuated paths. $B_w = 200$ MHz and $f_c = 2.4$ GHz. $M = 8$, $L = 101$, $sub_M = 5$ and $sub_L = 61$. , $SNR = 15$ dB. (Spectrum peaks) MUSIC estimates; ($\times$) Theoretical values.

parameters are $B_w = 200$ MHz and $f_c = 2.4$ GHz, $M = 8$ and $L = 101$, $M_{sub} = 5$ and $M_{sub} = 61$, $SNR = 15$ dB. The power of non-dominant paths varies from 17 dB to 67 dB below the strength of the strongest path. Simulation results are displayed in Table 2.6.

Under a more realistic condition, the channel parameters of 4 dominant paths corresponding to 80 percent of total power are well estimated, especially in the time delay domain. It is due to the large number of frequency tones compared to the number of antennas. The number of dominant sources is also well estimated by MDL.

Table 2.6: DCIR and Joint DoA, time delay and power estimates of 4 dominant paths.

$h(\tau_n, \theta_n)$	MUSIC estimates
21 ns, -1°, 0 dB	21 ns, 0°, 0 dB
33 ns, 47°, -6 dB	33.5 ns, 42°, -2.7 dB
40 ns, -32°, -9 dB	40 ns, -28°, -6.8 dB
49 ns, -4°, -9 dB	49 ns, -4.5°, -6.6 dB

Since the element response model is non-linear (1.1), a larger direction of arrival makes the estimation performance more sensitive to phase errors. This is observed for the $2nd$ and $3rd$ paths with errors of 5° and 4°, respectively. When the number of frequency tonnes is large, the MUSIC estimator appears to be independent on the knowledge of the number of sources. It is due to the noise subspace that is too large compared to the number of dominant signals and the choice of the noise subspace size is then less important compared to systems with small structures.

2.10 Conclusion

In this chapter, we presented the means and tools for the temporal-spatial characterisation of SIMO propagation channels. Various algorithms used to resolve the number of sources, DoA, time delay and power estimates are described. A brief state-of-the-art regarding MUSIC and ESPRIT algorithm performances are presented, followed by simulation trials of propagation channel parameters and their estimates. More realistic experiments are then simulated to test the robustness of the MUSIC and Unitary-ESPRIT algorithms.

Usually considered as a suboptimal technique when compared to more complex algorithms, MUSIC is relatively robust to modeling errors, as shown above and reported in [68, 9, 18], which justifies its wide dissemination in recent years.

Chapter 3

Five-Port discriminator in microstrip technology

INTRODUCTION

The five-port discriminator corresponds to a passive and linear circuit that performs vectorial measurements of the ratio between input electromagnetic waves. It has recently been used for applications such as a homodyne demodulator of RF signals [97, 98, 99], phase/frequency discriminator for anti-collision radars [100] and Phase Local Loop (PLL) [101]. Thus far, this technique has been implemented in microstrip [102], coaxial [103] and MMIC [104] technologies.

Like I-Q systems, the five-port discriminator also performs a direct conversion of RF signals, but uses a redundant mixer and a basis of 120 degrees [1] instead of the Cartesian basis. This redundancy makes the five-port discriminator more robust for the phase and amplitude unbalance of the local oscillator and, consequently, less sensitive to the error vector magnitude

(EVM) in comparison to I-Q systems, as shown in [4]. Drawbacks to the five-port include the DC offset intrinsic in five-port discriminators because power detectors are used as mixers. The resistive circuit used to match the power detector to 50 Ohm allows us to reach a wideband of 800 MHz around 2.4 GHz. However, this matching circuit causes energy dissipation and, consequently, sensitivity loss.

The complex envelope information when using the five-port technique is obtained by making only amplitude (or power) measurements of three different linear combinations of RF and local oscillator electromagnetic waves. This means that a five-port discriminator is in principle simply a passive linear circuit with two input ports and three output ports (hence its name).

Indeed, the five-port discriminator is a constrained version of the six-port which was originally designed to measure the reflection coefficient of microwave loads. Introduced by G. F. Engen and C. A. Hoer in 1972 [105], the six-port discriminator was widely used in metrological laboratories to perform precise RF circuit measurements. If the local oscillator (LO), used as reference of phase and frequency, is stable enough so that its power can be assumed to be constant, one of the six-port outputs may be neglected and the complex ratio between input signals may be well accomplished in five-port system [106].

During the thesis we decided to use a five-arm ring as an interferometric circuit made-up of microstrip lines and CMS (Component Mounted Surface) components due to its design and utilization ease as a phase/amplitude discriminator. In this chapter, we describe the microstrip five-port discriminator in detail. We first present the five-arm interferometric circuit and power

detectors. The operating principle of the five-port system is then shown, including the calibration procedure used to correct circuit imperfections and compensate phase and amplitude losses in cables.

3.1 Description of the microstrip Five-Port discriminator

The five-port system shown in Fig. 3.1 consists of a five-access interferometric ring implemented in microstrip technology. Two accesses of the five-arm ring are the RF and local oscillator input ports and the three others are each connected to a diode power detector followed by a low-pass filter. This system has the purpose to generate a signal $x(k)$ in the digital domain representing the complex ratio between the two input RF and LO signals as a linear combination of the three analogic voltages at the five-port discriminator outputs. This complex ratio is computed by digital signal processing (DSP) after A/D conversion of five-port output voltages v_3, v_4 and v_5.

3.1.1 The five-arm ring

The circular five-arm ring chosen as the interferometric circuit is represented in Fig. 3.2. The arms are spaced equally over the circuit ring designed in microstrip technology. This circuit performs 3 vectorial additions of the 2 input signals: the RF signal picked up by the antenna and LO signal. The five-arm ring has reciprocity and symmetry as features. Thus, the S-parameters of this circuit are defined as follows:

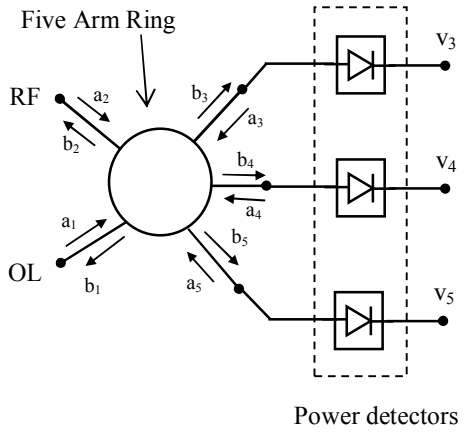

Figure 3.1: A Five-Port discriminator designed in microstrip technology.

$$\begin{aligned}
\text{Reciprocity} \quad &\Longrightarrow \quad S_{ij} = S_{ji} \forall i, j \in 1, 2, 3, 4, 5 \\
\text{Symmetry} \quad &\Longrightarrow \quad S_{ii} = R \forall i \in 1, 2, 3, 4, 5 \\
&\qquad\quad S_{12} = S_{15} = S_{23} = S_{34} = S_{45} = \alpha \\
&\qquad\quad S_{13} = S_{14} = S_{24} = S_{25} = S_{35} = \beta
\end{aligned}$$

Using these properties, the S matrix is expressed as:

$$S = \begin{pmatrix} R & \alpha & \beta & \beta & \alpha \\ \alpha & R & \alpha & \beta & \beta \\ \beta & \alpha & R & \alpha & \beta \\ \beta & \beta & \alpha & R & \alpha \\ \alpha & \beta & \beta & \alpha & R \end{pmatrix} \tag{3.1}$$

The relation between the non-zero eigenvalues of S (s_1, s_2 and s_3) and the independent variables (R, α and β) was proposed by Dickie [107], using the rotation and symmetry properties of the five-arm ring:

$$S_{11} = R = (S_1 + 2S_2 + 2S_3)/5 \tag{3.2}$$

$$S_{12} = \alpha = (S_1 + 2S_2\cos(2\pi/5) + 2S_3\cos(4\pi/5))/5 \tag{3.3}$$

$$S_{13} = \beta = (S_1 + 2S_2\cos(4\pi/5) + 2S_3\cos(2\pi/5))/5 \tag{3.4}$$

For a non-lossy five-arm ring circuit, Dickie demonstrates that the magnitude of the eigenvalues correspond to:

$$|S_1| = |S_2| = |S_3| = 1 \tag{3.5}$$

Thus, by choosing arbitrarily the S_1 phase as 180^o, we have:

$$S_1 = -1;\ S_2 = e^{j\psi_2};\ S_3 = e^{j\psi_3} \tag{3.6}$$

Considering $R = 0$ (matched system) and using (3.6), the expression (3.2) becomes:

$$0 = -1 + 2e^{j\psi_2} + 2e^{j\psi_3} \tag{3.7}$$

This equality is verified only if:

$$\psi_2 = -\psi_3 = \psi = \arccos(1/4) \cong 75.5^o \tag{3.8}$$

By rearranging (3.3)-(3.5) and (3.8), we can find the eigenvalues of S and the parameters α and β.

$$\alpha = \frac{1}{2}e^{j\frac{2\pi}{3}} \text{ and } \beta = \frac{1}{2}e^{j\frac{-2\pi}{3}} \tag{3.9}$$

Therefore, the matched five-arm ring works as a power splitter by sharing the received power into equal parts and sharing it out over all other arms

with a $\pm 120°$ phase-shift. Fig. 3.2 describes the different dimensions that characterize a five-arm junction designed in microstrip technology. Design rules are needed in order to give this circuit well matched conditions. The characteristic impedance of the 5 access lines ($Z_0 = 50$ ohms) allows us to evaluate their widths as a function of the substrate features.

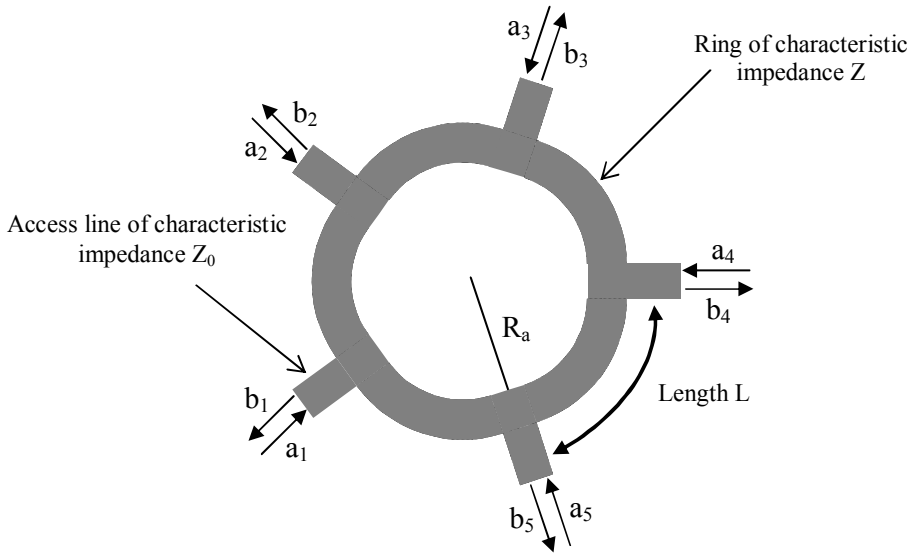

Figure 3.2: Five arm ring.

The following equations give us the ring dimensions (width and radius) and characteristic impedance Z:

$$\theta = \frac{2\pi L}{\lambda} = \arccos(1/4) \cong 75.5^o \tag{3.10}$$

$$R_a = \frac{5L}{\pi} \tag{3.11}$$

$$Z = \frac{\sqrt{3}}{2\sin(\theta)} Z_0 = \frac{2}{\sqrt{5}} Z_0 = 44.7\Omega \tag{3.12}$$

λ represents the effective wavelength in the substrate for a given frequency,

L is the length between two arms and R_a is the radius of the ring. The ring dimensions are optimized by the ADS (Advanced Design System) software for a five-port system working around 2.4 GHz. This optimization is performed by minimizing the reflection coefficient at the 5 accesses of the ring for frequencies around 2.4 GHz. The present ring is printed on an FR4 substrate with the following characteristics:

- Dielectric features:
  - epoxy;
  - width: $h = 1.59$ mm;
  - permittivity: $\varepsilon_r = 4.1$;
  - dielectric losses: $\tan(\delta) = 0.02$.
- Conductor features:
  - copper on both sides of the substrate;
  - copper thickness, $e = 35\mu$m.

The optimized dimensions are as follows:

- Width of the access lines (50 ohms): 3.16 mm;
- Width of ring: 3.6 mm;
- Radius of the ring: 10.2 mm.

Fig. 3.3 illustrates simulation results of return loss at the input port 1 of a five-port reflectometer. The curve shows that the circuit input is well

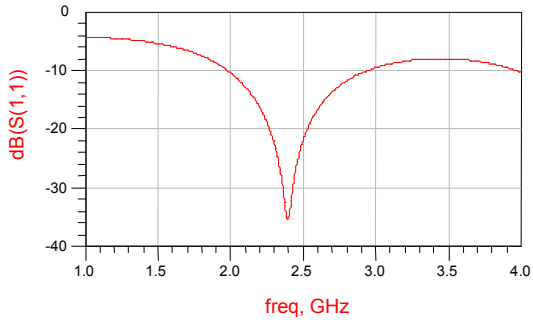

Figure 3.3: Reflection coefficient S_{11} at the input port 1.

matched ($S_{11} < -10$ dB) over a wide band of 1 GHz around 2.4 GHz. The circuit symmetry guarantees similar performance at the input port 2.

The magnitude of S_{12} and S_{13} and the phase difference between the S_{12} and S_{13} arguments as a function of the frequency are presented in Fig. 3.4. We can see that S_{ij} $(i \neq j)$ has magnitude around 0.5 and a phase shift between S_{12} and S_{13} around 120^o for 2.4 GHz. These results confirm the relation (3.9).

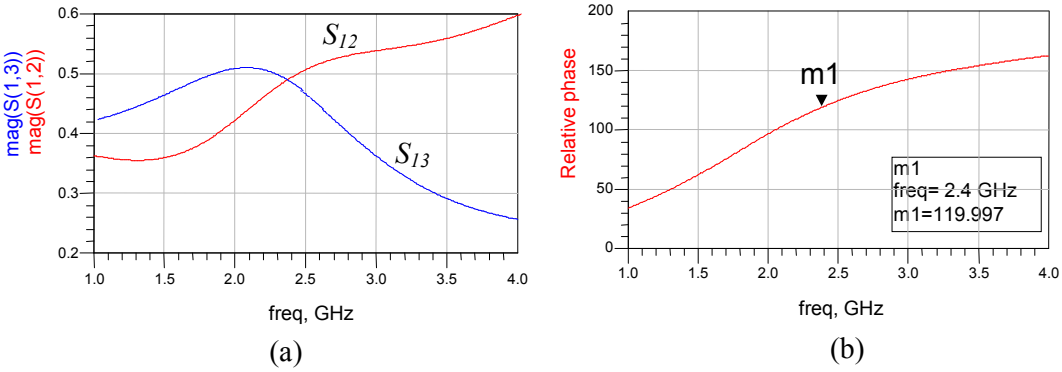

Figure 3.4: The amplitude of S_{12} and S_{13} (a) and the phase shift between S_{12} and S_{13} (b) as a function of frequency.

3.1.2 The power detectors

As illustrated in Fig. 3.1, a Schottky diode is connected to each five-arm ring output. The non-linear and current-voltage characteristic of this kind of diode permits its use as a power detector with input voltages given by v_{b-i}, $i \in \{3, 4, 5\}$. An Agilent Schottky diode (HSMS2850) with reflection coefficient magnitude of about 0.6 at 2.4 GHz [3] is used.

A Schottky diode and a low-pass filter (RC_L) make up the power detector illustrated in Fig. 3.5. The low-pass filter rejects the HF terms after diode mixing.

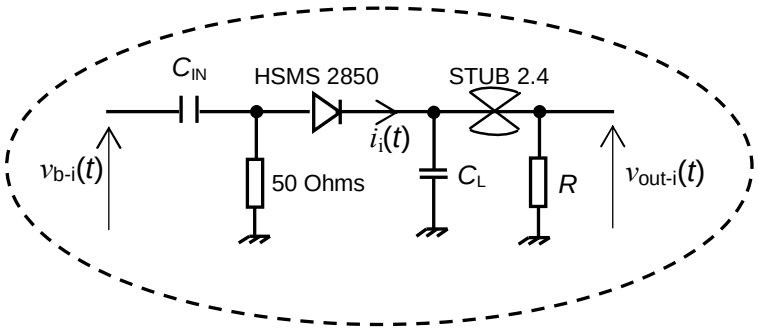

Figure 3.5: A quadratic detector based on a Schottky diode.

At the output of the diode, the low frequency component of the signal generates a voltage (v_{out-i}, $i \in \{3, 4, 5\}$) across the output resistor (R), which is a linear function of the RF signal power. Fig. 3.5 shows a DC-block capacitor (C_{IN}) and a 50-Ohm resistor used to match the power detector over a wide bandwidth. Its reflection coefficient simulated with ADS is illustrated in Fig. 3.6 with and without the matching circuit.

However, this matching circuit produces a reduction in sensitivity, as a large part of the incident energy is dissipated due to the Joule effect. A

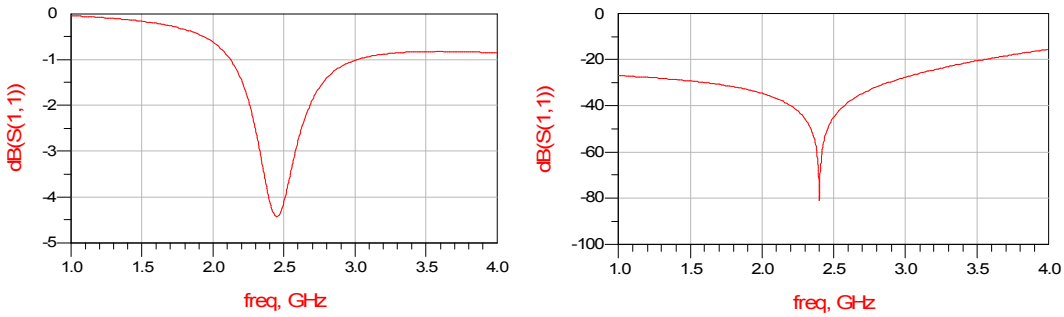

Figure 3.6: Reflection coefficient at the power detector input with (left) and without (right) the matching circuit.

reactive matching technique that performs better sensitivity is proposed by [108]. Nevertheless, this technique is not suitable for wideband application. In order to improve the RF filtering output, a butterfly stub tuned to 2.4 GHz is added, which counteracts impedance variations in the detector output as a result of cable movement, etc [98] and eliminates other residual signals at 2.4 GHz after RC filtering. This open-circuit stub of $\lambda/4$ length is located at the detector output and nulls the RF component at 2.4 GHz. Schottky's law describes the relation between the diode current $i(t)$ and the RF input voltages $v_{b-i}(t)$.

$$i_i(t) = I_S \left[\exp\left(\frac{v_{b-i}(t)}{V_T} \right) - 1 \right] \tag{3.13}$$

where $V_T = 26$ mV and I_S represents the saturation current of the diode ($I_S = 3\mu$ A for HSMS2850 Agilent) [3]. For low input power, we can approximate (3.13) using [109]:

$$i_i(t) = I_S \left[\left(\frac{v_{b-i}(t)}{V_T} \right) + \frac{1}{2} \left(\frac{v_{b-i}(t)}{V_T} \right)^2 + \dots \right] \tag{3.14}$$

The output equivalent circuit of the diode detector may be modeled as Fig. 3.7 [5] where R_V corresponds to the video resistance (or dynamic resistance) of the power detector.

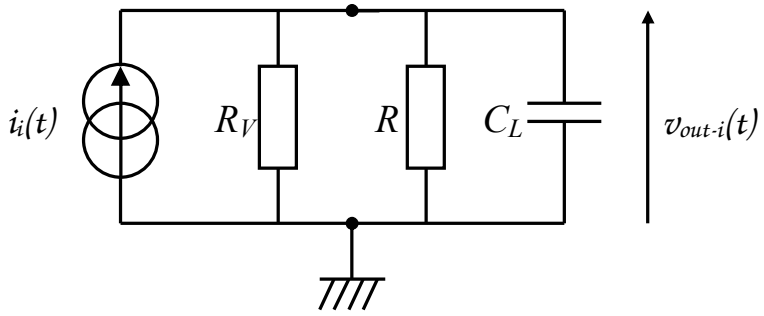

Figure 3.7: The Output equivalent circuit of the diode detector.

The resistors R_V and R and the capacitor C_L short-circuit the HF signal in the diode output, behaving as a first-order low-pass filter with cut frequency f_c:

$$f_c = \frac{R_V + R}{2\pi R_V R C_L} \tag{3.15}$$

At the low-pass filter output, the measured voltage $v_{out-i}(t)$ is proportional to the even-order terms of (3.14), that is, the baseband terms of $i_i(t)$. Therefore, for identical power detectors over all five-port outputs, the three output voltages $v_{out-1}(t), v_{out-2}(t)$ and $v_{out-3}(t)$ that obey the quadratic law of a power detector may be represented by:

$$v_{out-i}(t) = D(v_{b-i}(t))^2 \tag{3.16}$$

with

$$D = \frac{R_V R}{R_V + R} \frac{I_S}{2V_T^2} \tag{3.17}$$

The quadratic behaviour of the schottky diode is only true for low-input power. For input signals with power over -15 dBm, forth and higher order effects become significant [3] and a curve fitting procedure is necessary to increase the dynamic range of the power measurements. Among the numerous methods found in the literature, we have chosen Potter *et al* [110], as it may be applied to each detector independently. Potter's function is a non-linear polynomial of Mth order used to find the appropriate voltage $v_{fitting}$ from the measured voltage v_{mes}.

$$v_{fitting} = v_{mes} e^{f(v_{mes})} \tag{3.18}$$

where

$$f(v_{mes}) = \sum_{k=1}^{M} b_k v_{mes}^k \tag{3.19}$$

The constants b_k of the polynomial $f(.)$ are found from the fitting procedure and the chosen polynomial order is $M = 4$ [53]. Fig. 3.8 shows the power detector output before and after voltage correction for input signals at 2.4 GHz. The curves illustrate the voltage variation as a function of power and show the linear behaviour after correction. Power dynamic range from -30 dBm to 9 dBm was chosen since the diodes saturate over 9 dBm and the system noise becomes preponderant under -30 dBm and, consequently, the measurements become imprecise.

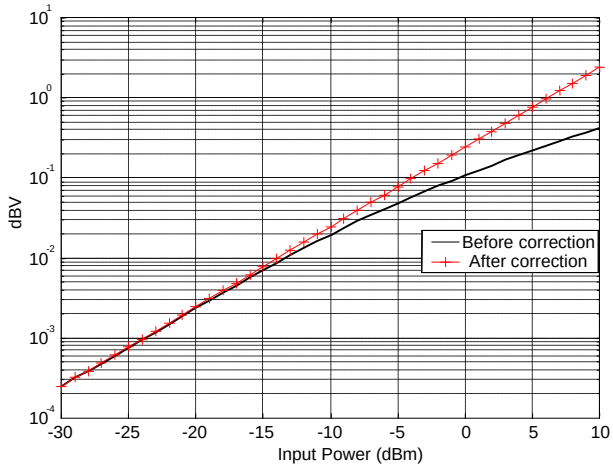

Figure 3.8: Voltage in the power detector output before and after correction.

3.1.3 The Five-Port circuit implementation

In this section, the five-port implementation in microstrip technology is described. Fig. 3.9 shows the circuit layout designed with ADS software.

As reported in Chapter 1, the chosen sounding technique needs narrowband A/D conversions since the channel transfer function is measured using CW signals that sweep the entire bandwidth. Thus, a low cut-off frequency of some hertz would be enough to satisfy measurements of a slowly time-varying channel, such as in indoor environments. However, the present measurement system is also used to demodulate modulated signals, as will be seen in Chapter 4. Therefore, a slightly larger cut-off frequency is chosen, namely, $f_c = 180$ KHz. According to (3.15), this cut-off frequency is obtained by using a resistance $R = 220$ KΩ and a capacitance $C_L = 100$ pF. The chosen diode has video resistance $R_V = 9$ KΩ. A photograph of the implemented circuit is shown in Fig. 3.10.

This circuit can be inscribed in a rectangle of 10 cm in length and 8 cm

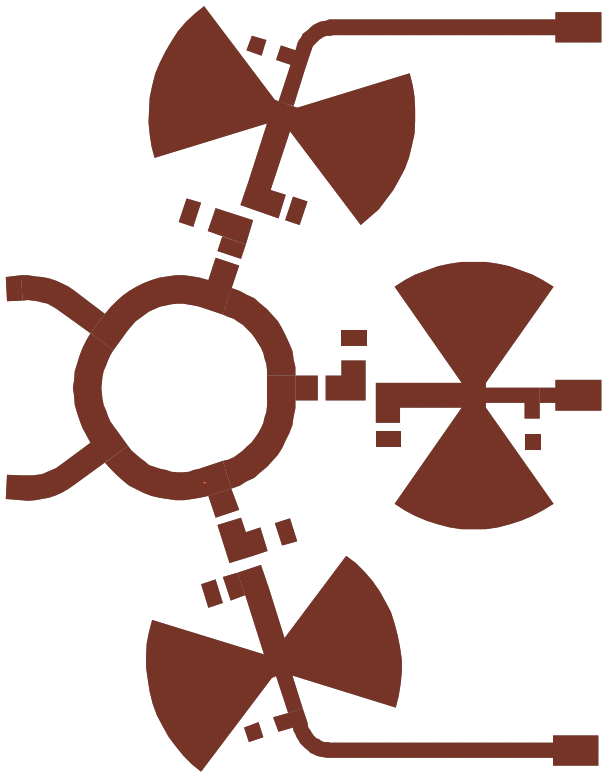

Figure 3.9: ADS layout of the five-port circuit in microstrip technology. Scale 1:1.

in width. As described above, the substrate is FR4 epoxy and the power detectors are Agilent HSMS 2850. The S11 parameter of the implemented five-port circuit is illustrated for measurement and simulation.

This curve shows that the five-port circuit is well matched (S_{11} < -10 dB) over a wideband (1 GHz around 2.4 GHz). We can observe in the curve corresponding to the measurements a slight shift from the center frequency. This is due to the permittivity of the substrate, as it is difficult to determine its exact value.

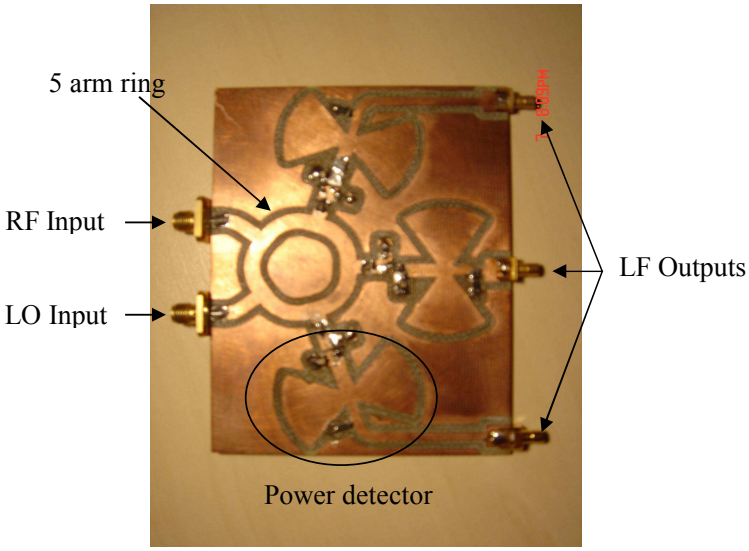

Figure 3.10: Photograph of a five-port reflectometer implemented in microstrip technology. It is designed to work around 2.4 GHz. Scale 1:2.

3.2 Operating principle of the Five-Port system

When used as an RF receiver (see Fig. 3.12), the purpose of the five-port system is to demodulate an RF signal $a_2 = A_{RF}x(t)\exp(j2\pi f_{RF}t)$, with f_{RF} being the carrier frequency, $x(t) = I(t) + jQ(t)$ the complex envelope and A_{RF} the RF signal amplitude. This is performed using a local oscillator $a_1 = A_{LO}\exp(j2\pi f_{LO}t)$, where f_{LO} is the LO frequency and A_{LO} the amplitude. The five-arm ring makes three vectorial additions between the two input signals a_2 and a_1. Using Fig. 3.2, we can write:

$$b_i = A_i a_1 + B_i a_2, \quad i = 3, 4, 5 \tag{3.20}$$

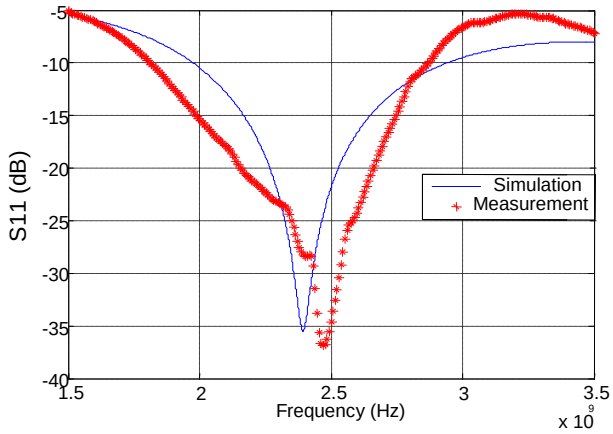

Figure 3.11: Return loss at input 1 of the five-port reflectometer.

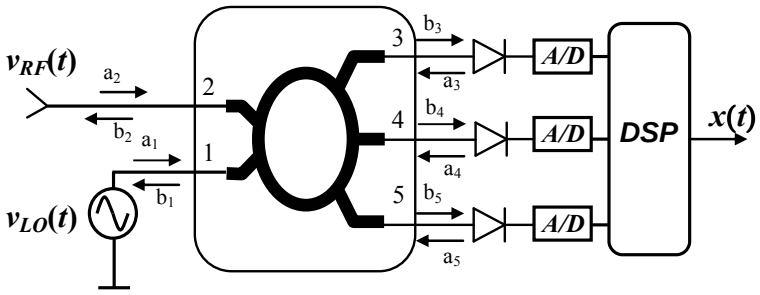

Figure 3.12: Receiver based on a Five-Port discriminator. $x(t) = \frac{a_2}{a_1} = I(t) + jQ(t)$.

where b_i is the transmitted pseudo power wave at ports 3, 4 and 5 of the ring, and A_i and B_i are complex constants that depend on the characteristics of the reflectometer. b_i may also be described as a function of the scattering parameter S_{ij} and the pseudo power wave a_j incident at port j.

$$b_i = \sum_{j=1}^{5} S_{ij} a_j, \quad i = 1 \ldots 5 \tag{3.21}$$

Assuming that the power detectors are permanently connected at the

discriminator output ports, one may write

$$a_j = b_j \Gamma_j, \quad j = 3, 4, 5 \tag{3.22}$$

where Γ_j is the reflection coefficient of the power detectors at port j. The power level detected in the discriminator outputs may be expressed by

$$P_i = |b_i|^2 \left(1 - |\Gamma_i|^2\right), \quad i = 3, 4, 5 \tag{3.23}$$

By manipulating equations [111], it is possible to write the complex ratio between the input pseudo power waves as a linear combination of the voltages $\tilde{v}_{out-3}$, $\tilde{v}_{out-4}$ and $\tilde{v}_{out-5}$ measured at the low-pass filter outputs after dc-offset cancellation

$$x = a_{cal}\tilde{v}_{out-3} + b_{cal}\tilde{v}_{out-4} + c_{cal}\tilde{v}_{out-5} \tag{3.24}$$

where the complex values a_{cal}, b_{cal} and c_{cal} are three calibration constants and $\tilde{v}_{out-3}$, $\tilde{v}_{out-4}$ and $\tilde{v}_{out-5}$ are proportional to P_3, P_4 and P_5. The calibration constants are determined by a calibration procedure such as the one presented in [98] overviewed in Section 3.2.2. It is important to notice that contrary to a six-port system, the power level at the reference input port of a five-port system must be the same for system calibration and operation, as the constants depend on a_1.

3.2.1 Evaluation of the output voltages

The RF voltages at the power detector input $v_{b-3}(t), v_{b-4}(t)$ and $v_{b-5}(t)$ (see Fig. 3.5) are obtained from (3.20) by calculating the band-pass representation

of the vectorial addition between the RF and LO signals.

$$v_{b-i}(t) = \Re\left[A_i A_{LO} e^{j2\pi f_{LO}t} + B_i x(t) A_{RF} e^{j2\pi f_{RF}t}\right], \quad i = 3\ldots5 \tag{3.25}$$

For identical power detectors over all five-port outputs, the three output voltages $v_{out-1}(t), v_{out-2}(t)$ and $v_{out-3}(t)$, may be represented as a combination of (3.25) and (3.16). Thus, we obtain:

$$\begin{aligned} v_{out-i} &= D\{\alpha_i A_{LO}\cos(2\pi f_{LO}t + \varphi_i) \\ &+ \beta_i A_{RF}\left[I(t)\cos(2\pi f_{RF}t + \phi_i) - Q(t)\sin(2\pi f_{RF}t + \phi_i)\right]\}^2 \end{aligned} \tag{3.26}$$

The terms α_i and β_i are, respectively, the magnitude of A_i and B_i, and φ_i and ϕ_i are, respectively, the argument of A_i and B_i. By manipulating equations [98] and supposing $f_{RF} = f_{LO}$, we obtain the expressions of the output voltages $v_{out-i}(t)$ of the five-port discriminator:

$$\begin{aligned} v_{out-i} &= \frac{D}{2}\alpha_i^2 A_{LO}^2 + \frac{D}{2}\beta_i^2 A_{RF}^2\left(I^2(t) + Q^2(t)\right) \\ &+ D\alpha_i\beta_i A_{LO} A_{RF}\left[I(t)\cos(\gamma_i) + Q(t)\sin(\gamma_i)\right] \end{aligned} \tag{3.27}$$

where $\gamma_i = \phi_i - \varphi_i$. We are interested in the third term of (3.27), which contains the desired signal I/Q hidden by the other terms. Therefore, a calibration procedure must be applied to reject the dc offset (first term) and the even order term, and to regenerate the I/Q signals using equation (3.24).

3.2.2 Calibration Principle

The calibration procedure determines three complex constants a_{cal}, b_{cal} and c_{cal} to regenerate the complex envelope from the three output voltages using equation (3.24). The method is based on the assumption that the power level of the received modulated signal is lower than the power level of the LO. This assumption allows us to neglect the second term of (3.27) and, consequently, it makes $v_{out-i}(t)$ dependent only on the DC component, the I and the Q signals. Calibration can be performed in 2 steps. First, an RF signal with a known IQ sequence (length of T symbols) is injected into the input of the five-port circuit, which generates 3 output voltages. The dc-offset is evaluated by averaging them over all samples. After dc-offset subtraction, these output voltages are used to solve:

$$V_{out} \begin{pmatrix} a_{cal} \\ b_{cal} \\ c_{cal} \end{pmatrix} = K_{SEQ} \tag{3.28}$$

$$\text{with} \quad V_{out} = \begin{pmatrix} \tilde{v}_{out-3}(1) & \tilde{v}_{out-4}(1) & \tilde{v}_{out-5}(1) \\ \vdots & \vdots & \vdots \\ \tilde{v}_{out-3}(T) & \tilde{v}_{out-4}(T) & \tilde{v}_{out-5}(T) \end{pmatrix} \quad \text{and} \tag{3.29}$$

$$K_{SEQ} = \begin{pmatrix} I(1) + jQ(1) \\ \vdots \\ I(T) + jQ(T) \end{pmatrix} \tag{3.30}$$

$\tilde{v}_{out-i}(t) = v_{out-i}(t) - \langle v_{out-i}(t) \rangle$ where $\langle . \rangle$ defines the average. Next, using the deterministic least squares method, the three coefficients are calculated:

$$\begin{pmatrix} a_{cal} \\ b_{cal} \\ c_{cal} \end{pmatrix} = \left(V_{out}^T V_{out}\right)^{-1} V_{out}^T K_{SEQ} \tag{3.31}$$

An easy way to simulate a known sequence of IQ symbols is to set a small frequency-shift (Δf) between the RF and LO generators, both in CW mode. This frequency-shift leads to a continuous and linear phase variation of the complex envelope at the five-port system output. If the generators are well synchronized and f remains constant, for T snapshots and sample frequency $f_s = T\Delta f$, the known IQ sequence corresponding to this complex envelope variation may be represented by:

$$\begin{pmatrix} I(1) + jQ(1) \\ \vdots \\ I(T) + jQ(T) \end{pmatrix} = \begin{pmatrix} \cos(2\pi/T) + j\sin(2\pi/T) \\ \vdots \\ \cos(2\pi k/T) + j\sin(2\pi k/T) \\ \vdots \\ \cos(2\pi) + j\sin(2\pi) \end{pmatrix} \tag{3.32}$$

In order to validate this calibration technique, the measurement setup shown in Fig. 3.13 is carried out. Two RF generators, namely, Marconi 2031 and HP 4432B, are connected to input ports 1 and 2 of the five-port reflectometer, respectively. A 10 MHz clock synchronizes both generators and a frequency difference of $\Delta f = 100$ Hz is set between the RF input signals

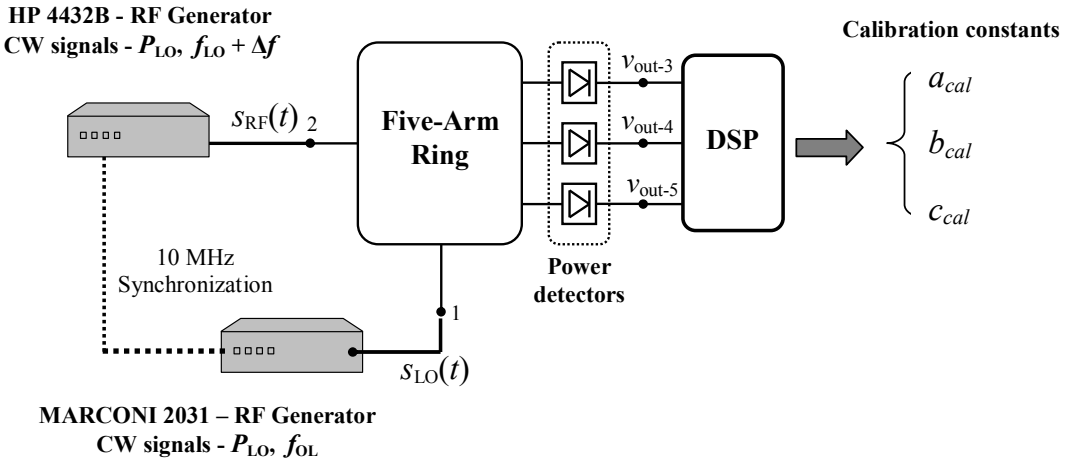

Figure 3.13: Measurement setup for five-port calibration.

$s_{RF}(t)$ and $s_{OL}(t)$. In order to simulate 100 IQ symbols equally distributed on a circle in the complex plane, the sampling frequency of the acquisition board is set at $f_s = 10$ KHz. The carrier frequency is 2.4 GHz and the RF generators are set to supply $P_{OL} = 0$ dBm and $P_{RF} = -20$ dBm of power.

After performing measurements and dc-offset subtraction, the voltages $\tilde{v}_{out-3}(k)$, $\tilde{v}_{out-4}(k)$ and $\tilde{v}_{out-5}(k)$ $(k \in [1, T])$ are used to resolve (3.31). From a_{cal}, b_{cal} and c_{cal}, the complex envelope of measured signals may be calculated using (3.28). As a result, the complex envelope, seen in Fig. 3.14, is useful to distinguish the calibration performance. If symbols are equally distributed along a circle, the generated calibration constants are reliable.

The normalized calibration constants are $a_{cal} = -0.48 + j\ 0.15$, $b_{cal} = 0.86 + j\ 0.50$ and $c_{cal} = -0.1 - j\ 0.42$. The result presented in Fig. 3.14 confirms the efficiency of the method.

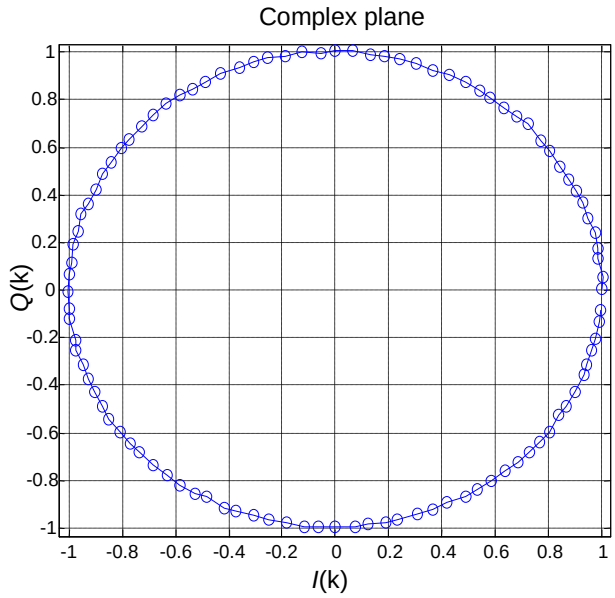

Figure 3.14: Normalized complex envelope after five-port calibration. $P_{OL} =$ 0 dBm and $P_{RF} = -20$ dBm. $f = 2.4$ GHz.

3.3 Conclusion

In this chapter, we presented the five-port circuit made up of a linear RF circuit with five accesses and three power detectors. A description of this circuit and its implementation in microstrip technology for frequencies around 2.4 GHz was presented. The characteristics of the five-arm ring and the power detector features were then explained. The complex envelope can be evaluated by making power measurements of the five-port outputs. We presented the procedure for recovering the complex envelope of RF signals from these three baseband measures. In order to accomplish power detection over a large dynamic, a linearization fitting of the power detectors are employed. A calibration procedure is used to set aright the five-port imperfections and compensate phase and amplitude losses in the system cables.

Chapter 4

Digital beamforming system using Five-Port reflectometer

INTRODUCTION

Modern communication systems such as the internet, online shopping, video telephones, etc. allow users to access multimedia services at a high data rate. Consequently, new challenges for the improvement of the communication link emerge, including interference and transmitted energy reduction, and increased range and capacity. In upcoming years, smart antennas, such as beamforming systems, will be massively employed as a high-performance solution to these challenges [112].

The usual communication systems use omnidirectional and sectorised antenna at a base station, whereas beamforming systems use an antenna array to point the main lobe of the radiation pattern toward the useful signal direction (or look direction) and the nulls toward jammer directions, thereby enabling the introduction of an additional multiple access technique known

as Spatial Division Multiple Access (SDMA).

We introduce a digital beamforming system for reception using the five-port technique instead of classical I-Q demodulators. The system proposed is a hybrid architecture in which beamforming is carried out in the baseband after down conversion. The difficulty in designing and implementation cost of reliable variable phase shifters and attenuators [113, 114] for smart antenna applications makes the weighting process performed in the digital domain a desirable option for future communication systems.

Both advantages and drawbacks of five-port discriminators are depicted in Chapter 3. In digital beamforming systems, the same signal in the antenna array output may be used in SDMA systems to generate different radiation patterns according to the user's location. That is, different users (or sets of users) are focalised simultaneously, working as a parallel architecture.

The drawback of the system is the number of necessary demodulators that must be equal to the number of antennas. According to [115], this inconvenience can be alleviated using a fast RF switch for multiplexing the signals from the array element outputs into a single RF demodulator.

In real communication systems, the beamforming system must be adaptive in order to take into account propagation channel variability due essentially to users' mobility. Despite the fact that measurements performed in this work were carried-out in a stationary propagation channel and the signal demodulation and beamforming used a non real-time process, the methods employed are valid for working in a real-time process with non-stationary channels.

Similarly, the discrimination between the jammers and useful signal is

resolved independently from the beamforming system and is not presented in this work. In communication systems, this discrimination may be done by using a reference signal such as a training sequence or PN code [116].

In Section 4.1, some of the best known beamforming techniques are briefly described. The beamformers and pattern synthesis techniques employed in this work are then depicted, and simulations of radiation patterns using these techniques are performed in Section 4.2. System performance is tested in Section 4.3 by measuring the bit error rate for different numbers of antenna array elements.

4.1 Abstract of best known techniques

In recent years, antenna array processing has been widely researched and a number of algorithms have been developed for detecting targets or maximising power toward a desired source in radar and sonar systems, or for attenuating the effects of interference in order to ensure an acceptable signal to noise rate in the communication link [112]. Some of these techniques are briefly described below.

The Multiple Sidelobe Canceller (MSLC) approach [12] is probably the oldest beamforming technique. A main antenna is highly directive toward the look direction and is not weighted, whereas some auxiliary antennas have their outputs adaptively weighted. The technique consists of subtracting the weighted and summed signals of the auxiliary antennas from the output signal of the main antenna. The auxiliary antenna weights are adaptively computed by minimising this subtraction. A more precise technique consists

of computing antenna weights by maximising the signal to noise rate [117] at the system output. The drawback of this technique is the need for a priori knowledge on the noise covariance matrix.

The null-steering beamformer referred to as Dicanne [118] is used to cancel a plane wave arriving from a known direction and thus produces a null in the response pattern toward the DoA of the plane wave. This is carried-out by estimating the signal arriving from the direction of the jammers using a conventional beamformer [119] and then substracting the result from each element. This technique could be repeated for multiple interference cancellation, but it becomes increasingly cumbersome as the number of interferences grows.

Some array applications require several fixed beams that cover an angular sector. In this case, fixed phase shifters, 90° hybrids, transmission lines and directional couplers can be used in association with techniques such as the Butler matrix [120] and Blass matrix [121] to perform fixed beams. Fixed beams can also be formed by using lens antennas such as the Luneberg lens or Rotman lens with multiple feeds.

The Linearly Constrained Minimum Variance (LCMV) beamformer [122] is designed by minimising the array output power subject to a set of linear constraints. It is assumed that the signal arriving from the look direction has a desirable gain, whereas interfering signals have gains equal to zero.

Griffiths and Jim proposed an efficient implementation of the LCMV method, which is referred to as the Generalised Sidelobe Canceller (GSC), where the constrained optimisation problem is transformed to an unconstrained optimisation problem [123]. GSC is a two-stage scheme. The first

stage takes the array signals as input and produces a set of multiple outputs, which are then weighted and combined in the second stage to produce the array output. This two-stage concept is called beam spacing processing and has been extensively studied [124, 125, 126].

Radiation pattern synthesis can be carried-out by controlling the array excitation in order to produce low sidelobe patterns or very accurate approximations of chosen radiation patterns. The array excitation at the input of antennas may use defined distributions of the magnitude of signals. This is referred to as line sources and are used to control the sidelobe level and beamwidth, such as the Dolph-Chebyshev and Taylor synthesis [13].

Classically, antenna weights can be adaptively updated by means of stochastic approaches such as LMS (least mean square) or RLS (recursive least square) [127] that use closed loop systems. These systems use feedback, which is derived from the system output. The steady-state is reached after a convergence time that varies according to the technique used. Other optimisation techniques use a reference signal to generate an error signal that is used to control the weights [12, 128]. Weights are adjusted such that the mean square error (MSE) between the array output and the reference signal is minimised.

However, some beamforming systems can overcome the need for the feedback present in adaptive systems, since optimum antenna weights can be computed directly from the direction of arrival of useful and interfering signals [115]. In this way, a open loop system of one stage is carried out in this work.

Beamforming for mobile communication systems

The implementation of beamforming for communication systems on compact and handheld arrays is a recent area of research. In 1988, Vaughn [129] achieved an adaptive beamforming that worked for units moving at pedestrian speeds.

In 1999, Braun [130] reported indoor experiments using a single stationary narrowband transmitter and a two-element handheld antenna array. In [131], Dietrich reports an investigation of adaptive beamforming performance using four array elements with different polarisation configurations. The system was tested in indoor, rural, suburban and urban environments.

An introduction to digital beamforming for mobile communications is found in [132]. More recently, Hattenberger [115] studied ADC and digital circuit performance, such as DSP (Digital Signal Processor) and FPGA (Field Programmable Gate Array), in order to propose solutions for hybrid digital beamforming.

The implementation of the beamforming system proposed in this chapter aims to maximise the useful signal strength at the system output as well as attenuate strong interference. No sufficient measurements were carried-out in different environments to compare the system performance to other experiments. Array antenna, RF and digital circuits, signal bandwidth and propagation channel configurations were used according to available conditions in the laboratory and do not correspond to the features of other systems for relevant comparisons.

Among the best known beamforming techniques presented above, a simple

one-stage structure with no need for feedback is chosen. The signal model and algorithms used in the beamforming procedure are described in the next section.

4.2 Antenna array processing

Similarly to the principle of DoA estimators described in Chapter 2, the signal modeling for the beamforming techniques used in this work supposes far-field conditions, a homogeneous medium and a narrowband signal. The signal bandwidth is subject to the following condition: The modulation function must not vary between the arrival time at the first and last array elements. That is, the crossing time is ignored in comparison to the inverse of the signal bandwidth.

We assume N signals s_n impinging on a uniform linear array (ULA) of M elements ($N < M$) from N different sources (see Fig. 2.1 in Chapter 2), where one source radiates the useful signal, while $N-1$ sources radiate undesired signals and are considered as strong agents of noise. Although these signals may share the same frequency channel, they are assumed to be uncorrelated, which is not uncommon in communication systems.

Let $y_m(t)$ denote the total signal induced due to all N directional sources and background noise on the mth array element, given by:

$$y_m(t) = \sum_{n=1}^{N} g_r(\theta_n) e^{-j2\pi f_o \tau_m(\theta_n)} s_n(t) + n_o(t) \tag{4.1}$$

where $n_o(t)$ is the random noise component assumed AWNG with zero mean

and variance equal to σ_o^2. $\tau_m(\theta_n)$ is the time delay of the nth source between a reference antenna and the mth array element and can be modelled as (1.1). The parameter $g_r(\theta_n)$ is the radiation pattern of the mth element at the angle θ_n. Regarding the antenna array, the equivalent baseband of (4.1) at time k can be expressed in matrix notation as in (2.1):

$$x[k] = As[k] + n_o[k] \tag{4.2}$$

The matrix $A \in C^{M \times N}$ made up of N steering vectors $a(\theta_n)$ and the vectors $x[k]$, $s[k]$ and $n_o[k]$ are depicted in Chapter 2. In this model, instead of impinging signals as a result of multipath propagation, the signals picked up by antennas are from independent sources.

4.2.1 Beamformer models

Consider a narrowband beamformer, shown in Fig. 4.1. After down-conversion, signals associated to each element are multiplied by a complex weight and summed to form the array output. From the figure, it follows that an expression for the array output $x_w[k]$ is given by:

$$x_w[k] = \sum_{m=1}^{M} w_m^* x_m[k] \tag{4.3}$$

where $(.)^*$ denotes the complex conjugate. Representing the weights of the beamformer in matrix notation as:

$$w = [w_1, w_2, ..., w_M]^T \tag{4.4}$$

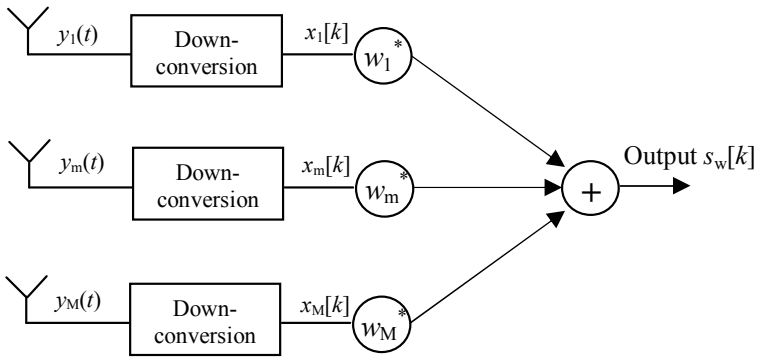

Figure 4.1: Digital narrowband beamformer structure.

the output of the beamformer becomes:

$$x_w[k] = w^H x[k] \tag{4.5}$$

where the superscripts T and H, respectively, denote the transpose and complex conjugate transpose of the vector or matrix. Throughout this chapter, w and $x[k]$ are referred to as the weight vector and the signal vector, respectively.

If the components of $x[k]$ can be modelled as zero mean stationary processes, then for a given w, the mean output power of the processor is given by:

$$P(w) = E[x_w[k]x_w^*[k]] = w^H R_x w \tag{4.6}$$

where $E[.]$ denotes the expectation operator and R_x is the cross-spectral matrix. R_x can be estimated using the covariance matrix of $x[k]$ given by (2.4). Replacing w in (4.6) by the steering vector of a signal arriving from a

known direction θ_o, we obtain maximum output power $P(\theta)$ in this direction.

$$P(\theta) = a(\theta_o)^H R_x a(\theta_o) \tag{4.7}$$

This simple approach is known as the conventional beamformer or delay-and-sum beamformer [119] and its only purpose is to maximise power in the look direction. This is achieved by replacing $a(\theta_o)$ in (4.7) by the estimated steering vector of the signal in the look direction $\hat{a}_{US}(\theta)$, which is determinated previously.

The LCMV algorithm developed by Veen [133] and the unconstrained beamformer [12] for minimising interference effects from the total signal received are depicted below.

LCMV method

The principle of the LCMV technique is to minimise output power under the condition that the signal arriving from the look direction has a desired gain g_w, whereas interfering signals have gains equal to zero. Assuming the response vector u a column vector of N real elements containing the chosen gains, and the constraint matrix $C_{\hat{a}} \in C^{M \times N}$ made up of the estimated directional information $\hat{a}_{US}(\theta) \in C^{M \times 1}$ and $\hat{A}_I(\theta) \in C^{M \times (N-1)}$ of useful and interfering signals, respectively, the relation between w, u and $C_{\hat{a}}$ is given by:

$$C_{\hat{a}}^H w = u \tag{4.8}$$

$$\begin{bmatrix} \hat{a}_{US}^{H}(\theta) \\ \hat{A}_{I}^{H}(\theta) \end{bmatrix} w = \begin{bmatrix} g_w \\ 0_{N-1} \end{bmatrix}. \tag{4.9}$$

where $\hat{A}_I(\theta) = [\hat{a}_{jam_1}, \ldots, \hat{a}_{jam_{N-1}}]$ is the concatenation of $N-1$ estimated steering vectors of the jammers and 0_{N-1} is a zero column vector made up of $N-1$ elements.

The constraints are assumed linearly independent. Thus, the rank of $C_{\hat{a}}$ is N. Furthermore, the number of linear constraints N must be less than the number of elements M. Therefore, from (4.6) and (4.9), we seek the weight vector w that satisfies the following criterion:

$$\min_{w} w^H R_x w \text{ under the constraint } C_{\hat{a}}^H w = u \tag{4.10}$$

Assuming $g_w = 1$, the above equation is resolved by using the Lagrange multiplier [115]. The optimum weight vector is:

$$\hat{w} = R_x^{-1} C_{\hat{a}} (C_{\hat{a}}^H R_x^{-1} C_{\hat{a}})^{-1} u \tag{4.11}$$

Substituting (4.11) in (4.6), we find the mean power relation for the LMCV technique.

Unconstrained beamformer

Let an M-dimensional complex vector w represent the weights of the beamformer shown in Fig. 4.1 that maximise the output SNR. For an array that

is not constrained, an expression for w is given by [12, 134, 135]:

$$\hat{w} = \mu_o \hat{R}_{N+I}^{-1} \hat{a}_{US}(\theta) \tag{4.12}$$

where $\hat{R}_{N+I}$ is the estimated array correlation matrix of the noise plus interference signals, that is, it does not contain any signal arriving from the look direction; and μ_o is an arbitrary constant.

The proposed system depicted in the next section assumes the power of thermal noise much less than the sum of power of all interfering signals, since the useful signal is narrowband. Thus, the unconstrained beamformer can be expressed as:

$$\hat{w} = \mu_o \hat{R}_I^{-1} \hat{a}_{US}(\theta) \tag{4.13}$$

where $\hat{R}_I$ can be calculated using:

$$\hat{R}_I = \hat{A}_I(\theta) \hat{A}_I(\theta)^H \tag{4.14}$$

By replacing (4.14) in (4.13), the unconstrained beamformer can be given by:

$$\hat{w} = \mu_o (\hat{A}_I(\theta) \hat{A}_I(\theta)^H)^{-1} \hat{a}_{US}(\theta) \tag{4.15}$$

For both techniques, the direction of arrival of useful and interfering signals as well as the covariance matrix of the signal vector are estimated as shown in Chapter 2.

By using the mean power relation in (4.6) for LMCV and unconstrained beamformers, the simulated radiation pattern for both techniques is plotted

as shown in Fig. 4.2. The radiation pattern of a conventional beam towards the look direction is also compared. A uniform linear array of 10 omni-directional elements and inter-element spacing equal to $\lambda/2$ is used.

Three interfering signals and a useful signal impinge on the antennas with different DoAs. The jammers arrive on the array with azimuth angle 47°, 13° and −52°, whereas the look direction is 15°. All impinging waves are assumed to be plane and the signals are assumed to be narrowband and uncorrelated. In Fig. 4.2, the vertical dashed lines corresponds to the DoA of the true signals.

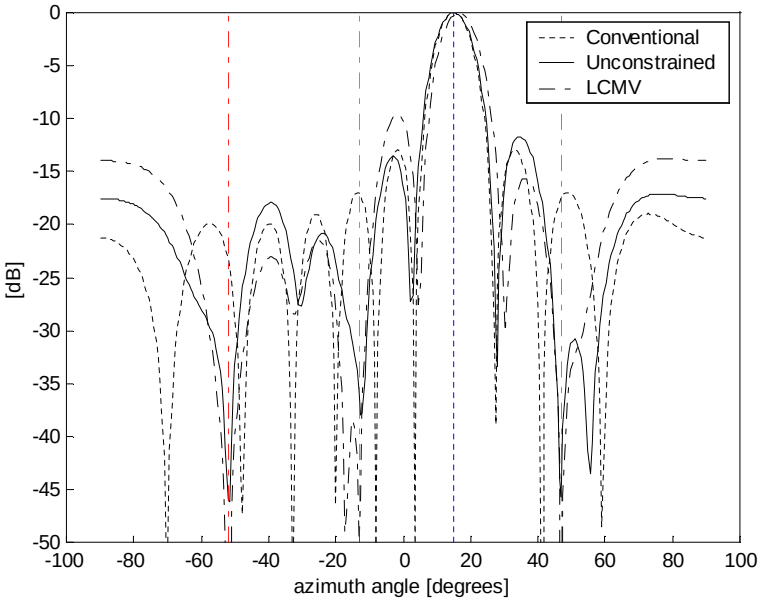

Figure 4.2: Simulated radiation pattern computed according to different techniques. $M = 10$. The DoA of the jammers is 47°, −13° and −52° and the DoA of the useful signal is 15°.

The radiation patterns illustrated above show an unbiased angular response of the conventional and unconstrained beamformers in focalising on the look direction. The LCMV radiation pattern presents a slight displace-

ment of less than 2° of the main lobe peak. It is also observed that the conventional beamformer performs the narrower main lobe.

As expected, the conventional beamformer pattern does not present any null with regard to the direction of the jammers. Attenuations from 38 dB to 46 dB are observed at the DoA of the jammers when the unconstrained beamformer is used, whereas attenuations exceed 50 dB when the LCMV beamformer is used.

The jammer attenuations performed by both the LCMV and unconstrained beamformers are sufficiently high and in comparison to the look direction gain, the difference between them may be ignored. The better performance of the unconstrained beamformer in steering toward the look direction without bias suggests the use of this technique.

4.2.2 Pattern synthesis

According to [13], beamwidth and sidelobe levels of the radiation pattern depend on the magnitude of weighting constants. The radiation pattern control is based on the displacement of nulls in the radiation pattern. That is, the zeros of the pattern function are adjusted so that the desired radiation pattern is created. Array pattern zero locations are related to the distribution of line sources (or aperture taper) by means of a variance of the Fourier transform.

The normalised broadside radiation pattern in far field of a line source of length $M \times d$ as a function of the azimuth angle Φ is given by:

$$S(u) = \frac{\sin \pi u}{\pi u} \tag{4.16}$$

where $u = \frac{Md}{\lambda} \sin \Phi$. This sinc function is a Fourier transform of a rectangular line source with 13 dB of sidelobe level. This level is relatively high and can be attenuated by using a polynomial, such as the Taylor polynomial, to equate the array distribution and produce the desired sidelobe level.

Taylor line source synthesis

The array distribution defined as a function of the element position (ς) is computed by means of the Taylor polynomial [13] by:

$$h(\varsigma) = S(0) + 2 \sum_{u \in \Omega} S(u) \cos \left(\frac{2u\pi\varsigma}{Md} \right) \tag{4.17}$$

where $S(u)$ is defined as follows [136]

$$S(u) = \frac{\sin \pi u}{\pi u} \prod_{u \in \Omega} \frac{1 - u^2/u_n^2}{1 - u^2/n} \tag{4.18}$$

The values u_n represent the η nulls of $S(u)$ and $\Omega = 1, 2, \ldots, \eta$. Assuming that:

$$A_{SL} = \frac{1}{\pi} \cosh^{-1} r \tag{4.19}$$

and

$$\sigma = \frac{\bar{n}}{\sqrt{A_{SL}^2 + (\bar{n} - \frac{1}{2})^2}} \tag{4.20}$$

u_n may be expressed by:

$$\begin{aligned} u_n &= \pm\sigma \left[A_{SL}^2 + \left(n - \frac{1}{2} \right)^2 \right]^{\frac{1}{2}} \text{ for near sidelobes } (1 \leq n \leq \bar{n}) \\ &= \pm n \text{ for far sidelobes } (\bar{n} \leq n \leq \eta) \end{aligned} \tag{4.21}$$

where r is the sidelobe level that is usually mentioned in dB form ($SL_{dB} = 20\log_{10} r$) and $\bar{n} \in \Omega$ is an optimized integer for each array configuration. Far sidelobes represent lobes away from the main beam, whereas near sidelobes are closer to the main lobe.

According to (4.21), the Taylor synthesis produces a pattern function with zeros far from the main beam at locations that correspond to the uniform illumination, whereas zeros closer to the main beam are chosen in a similar way as in the Chebyshev pattern [137]. For small $\bar{n}$, near sidelobes are not controlled and distortions may occur in the radiation pattern. For large $\bar{n}$, $h(\varsigma)$ may experience a non-monotonic distribution [13], which is impractical for arrays of few elements. Optimised values of $\bar{n}$ for different array configurations are suggested in [138].

Fig. 4.3 and Fig. 4.4 show the simulation of a radiation pattern synthesis for three different spatial windows: rectangular (uniform), Taylor and Chebychev distribution for $M = 20$, $SL_{dB} = 30$ dB and $\bar{n} = 4$. It is clear that the sidelobe control is only performed for Taylor and Chebychev distributions and that for uniform distribution the narrowest main beam is synthesised.

In Fig. 4.3, where the line-sources are plotted, a non-monotonic behaviour in the array extremities for the Chebychev distribution is seen, which constitutes a disadvantage. The hybrid control of zeros for the Taylor spatial window performs lower levels of far sidelobes, even below SL_{dB}, as seen in Fig. 4.4.

In the case of a non-stationary propagation channel, interfering signals may escape from the narrow null zones before being held again. Attenuated sidelobe levels can avoid a sudden drop of the signal to interference plus noise

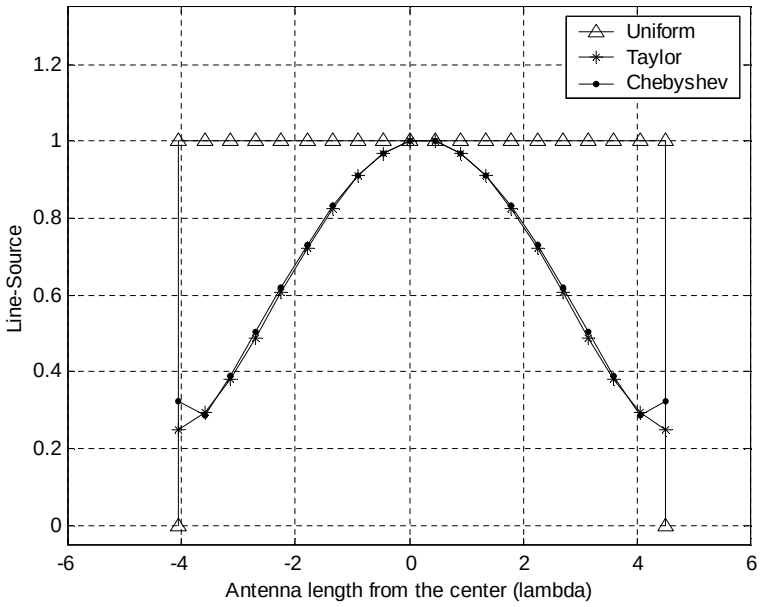

Figure 4.3: Line-Source for $M = 20$ and $SL_{dB} = 30$ dB.

rate (SINR) in such a situation. A combination of both pattern synthesis and beamformer concepts may be used to control the radiation pattern of an antenna array at best. The aim is to steer the array in the look direction, produce nulls in the jammer direction and control the beamwidth and sidelobe level.

Some conflicts may occur when the pattern synthesis and beamformer are used together, as will seen be in next section, and trade-offs must be respected.

4.3 Experimental setup

In a non-reflective environment, the proposed system [139] is tested using the following configuration: at the level of the emitter, two directive antennas

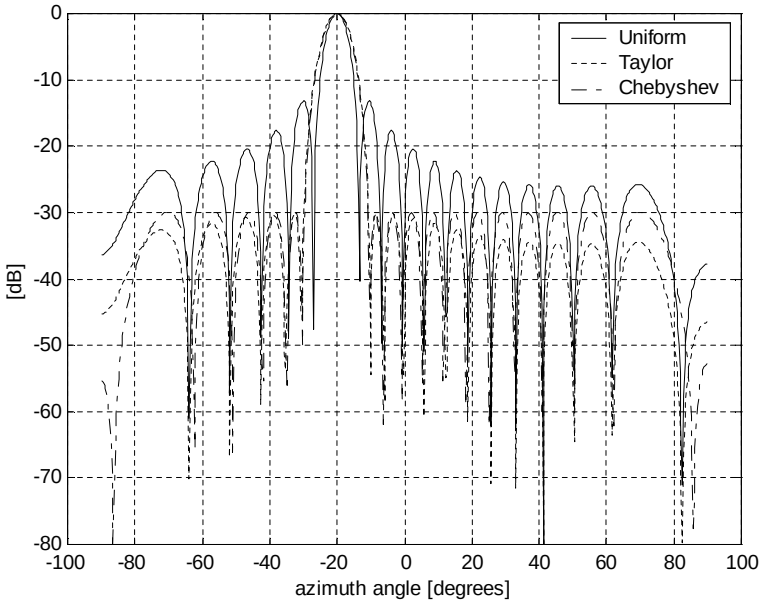

Figure 4.4: Radiation Pattern corresponding to the Line-Source distributions presented in Fig. 4.3.

radiate the interferers and are located at an angle of 36° and −34° to the orthogonal axis of the antenna array baseline of the receiver. Another antenna located at angle 18° radiates the useful signal. All antennas are placed 6 meters from the reception array.

At reception, a uniform linear array (ULA) of seven antenna elements is used. The antenna elements are positioned as a ULA on the H-plane of the antenna with element spacing equal to $\lambda/2$. A low-noise amplifier with a gain $G_{LNA} = 20$ dB and a noise factor $NF = 2.5$ dB is integrated to each antenna element. Quasi-yagi antennas [140] with gain $G_{Yagi} = 6$ dB implemented in planar technology are used for both the reception and transmission systems as radiating elements. The mutual coupling of quasi-yagi antennas is assumed very small and thus is ignored.

The antenna features and the receiving circuitry, including five-port discriminators used as demodulators, are better depicted in Chapters 3 and 5.

The frequency of the received signals is around 2.4 GHz and the data rate is about 5 kbps using a QPSK modulation. A slight difference in the carrier frequency of the signals makes them incoherent. After down-conversion, the DSP performs the signal demodulation, the direction of arrival (DoA) estimation of the RF signals and the evaluation of the weighting factors for the digital beamforming process. Using (4.5), the signal vector $x[k]$ is then weighted and the bit error rate (BER) can be evaluated.

Two experimental setups are performed. They are carried out in a large room with a high ceiling and walls spaced far apart in order to reproduce a non-reflecting environment. Absorbers cover all the floor space between the transmitters and the receiver. The power level of arriving signals is measured by a wattmeter at the level of the receiving antennas.

In the first setup, the power of the jammers at the receiver is about -62.5 dBm and -57.8 dBm and the power of the useful signal varies from -67.5 dBm to -64.5 dBm. In Fig. 4.5, the floor plan of the measurement site is illustrated. The DoA of the three signals is well estimated (see Fig. 4.6) by the five-port/MUSIC system.

Fig. 4.7 shows the simulated radiation pattern for 7 elements when using two different weighting models. The Model 1 is expressed by [13, 119]:

$$\hat{w} = I_M \left[\mathrm{diag}(\hat{a}_{US}(\theta))h(\varsigma)\right] \tag{4.22}$$

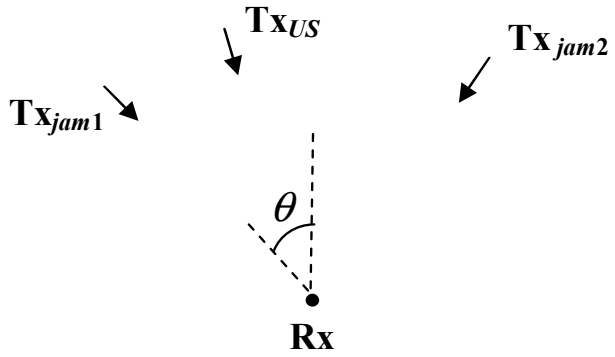

Figure 4.5: Floor plan of the measurement site for the first experiment. Rx, Tx_{US}, Tx_{jam1} and Tx_{jam2} correspond to the receiving antenna, transmitter of useful signals and transmitters of jammers, respectively.

and uses only information $\hat{a}_{US}(\theta)$ from the DoA of the useful signal and $h(\varsigma)$ (4.17). That is, the vector w is computed according to the conventional beamformer in association with pattern synthesis. $I_M \in C^{M\times M}$ and diag(.) denote the identity and diagonal matrices, respectively.

The Model 2 is computed using the unconstrained beamformer (4.15) and pattern synthesis (4.17).

$$\hat{w} = (\hat{A}_I(\theta)\hat{A}_I(\theta)^H)^{-1}\,[\mathrm{diag}(\hat{a}_{US}(\theta))h(\varsigma)] \tag{4.23}$$

For both models, SL_{dB} is set 20 dB by the Taylor spatial window. Lower sidelobe level could produce a very large beamwidth, since the antenna aperture is relatively small. The element pattern $g_r(\Phi)$ on the H-plane of the antenna was determined by simulation and is taken into account in order to compute the array radiation pattern.

Nulls are observed in the radiation pattern at the direction of arrival of the interfering signals when using Model 2. In Model 1, one of the interfering

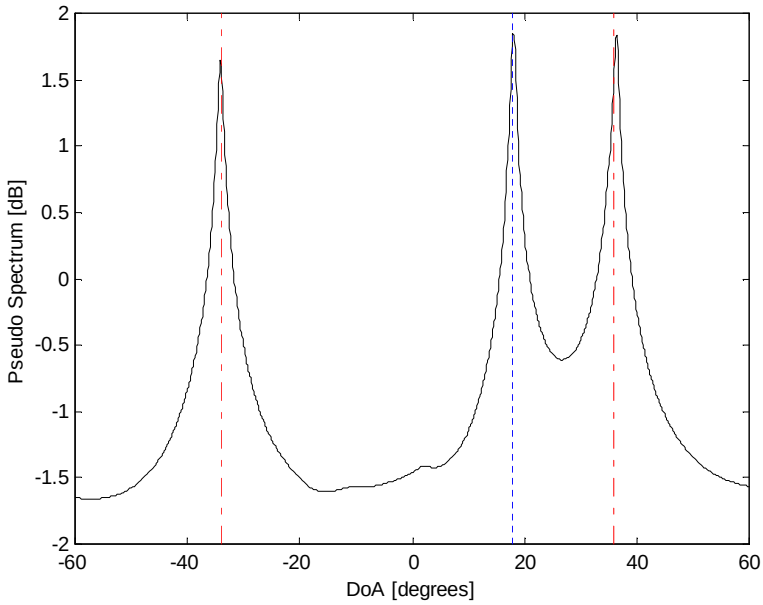

Figure 4.6: DoA Estimation (MUSIC) of three non-coherent signals for $M = 7$. Transmitters situated at the azimuth angles $-34°$, $18°$ and $36°$.

signals is incident on the main lobe because of its large beamwidth. It causes an attenuation of 10 dB, which is less than a classical rectangular sidelobe level.

Vertical and horizontal dashed lines denote the DoA estimates of incident signals and the sidelobe level set by the line source, respectively.

For both models, far sidelobes are observed with very low levels due to the directivity of the elements. One near sidelobe could not be controlled by the Taylor tapering due to the divergence between u_n and the DoA of the jammers when using Model 2. Errors due to the difference between pattern zero locations and the direction of arrival of the jammers can be alleviated by reducing the sidelobe level set by the taper.

Fig. 4.8 illustrates the bit error rate (BER) as a function of the signal

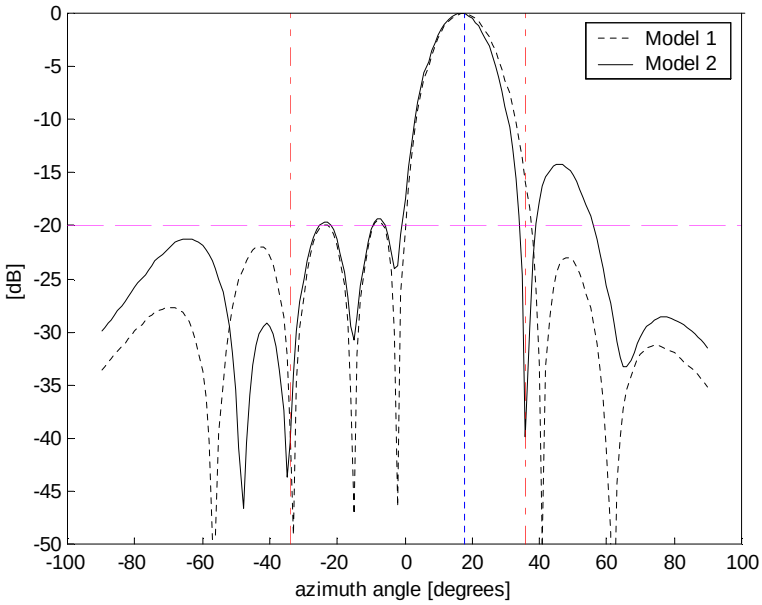

Figure 4.7: Radiation Pattern for M=7 and SL_{dB}=20 dB.

to interference plus noise ratio (SINR) when using Model 2 and 7 elements in the reception array. This graph exhibits the adequate performance of the five-port and beamforming system in demodulating the useful signal even in the presence of high interference.

In the second setup, the same configuration is conserved, but the jammers are removed. Model 1 is used in order to achieve a smaller sidelobe level.

The BER as a function of the power of the useful signal at the input of the receiver with array of 1, 3 and 5 elements is shown in Fig. 4.9. The input power varies from - 92.5 dBm to -87.5 dBm. As expected, better performance for larger arrays is observed because the antenna array gain is directly proportional to the number of elements. A BER of 10^{-3} is achieved when the useful signal power is about -88 dBm and 5 array elements are used.

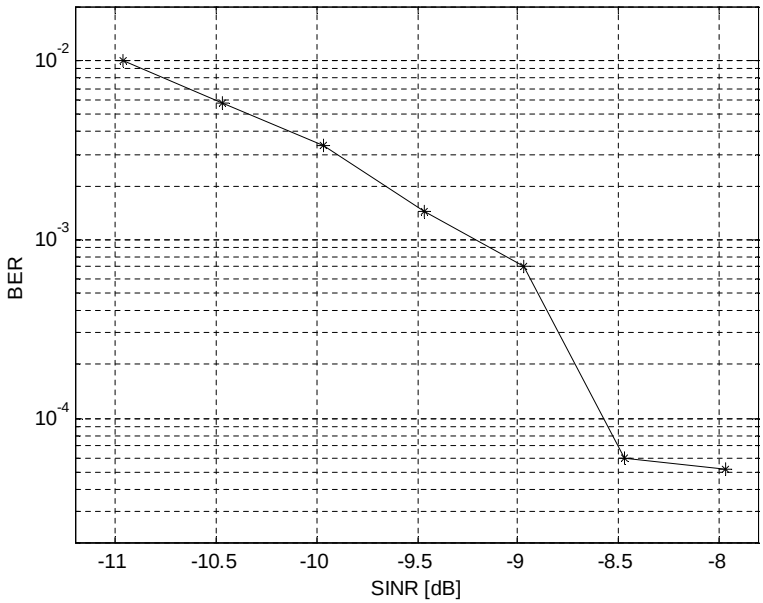

Figure 4.8: BER vs. SINR for jammers with power $P_{jam1} = -62.5$ dBm and $P_{jam2} = -57.8$ dBm and useful signal power varying from -67.5 dBm to -64.5 dBm.

4.4 Conclusion

There are several algorithms used to modify the radiation pattern of an antenna array. Some techniques use a reference signal to steer the array toward a given direction, and others use the DoA and covariance matrix information to control the beams. Synthesis pattern is performed by filtering the excitation of the antenna array.

In this chapter, we presented simulations of the radiation pattern using conventional, unconstrained and LCMV techniques in order to maximise power in the look direction and attenuate the interference level. Uniform, Taylor and Tchebyshev line source syntheses are implemented to simulate the radiation pattern.

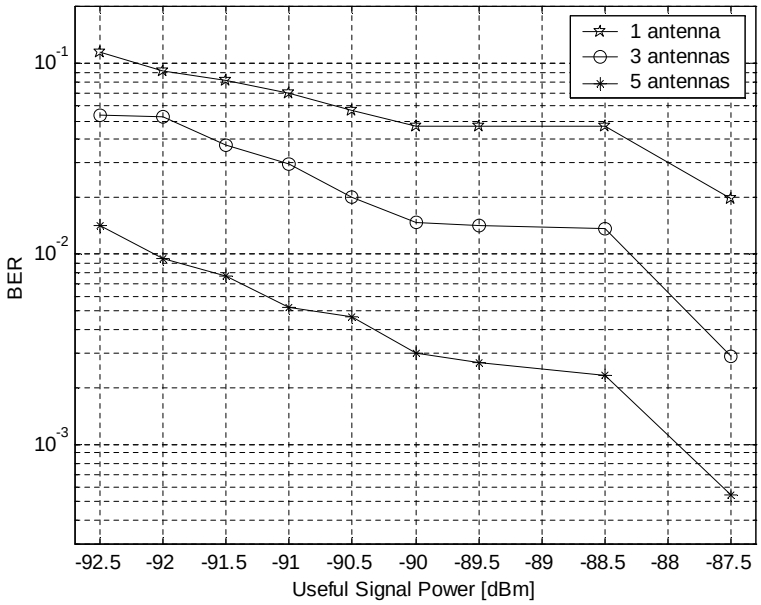

Figure 4.9: BER vs. useful signal power for 1, 3 and 5 antenna elements and useful signal power varying from - 92.5 dBm to -87.5 dBm.

A digital beamforming system using five-port discriminators, conventional and unconstrained beamformer associated with Taylor tapering is then implemented and tested through BER relation. The results in Fig. 4.8 show the ability of the proposed system to perform spatial filtering well and provide higher gain (and smaller BER) in the useful signal direction even in presence of a strong interference level. For BER = 10^{-3}, the SINR is about -9.25 dB.

In the absence of jammers, the linear relation between the antenna array gain and the number of elements are observed in Fig. 4.9. When 5 elements are used, the minimum detectable signal (about -88 dBm) of the receiver defined to a BER of 10^{-3} demonstrates the adequate sensitivity of the system compared to monochannel five-port systems.

However, due to the limited number of measurements and configuration

of the experimental setups, the results could not be compared to those of other existing digital beamforming systems.

Chapter 5

Measurement setups and results

INTRODUCTION

In the present work, we first described the theory and specifications of the chosen sounding technique. Then, a number of tools used for data processing and RF measurements were presented. Finally, a number of experiments carried out through the years of the thesis are presented in this chapter.

The measurement setup of a direction finding system and a channel sounder using five-port discriminators in different configurations are depicted in increasing order of complexity. The quasi-Yagi antenna and the description of the multichannel measurement system, including the calibration procedure, are presented first. Next, simulations of a propagation channel with cables and directive antennas are described, followed by the measurements of an indoor propagation channel.

5.1 Quasi-Yagi antenna implemented in microstrip technology

In order to characterize the propagation channel in the chosen band, the antennas must satisfy a number of features, such as wideband (about 20% around 2.4 GHz), relatively stable radiation pattern in function of frequency, feasible implementation in antenna array, low level of mutual coupling and low production cost.

Among wideband antennas, planar antennas have a number of advantages over wired antennas: Fabrication is easier, the overall dimensions are reduced and this technology enables a feasible association between the antenna and other elements of the RF front end, such as low-noise amplifiers (LNA) [53].

Microstrip antennas that use planar technology consist of an electrical conductor of the desired shape printed on a dielectric material. A ground plan is generally placed under the dielectric.

The quasi-Yagi implemented in microstrip technology [141] (see Fig. 5.1) is a compact, one-layer and linearly polarized antenna and can achieve a large passband. The mutual coupling between two quasi-Yagi antennas is small [142], enabling their use in antenna array applications. Therefore, this technology was chosen as the radiating element for the receiving and transmitting systems.

The antenna features, loss return and radiation pattern are presented in [53]. Vu presents the implemented antenna with passband of about 800 MHz around 2.4 GHz. The antenna radiation is stable in the H-plan with a 3dB bandwidth of 125° where $f_o = 2.4$ GHz. The gain at 0° is about 6 dB and

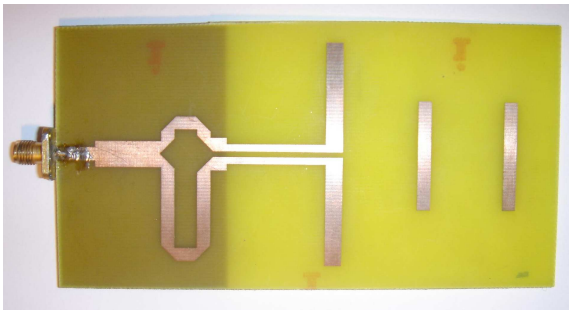

Figure 5.1: Photograph of a quasi-Yagi antenna implemented in microstrip technology for working around 2.4 GHz. Dimensions: 130 × 65.5 mm. Scale 1:2

its mean value over the entire band is about 5.5 dB. The mutual coupling between two elements placed on the H-plane of the antennas is below -17 dB at 2.2 GHz, -19 dB at 2.4 GHz and -23 dB at 2.6 GHz.

The employed substrate is Epoxy, with a dielectric permittivity of 4.1 and the dimensions of the antenna are 65.5 × 13 mm. Each antenna is associated to an LNA of a gain equal to 20 dB from 2.3 to 2.4 GHz. The same substrate used for printing the antenna is used as printed chip board for the LNA. The LNA model is HMC 286 [143] from the Hittite microwave corporation.

5.2 Description of the multichannel measurement system

As reported in Chapter 3, five-port discriminators measure the complex ratio between two input RF signals. When used as a receiver for communication systems, one of the ports is connected to the receiving antenna and another port receives a reference signal known as the local oscillator (OL). Through-

out this chapter, the input signals connected to the receiving antenna and local oscillator are referred to as RF signal and LO signal, respectively.

When a multi-antenna system is used, the LO signal is of great importance for the use of antenna processing techniques that are based on the phase ratio between array elements.

Let us assume an antenna array of M elements, where each element is connected to a single five-port discriminator. If LO signals with the same reference phase Φ are available for all five ports, the ratio $\frac{x_\mu}{x_\nu}$ between the complex envelopes of two arbitrary discriminators μ and ν can represent the phase ratio between the RF signals of the five-ports μ and ν. Consequently, if cables and circuits of identical length are used between antennas and the five-ports, $\frac{x_\mu}{x_\nu}$ can also represent the phase ratio between the μth and νth array elements.

Multitones were chosen as the sounding technique employed in this work and use the same signal that is transmitted and filtered by the propagation channel as the reference signal of the five-port discriminator. A power divider is used to split the generated signal in order to supply the transmitting antenna and local oscillator.

The phase component of the channel transfer function is the key to this technique. The time delay solution is achieved by measuring the phase ratio between responses from different frequencies. The response for each frequency is measured directly from the complex envelope of the five-port.

As the length of cables and circuits in a parallel array system is rarely identical, a calibration procedure is necessary to compensate phase in the RF front end. Calibration also sets reference values in the angle and time

domain as well as the power of input signals.

5.2.1 Calibration of a multichannel system

As stated in Chapter 3, a calibration must be performed to compensate for the five-port imperfections that give rise to an unbalance between output ports.

In the present work, the relative phase between array elements and between frequency tones is important. Thus, the calibration procedure presented in Section 3.2.2 also performs the phase and amplitude compensation.

For a multichannel system, the calibration procedure must be employed for all frequency tones and five-ports (antennas). The calibration is carried out using a transmitter (Tx) with single antenna that radiates the calibrating signals toward a receiving array (Rx), as illustrated in Fig. 5.2. The distance between the calibrating antenna Tx and Rx must ensure a far-field condition and the propagation channel must be non-reflective, such as free space.

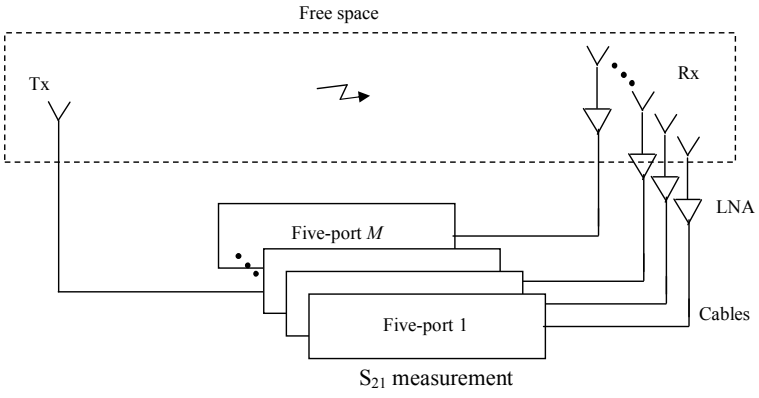

Figure 5.2: Calibration structure of a multichannel system.

As the antenna array has a parallel architecture, the same plane wave

is picked up by all antennas and simultaneously measured by the five-ports. However, the Multitone technique carries out a discrete sweep of frequencies and their corresponding signals are measured as a function of time.

The system configuration during calibration measurements, such as the relative location between the transmitter and receiver, the length of the cables and the power of the transmitter and LO, determines the references for the DoA and time delay estimation.

For detecting the DoA and time delay of the paths, their estimated values must be analyzed according to the positions of Tx and Rx. That is, the orthogonal axis of the antenna array baseline used as the angle reference is the straight line between the calibrating antenna and the geometrical center of Rx. The estimated time delay of a path is compensated by the propagation time in cables and free space measured in the calibration procedure. Since this part of time delay is deleted, the system benefits from the entire observation window ($1/\Delta f$).

According to the calibration principle reported in Section 3.2.2, the effect of an RF signal with a known IQ sequence can be reproduced by setting a small frequency shift between the RF and LO signals. In this case, two generators are used in the calibration procedure and the number of pseudo charges in the complex plan depends on the sampling frequency and the frequency shift between the RF and LO signals. This method is used for calibrating the direction-finding system presented below.

The sounding system is calibrated using only one RF generator and modulated signals. QPSK modulated signals are transmitted using carrier frequencies that change according to the step mode technique. That is, the

carrier frequency changes discretely as a function of time. The local oscillator port receives the CW signal available on the back of the generator. Thus, for each frequency, three calibration constants are computed according to (3.31).

For experiments where multipath phenomena are simulated by directive transmitting antennas, the calibration configuration is as follows: The distance between Tx and Rx is 5.48 m. The transmitted power at the antenna input is about 9 dBm and the power at the LO input is about -15 dBm. A bandwidth of 1 KHz is used and the sampling frequency is set at 8 KHz. Fig. 5.3 shows the normalized complex envelope of measured signals collected for the calibration procedure. These measured data correspond to a specific five-port and frequency.

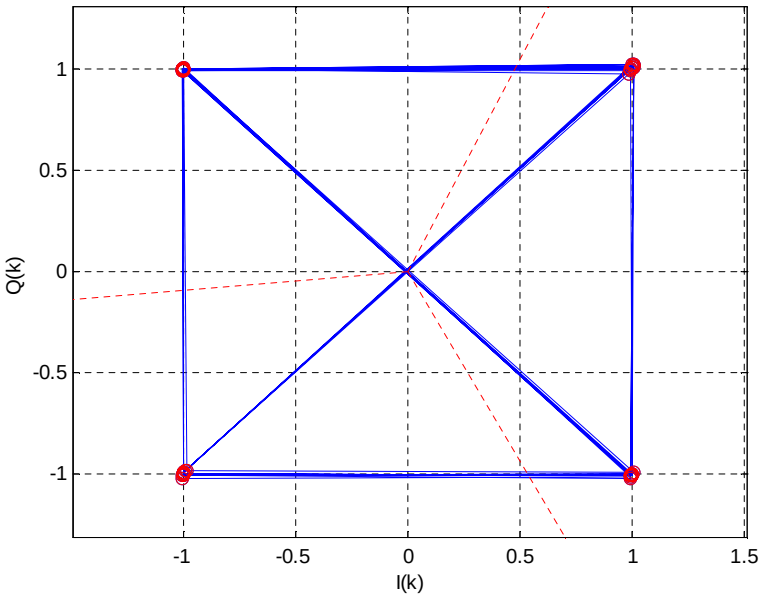

Figure 5.3: Normalized complex envelope after propagation channel calibration at $f = 2.4$ GHz.

The dashed lines indicate the phase of the calibration constants. The square shape of the constellation and the phase balance between the axes of the five-port discriminator signifies that the computed calibration constants are reliable.

For experiments in realistic environments, the calibration strategy was changed. The transmitted power is about 2 dBm. However, the distance between Tx and Rx is reduced to 3.50 m and the power at the LO input is increased to -3dBm to compensate the complex envelope strength. A trade-off between RF and LO power is needed to avoid ADC saturation, in particular in calibration procedure. Since the LO power must be the same for both calibration and channel measurement procedures, strong LO signals is preferable for realistic measurements, as reported in [144].

5.3 Direction finding system

Direct detection of the direction of arrival (DoA) with no frequency conversion simplifies the design of DoA measurement systems and alleviates baseband processing. The phase shift between antennas is directly measured by the five-port to estimate the DoA of RF signals.

5.3.1 DoA system simulation using cables and microstrip circuits

An initial experiment consisting of cables, phase-shifters and power dividers (PD) is implemented for simulating a propagation channel and phase-shift

between virtual antennas. Fig. 5.4 shows the electrical schema, in which two signals are simulated and measured by three five-port discriminators.

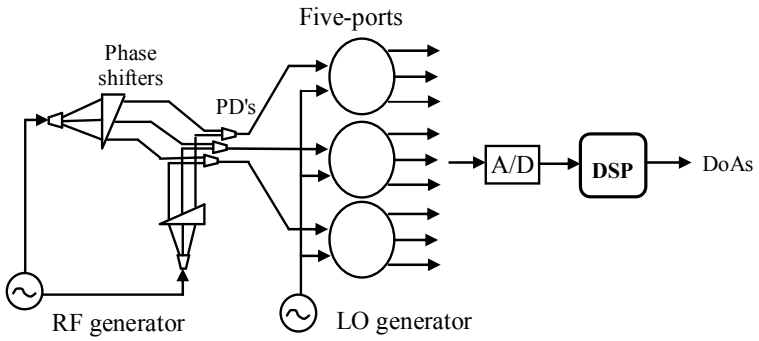

Figure 5.4: Simulation of a direction finding system consisting of cables, phase-shifters, power dividers and five-port discriminators.

This circuit simulates an ideal system, neglecting phase errors due to mutual coupling between elements, geometric non-linearity of the array, parasitic multipath signals and non-plane waves. Phase-shifters and power dividers are implemented in microstrip technology on a FR4 substrate ($\varepsilon_r = 4.7$).

The signals that represent the two plane waves are phase-shifted and summed before reaching the five-ports. This corresponds to the summation of all incident waves on the antenna. The schema in Fig. 5.4 corresponds to a simulation of two coherent signals. A trial with incoherent signals is also performed, in which two generators with a slight frequency shift are used as transmitters.

In order to simulate DoAs of -28° and 14°, phase-shifters of -84.5° and 43.5° between consecutive microstrip lines at 2 GHz is used. A virtual inter-element spacing of $\lambda/2$ was considered for designing the desired phase-shifters. This information is very important for matching the steering vector

to the virtual array geometry.

Two algorithms are used for processing data and estimating DoA. MUSIC is employed as a DoA estimator preceded by Forward-Backward (FB) averaging [11] used for decorrelating coherent sources. The FB averaging technique is a less efficient decorrelating technique than Spatial Smoothing, but is more feasible when antenna arrays of a small number of elements are used.

Fig. 5.5 shows the results of the DoA finding system simulated by cables and microstrip circuits. Accurate values were found for both incoherent and coherent signals after the decorrelating processes. Without using any decorrelation method, detection errors are present for coherent signals.

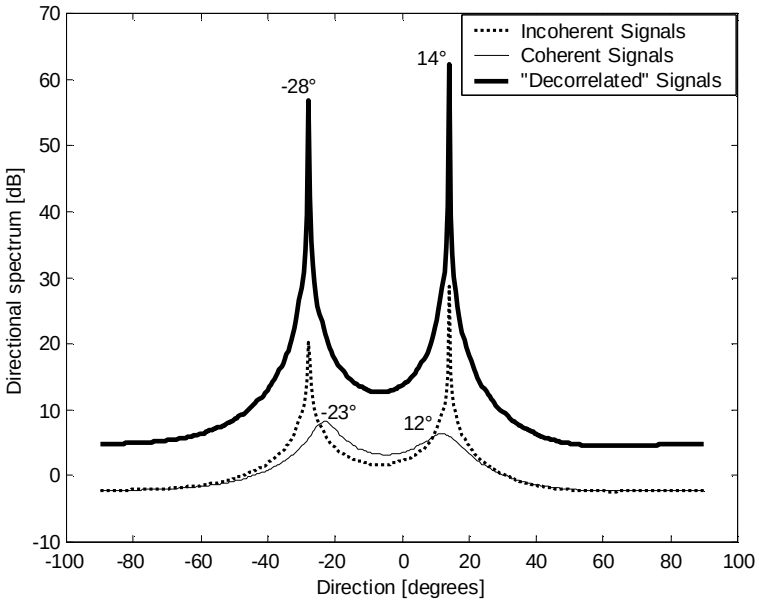

Figure 5.5: Simulation of a direction finding system consisting of cables, phase-shifters, power dividers and five-port discriminators. Theoretical DoAs: -28° and 14°. $f_c = 2$ GHz.

5.3.2 DoA finding experiment using a ULA

As in the beamforming experiments presented in Chapter 4, the experimental setup is carried out in a non-reflective environment. The aim is to avoid any parasitic signal due to the multipath and only consider signals from directive antennas placed at known locations.

At the level of the emitter, three directive antennas are located at an angle of -25°, 16° and 57° to the orthogonal axis of the antenna array baseline of the receiver and radiate the RF signals. All antennas are placed 6 meters from the reception array and only CW signals at 2.4 GHz are transmitted.

At reception, a uniform linear array (ULA) of 8 array elements is used. The elements are positioned as a ULA on the H-plane of the antenna with element spacing equal to $\lambda/2$. A low-noise amplifier with a gain $G_{LNA} = 20$ dB and a noise factor NF = 2.5 dB is integrated to each antenna element. The photograph of the receiving ULA made up of quasi-Yagi antennas and LNAs is shown in Fig. 5.6.

Each antenna element is connected to Port 2 of the five-port discriminator, whereas Port 1 receives the LO signal. Each five-port output is connected to a sample/hold (S/H) that freezes the low frequency signal for a period of time. This time must be enough to assure a simultaneous conversion by the 12 bit A/D converter. In baseband, the DSP performs the direction of arrival (DoA) estimation of the RF signals. The measurement setup is illustrated in Fig. 5.7.

The blocks S/H, Multiplexer and A/D are performed by the signal conditioning device SC-2040 and acquisition board PCI-MIO-16 E-1. Two 8-

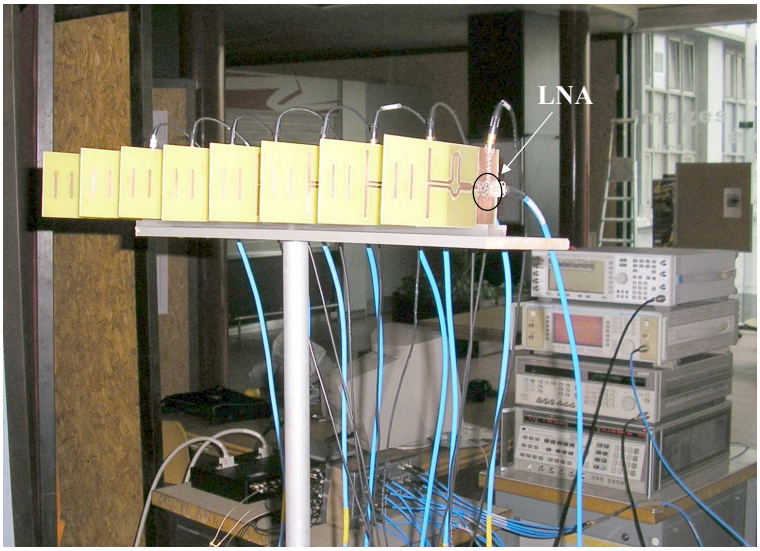

Figure 5.6: Receiving ULA composed of quasi-Yagi antennas and LNAs integrated on the antenna substrate.

Table 5.1: DoA estimates of 3 coherent sources using ULA array.

Theoretical DoAs	MUSIC estimates
-25°	-24°
16°	15°
57°	58°

channel SC-2040s are associated to each acquisition board with 16 single-end channels. Both devices are manufactured by National Instruments. The acquisition board is connected to a PC Pentium III via PCI bus.

Fig. 5.8 shows the estimation detection when coherent and incoherent sources are tested. Spatial Smoothing (SS) is applied when coherent sources are present. As there are 8 elements in the receiving array, the size of the subarrays is set at 5, as suggested in [86]. The number of snapshot $T = 100$. Tab. 5.1 presents the theoretical and estimated values of this experiment setup.

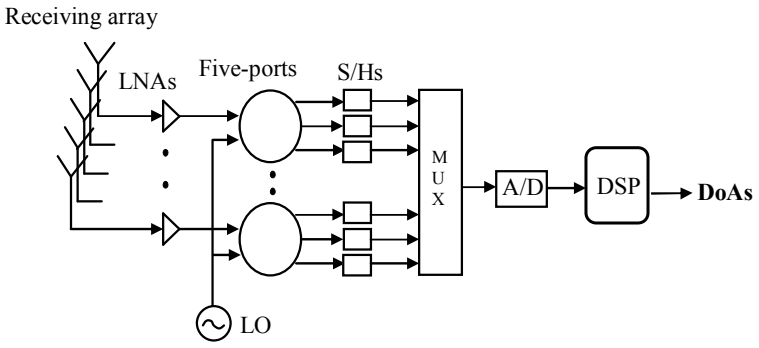

Figure 5.7: Measurement system of the direction of arrival of RF signals.

We have an accurate estimation with a maximum error of 1° when the decorrelating technique is applied before the MUSIC estimator. However, the MUSIC estimator fails to correctly compute its spectrum when the SS technique is not applied.

In order to measure the Doppler-shift of incident signals, a trial is performed with two antennas transmitting CW signals as illustrated in Fig. 5.9. One of the antennas is stationary, whereas the second moves in the radial direction of the antenna array. This displacement is performed manually. The operating frequency is 2.4 GHz; the sampling frequency is $f_s = 20$ Hz; and the number of samples is $N_s = 50$. N_s and f_s determine the Doppler resolution and Doppler window, respectively.

The relative azimuth angles and speed of the transmitting antennas in comparison to the receiver is as follows: For the first antenna $\theta_1 = 20°$ and $v_1 = 0$ m/s, and for the second antenna $\theta_2 \approx -17°$ and $v_2 \approx 1$ m/s. The approximated speed of the second antenna produces a Doppler-shift of 8 Hz. Fig. 5.10 compares the MUSIC estimates with the approximately calculated theoretical values.

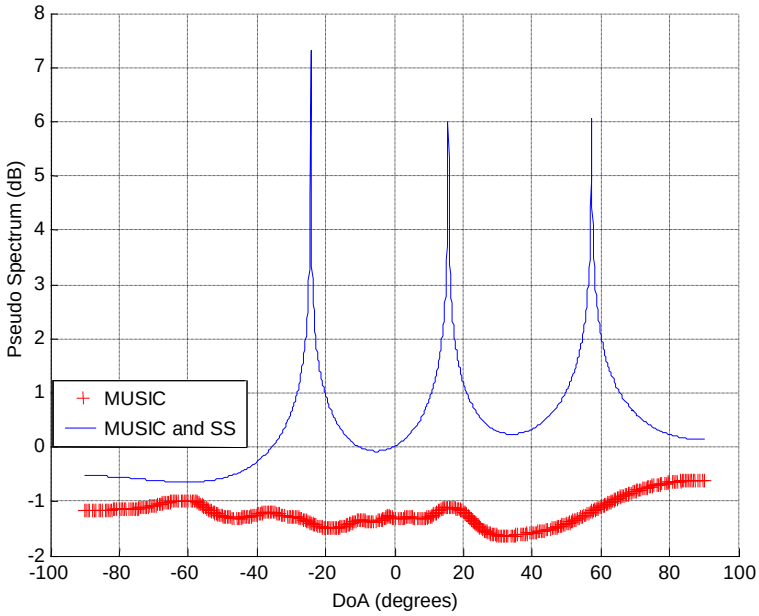

Figure 5.8: Experimental results - DoA estimation of three coherent sources using MUSIC and SS techniques. M=8, $sub_M = 5$, $f_c = 2.4$ GHz, $T = 100$

The estimated values are 22° and 0.5 Hz for the first source and -17°, and 10 Hz for the second source. Taking into consideration the imprecision in knowing the realistic value of v_2, this result is satisfactory for verifying system capability in measuring the Doppler-Shift.

5.3.3 DoA finding experiment using a uniform rectangular array (URA)

In this section, estimation results on the elevation and azimuth angle of RF signals are presented. Only CW signals are transmitted and the system operates at 2.4 GHz. The receiving array is made up of 14 antennas forming a 7×2 uniform rectangular array. The RF front end is the same as in Fig. 5.7 and the experiments are carried out in a non-reflective environment.

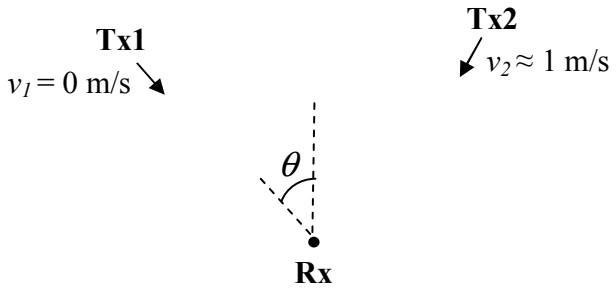

Figure 5.9: Scenario of a DoA and Doppler-shift simulation performed by directive antennas. The arrows correspond to the directive antennas and point to the receiving array.

Table 5.2: Azimuth and elevation angle estimation of 4 incoherent signals.

Theoretical values (Azimuth, Elevation)	MUSIC estimates (Azimuth, Elevation)
-18°, -4.5°	-15°, -5.5°
-53°, 21°	-50.5°, 21°
20.5°, -15°	22.5°, -13.5°
52°, 7°	51.5°, 13°

Two experimental trials are performed. In the first, 4 non-coherent signals with different DoAs are simulated by 4 directive transmitting antennas. Fig. 5.11 and Tab. 5.2 show the system performance in estimating the azimuth and elevation components of the DoAs using the MUSIC algorithm. The MUSIC pseudo-spectrum is plotted as a contour map, on which the peaks are indicated by the direction of the spectrum gradients. The marks ($\times$) correspond to the theoretical DoAs.

The DoA of all signals is well estimated by the five-port/MUSIC system with the exception of the elevation angle of the signal from the fourth transmitting antenna, which presents an error of 6°. A second trial is carried out. This time, three coherent signals are transmitted by directive antennas

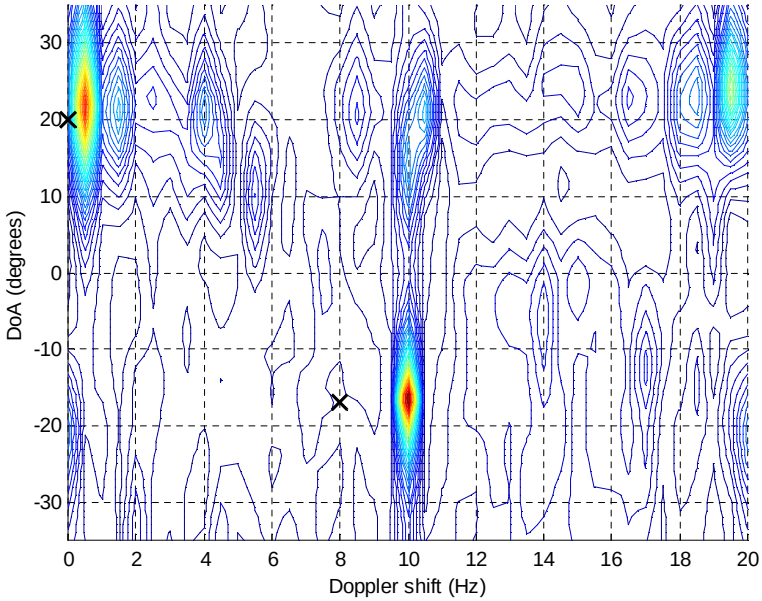

Figure 5.10: Estimation of azimuth DoA and Doppler-shift of two sources. $M = 8$, $N_s = 50$ samples, $f_s = 20$ Hz, $f_c = 2.4$ GHz. (Spectrum peaks) MUSIC estimates; (×) theoretical values.

and measured by the proposed system. The number of sources is estimated by MDL and its result is shown in Fig. 5.12. The algorithm uses the data covariance matrix after decorrelation by the SS procedure and the number of snapshots is $T = 100$. $sub_{M_y} \times sub_{M_z} = 8$ bars are displayed and $N = 3$ is estimated.

The MUSIC algorithm is used after the spatial smoothing of the data, as shown in Fig. 5.13. Table 5.3 displays both the theoretical and estimated values.

The estimation of the number of signals and the MUSIC estimates of DoA are coherent with the theoretical values. A maximum error of 4.5° is observed in the azimuth angle for signals from the second antenna.

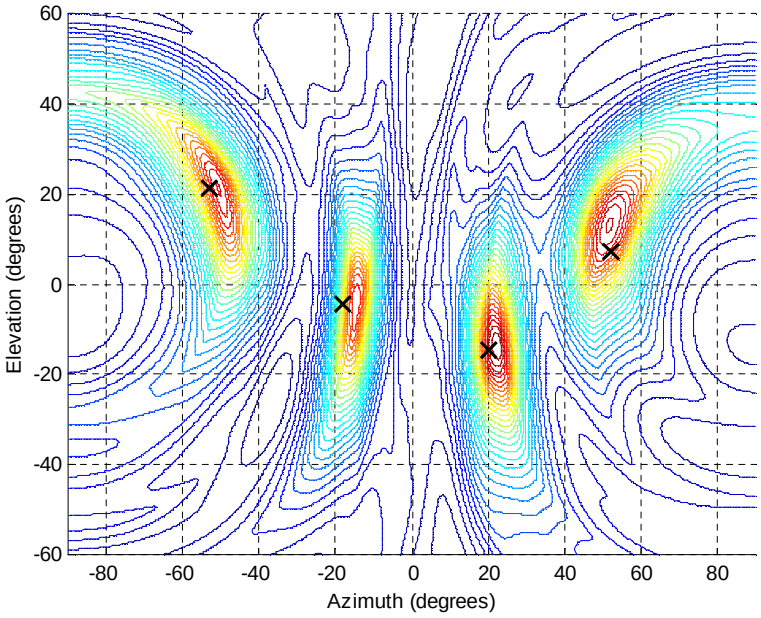

Figure 5.11: Estimation of azimuth and elevation angles of arrival of 4 incoherent sources. $M_y = 7$, $M_z = 2$, $f_c = 2.4$ GHz, $T = 100$ samples. (Spectrum peaks) MUSIC estimates; (×) theoretical DoAs.

5.4 Multitone channel sounder using Five-Port discriminator

The proposed channel sounder consists of quasi-Yagi elements arranged as a ULA or URA array, LNA and five-port discriminator that performs direct conversion. The measurement architecture is parallel SIMO and the system

Table 5.3: Azimuth and elevation angle estimation of 3 coherent signals.

Theoretical values (Azimuth, Elevation)	MUSIC estimates (Azimuth, Elevation)
-18°, -4.5°	-13.5°, -2°
-53°, 21°	-51°, 18°
20.5°, -15°	21.5°, -11°

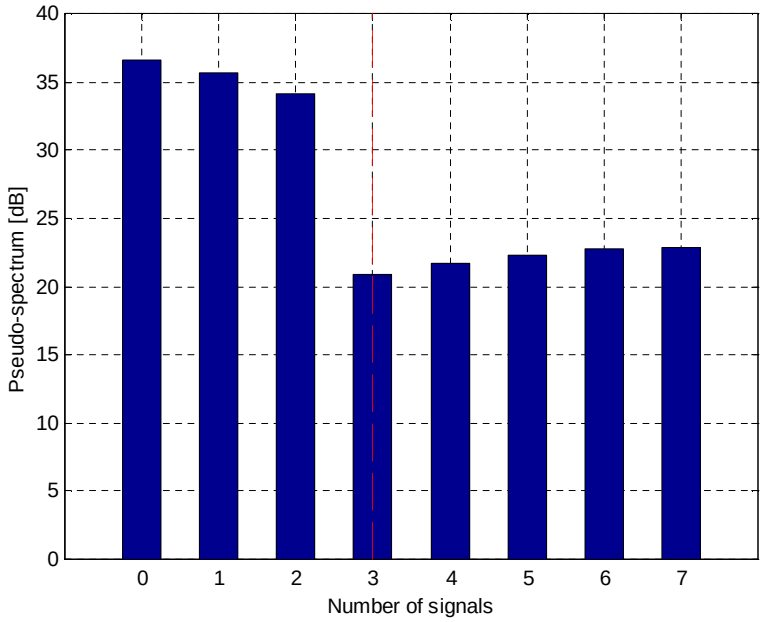

Figure 5.12: Number of source estimation using minimum description length (MDL) for a 7×2 URA. The theoretical and estimated number of sources is $N = 3$.

is appropriate for sounding indoor environments. The bandpass signals at the output of the five-ports are digitally converted before the estimation of the propagation channel parameters.

Fig. 5.14 presents the proposed channel sounder that operates from 2.3 GHz to 2.5 GHz with a frequency step of 2 MHz. Δf limits the measurable distance of paths. In the time delay domain, $\Delta f = 2$ MHz corresponds to an observation window of 500 ns.

It is also possible to perform a sounding with $B_w = 400$ MHz around 2.4 GHz at the expense of having a non-flat LNA gain over the entire band.

The computer controls the changing frequency of the generator via a GPIB bus and performs the acquisitions for each frequency and antenna.

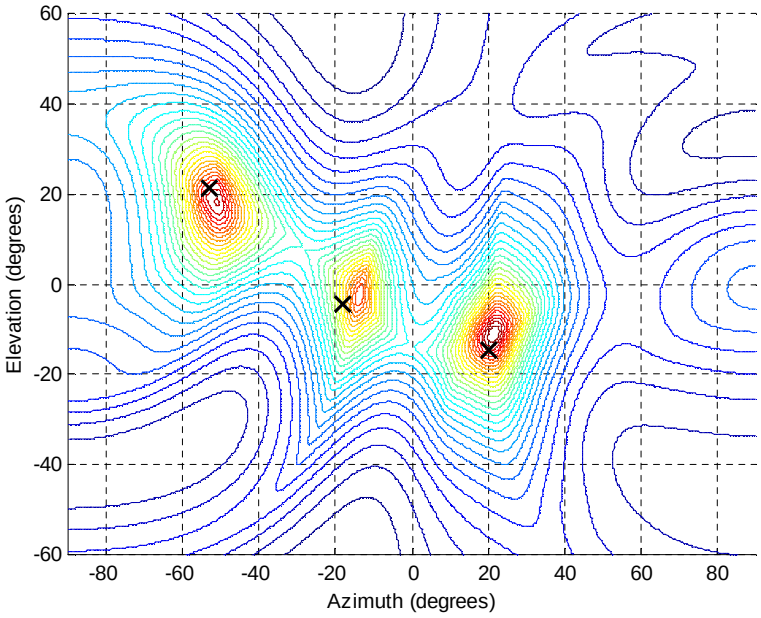

Figure 5.13: Estimation of azimuth and elevation angles of arrival of 3 coherent sources. $M_y = 7$, $M_z = 2$, $sub_{M_y} = 4$, $sub_{M_z} = 2$, $f_c = 2.4$ GHz, $T = 100$. (Spectrum peaks) MUSIC estimates; ($\times$) theoretical DoAs.

This procedure is usually slow and can be substituted by a faster process using an external clock (TTL 5 volts) for the frequency changing and acquisition.

A transmitting antenna connected to an RF generator emits multitone signals as a function of time. Each CW signal is filtered by the propagation channel before reaching the receiving array. The incident waves are then combined and amplified by the LNA. The signal from each antenna is down-converted by a five-port using the signal from the sweep generator as the LO signal. The outputs of the five-ports are connected to a SC-2040 device and then to the acquisition board (PCI-MIO 16E1), which contains one A/D. Six SC-2040 devices and three acquisition boards are used to convert 48 analogue

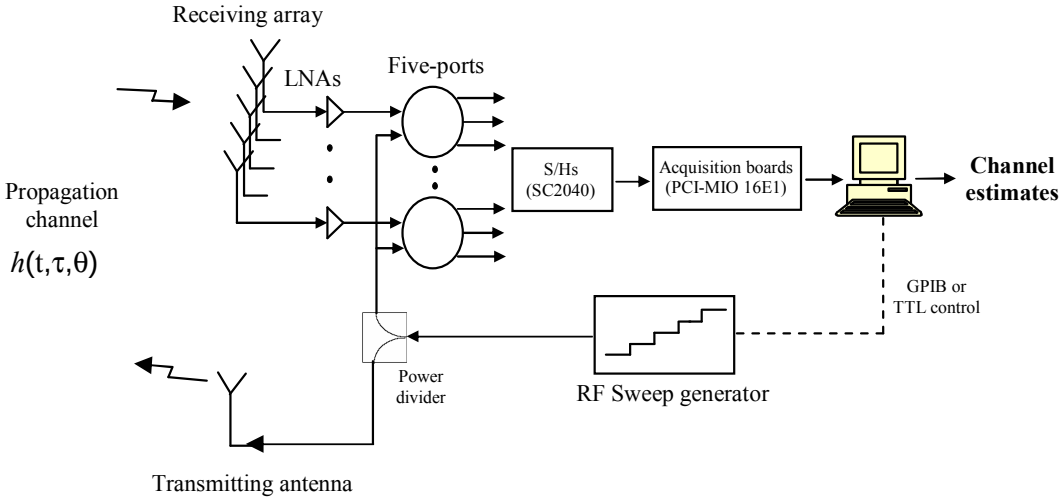

Figure 5.14: SIMO channel sounder using five-port discriminators.

signals when 16 array elements are used.

The channel response for each frequency and antenna is then computed as the complex envelope between Ports 1 and 2 of the five-port. The SISO transfer function is the assembling of these responses from one five-port and the SIMO transfer function from all five-ports.

5.4.1 Multipath simulation using cable

An experiment using cables for simulating multipath phenomena is carried out to test the measurement scheme. The implemented SISO system consists of cables of different lengths connected to the same generator representing coherent paths with different time delays. A combiner is used to associate all cables to the RF input of the five-port.

4 paths are simulated by cables of 2 m, 4 m, 6m and 7.5 m, corresponding to time delays of 9 ns, 18 ns, 27 ns and 33.5 ns. These values were measured

Table 5.4: Time delay estimation of 3 coherent paths simulated by cables.

Theoretical values	DFT estimates	MUSIC estimates	ESPRIT estimates
9 ns	10 ns	9 ns	8.6 ns
18 ns	20 ns	19.5 ns	19.3 ns
27 ns	27.5 ns	28 ns	27.9 ns
33.5 ns	35 ns	35 ns	35.1 ns

by a vector network analyzer. 401 frequency tones from 2.2 GHz to 2.6 GHz were used for sounding the simulated channel. Before employing the MUSIC and Unitary-Esprit estimators, the SS technique is applied with a subarray size of 251. The theoretical and estimated values using MUSIC, Esprit and DFT are presented in Tab. 5.4.

Good results are seen for all techniques even for the Fourier method. It is due to the wide bandwidth used in the sounding performing a resolution of $1/B_w$= 2.5 ns for DFT estimations.

The direction finding system presented in Section 5.3 and the simulated propagation channel presented above using cables and microstrip circuits validate the adequate performance of the measurement system and employed algorithms in ideal conditions.

5.4.2 Joint estimation of DoA and time delay of multipath

The sounding of a propagation channel using SISO measurements is limited to the time-delay characterisation. When paths with very close lengths are present, even high-resolution techniques of estimation cannot distinguish them.

Since the measure data depends on the phase-shift between frequency tones and array elements when a spatio-temporal sounding is performed, the mode vector of paths with different DoAs or time delays is not the same. Hence, joint estimation of DoA and time delay of the multipath using a SIMO architecture enables the discrimination of paths with the same length. Besides, the angular characterisation is very important for smart antennas applications.

In an experiment setup, a propagation channel is reproduced by coherent signals transmitted by four directive antennas in a non-reflective environment. The transmitter positions compared to the receiving antenna reproduce paths with different time delay, azimuth and elevation angles.

At the receiver, a URA of 16 elements (8×2) is used and the number of snapshots associated to each antenna and tone is $T = 48$. The spatio-temporal parameters for each path are geometrically calculated and correspond to the values in Tab. 5.5. The data measured by the five-port discriminators are smoothed using the 3D-SS technique. Thus, joint estimates of time delay, azimuth and elevation angles are computed by using the MUSIC and 3D Unitary-Esprit estimators. As the MUSIC spectrum of a 3D system (Y, Z and frequency domains) cannot be displayed, an algorithm is employed to search for peaks in the 4D spectrum (pseudo-spectrum, azimuth, elevation and time delay axes).

The radiation pattern of the quasi-Yagi antennas is used to remove the antenna influence on the propagation channel. After estimation of power using (2.18), the estimates are compensated according to a lookup table containing the antenna radiation pattern. We assume that the radiation

Table 5.5: Estimation of azimuth (θ_n) and elevation (ϕ_n) angles, relative time delay (τ_n) and normalized power (P_n) of 4 paths reproduced by directive antennas.

Theoretical values (τ_n, θ_n, ϕ_n, P_n)	MUSIC estimates (τ_n, θ_n, ϕ_n)	ESPRIT estimates (θ_n, ϕ_n)	Power estimates (P_n)
0 ns, 52°, 7.5°, 0 dB	0 ns, 56°, 11°	50°, 9.5°	-0.5 dB
5.3 ns, -52.5°, 21°, -0.3 dB	5 ns, -56°, 16°	-54.5°, 16°	0 dB
14.1 ns, -17°, -3°, -4.2 dB	15 ns, -18°, -10°	-20.5°, -6°	-5.8 dB
19.4 ns, 22.5°, -10.5°, -5.3 dB	20 ns, 22°, -13°	13°, -26.5°	-5.5 dB

patterns for all frequencies are similar. Thus, the radiation at 2.4 GHz is used for power compensation.

The theoretical values, MUSIC and Esprit estimates are presented in Tab. 5.5. Only three of the four paths are well estimated when the 3D Unitary-Esprit is used, whereas the MUSIC estimator performs a maximum error of 7° in elevation angle. Estimation in elevation angle is more subject to errors than time delay and azimuth estimates, as only two elements are presented in the Z-axis and the size of sub_{M_Z} is two. Fig. 5.15 illustrates the power delay profile (PDP) of the simulated propagation channel in agreement with the theoretical values.

5.4.3 Measurements of an indoor propagation channel

For over three years, a number of tools for estimating propagation parameters were implemented and tested. The complexity of the measurement system was gradually increased. Finally, a measurement campaign is carried out in order to test the reliability of the system in a realistic scenario.

The aim of this experimentation is not to achieve an objective charac-

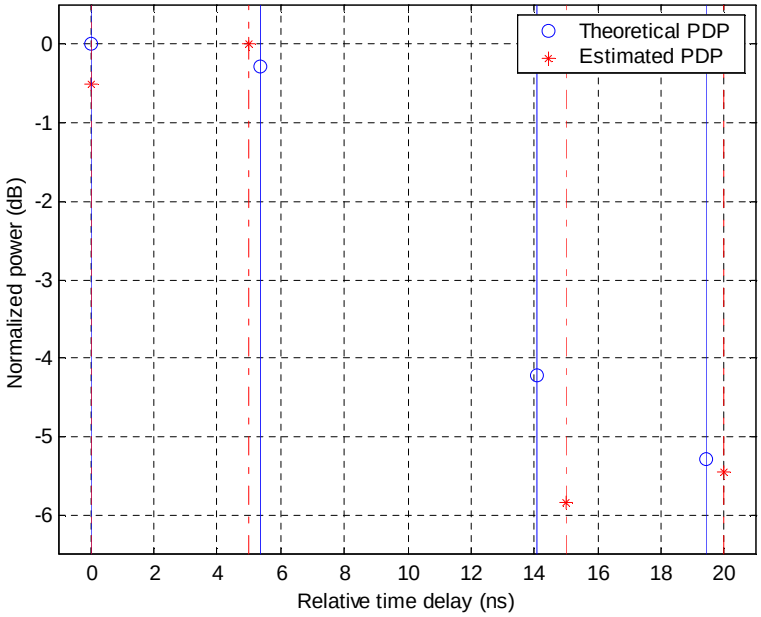

Figure 5.15: Power delay profile (PDP) of a propagation channel reproduced by directive antennas. Estimates are found using 3D SS and MUSIC estimator. $M_y = 8$, $M_z = 2$, $L = 101$, $sub_{M_y} = 4$, $sub_{M_z} = 2$, $sub_L = 61$, $f_c = 2.4$ GHz, $B_w = 200$ MHz, $T = 48$ samples. ($\circ$) Theoretical values. (*) Estimated values.

terization of a given environment. A sufficient number of measurements is not performed so as to attain neither the representative parameters of the frequency selectiveness nor parameters such as Doppler bandwidth and angular spread. The aim of this experimentation is to show the capability of the proposed system in estimating the DoA and time delay of a multipath in indoor environments.

The measurement campaign is performed in a corridor with metallic walls of Ecole Nationale Supérieure des Télécommunication (ENST) in Paris. For a fixed receiving antenna, two different locations for the transmitting antenna are tested reproducing different propagation channels. In the first case, there

is line of sight (LoS) between transmitting and receiving antennas. In the second case, there is no line of sight (NLoS). Both measurements are done with a stationary receiver and transmitter.

Fig. 5.16 illustrates the scenario for both trials. The antenna height of both transmitting and receiving antennas is 1.59 meters and a ULA of 8 elements is used. Thus, only the azimuthal component of angles is measurable. The antenna array is placed with the H-plane of the elements orthogonal to the corridor wall axis. Both transmitting and receiving antennas are linearly polarized on the vertical plane.

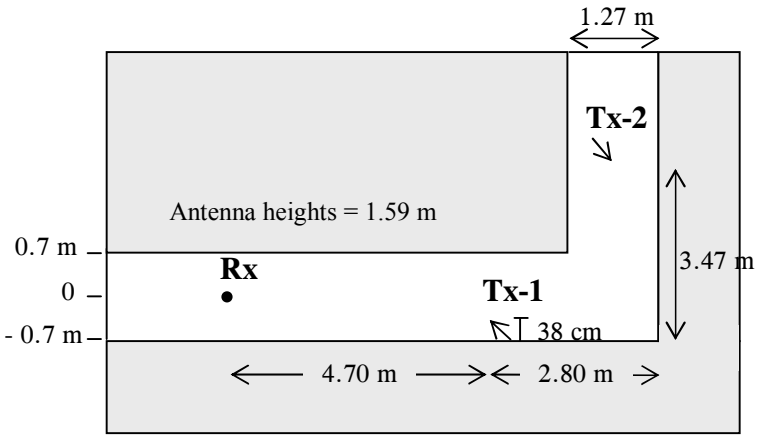

Figure 5.16: Floor plan of the measurement site.

Although unusual in channel soundings, a directive antenna is used as a transmitter. The directive antenna Tx-1 points to the opposite wall with 40° to the corridor wall axis in the first experiment. 400 MHz of band is swept from 2.2 GHz to 2.6 GHz by transmitting 201 frequency tones. Compensating for loss in the cables, the power at the input of the transmitting antenna is about 2 dBm and the power at the input of the local oscillator is -3 dBm.

Table 5.6: LoS case - Joint estimation of time delay and azimuth angles of multipath.

MUSIC estimates
44 ns, -8°
48 ns, -37°
52 ns, 46°
54 ns, -51°
59 ns, 66°

The joint estimation of time delay and azimuth angle of multipath for the LoS case using 2D SS and MUSIC is presented in Tab. 5.6.

44 ns of time delay are observed for the first path. In fact, the real time delay between receiving and transmitting antennas is 15.7 ns, as the corresponding distance is 4.7 meters. However, the calibrating measurements were performed with the transmitter 3.5 meters from the receiving array. Thus, the difference between these distances is 1.2 meters (or 4.3 ns). A 10-meter cable ($\varepsilon_r = 1.45$) is added to help the displacement of the transmitter, inserting an offset of 40 ns in the time delay.

Since the scenario of the first experiment is simple, the propagation channel can be modelled as a wave guide for calculating the path parameters, as seen in [145]. The DoA of waves which experienced, respectively, an even and odd number of reflections is found using:

$$\theta^{\pm}_{even} = \arctan\left(\frac{C_w N_R \mp d_r \pm d_t}{C_d}\right) \tag{5.1}$$

$$\theta^{\pm}_{odd} = \arctan\left(\frac{C_w (N_R \pm 1) \mp d_r \mp d_t}{C_d}\right)$$

θ^{+} denotes DoA > 0 and θ^{-} denotes DoA < 0. N_R is the number of

reflections experienced by the wave and d_r, d_t, C_w and C_d are geometrical variables shown in Fig. 5.17. As c is the speed of light, the time delay is easily found using:

$$\tau = \frac{C_d}{\cos(\theta)\ c} \tag{5.2}$$

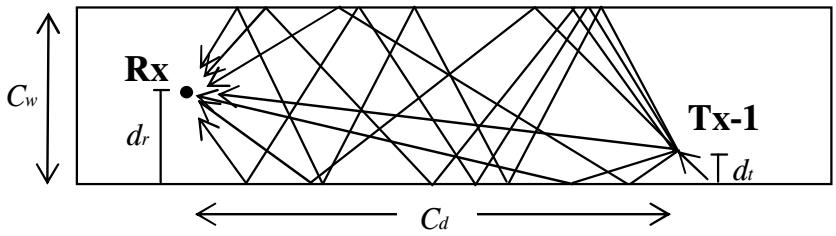

Figure 5.17: Floor plan of the measurement site of the first experiment.

Estimated and calculated values are compared in Fig. 5.18. All possible paths that experience up to 5 reflections are displayed according to (5.1) and (5.2). Only the zone where dominant paths are found is plotted.

Adequate agreement between theoretical and estimated values is observed with paths that experienced up to 5 reflections. Pairs of paths with very close time delays and DoAs are seen in the calculated values. In the MUSIC spectrum, each pair is seen as one peak because system resolution is exceeded. This effect of very close paths is due to the small distance between the transmitter and the corridor wall. That is, paths of 2 and 3 reflections with DoA > 0 are closer to one another when the transmitter is near the corridor wall. Nevertheless, dominant paths probably correspond to waves that are first reflected upon the wall on the right side of the transmitter due to the antenna directivity.

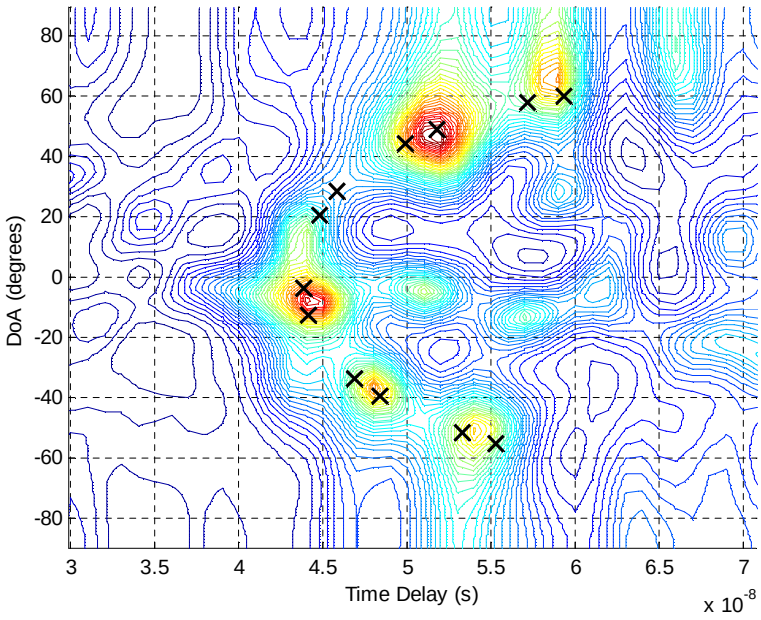

Figure 5.18: LoS case - Joint estimation of time delay and azimuth angle of propagation channel multipath using 2D SS and MUSIC estimator. $M = 8$, $L = 201$, $sub_M = 5$, $sub_L = 101$, $f_c = 2.4$ GHz, $B_w = 400$ MHz, $T = 100$ samples.

Estimation of paths with such a number of reflections is due to the wall material. The high conductivity of metallic surfaces ensures low attenuation per reflection. None of the paths that undergo reflections on the floor or ceiling is identified. There are two small peaks at (51 ns, -4°) and (57 ns, -13°), but no conclusive relation can be determined with these paths.

The second experiment is carried out. The channel sounder features remain the same and the measurement scenario is as in Fig. 5.16. The estimation of time delay, azimuth angle and normalized power is given in Tab. 5.7.

After compensating for the time delay due to the added cable and the time delay due to the position of the calibration reference as reported above,

Table 5.7: NLoS case - Joint estimation of time delay, azimuth angles and normalized power of the multipath.

MUSIC estimates
66 ns, -39°, -10.9 dB
68 ns, 28°, -21.4 dB
71 ns, -39°, -10.6 dB
75 ns, 53°, -16.8 dB
76 ns, -19°, 0 dB
77 ns, 17°, -16.6 dB
82 ns, 45°, -18.7 dB
83 ns, -15°, -6.5 dB

the first path is estimated with 37.5 ns or 11.3 meters. This result is coherent with the scenario geometry. The MUSIC spectrum is shown in Fig. 5.19. At the top of the figure, the PDP estimated by the discrete Fourier transform and Hamming window is shown for comparing both spectrums.

We observe a cluster of waves with a delay window of 15 ns that concentrates most of the energy. This is a natural result of non-line-of-sight measurements. The dynamic range, which is measured from the highest peak of the cluster down to the noise level, is about 14 dB when DFT is used to estimate PDP.

In spite of the poor resolution of the DFT spectrum, it appears to be an important tool for comparing the MUSIC spectrum to the power distribution. Contrarily, the power estimates shown in Tab. 5.7 (see Section 2.3) give the impression of incoherence regarding the corresponding time delays and the strength of peaks in the MUSIC spectrum.

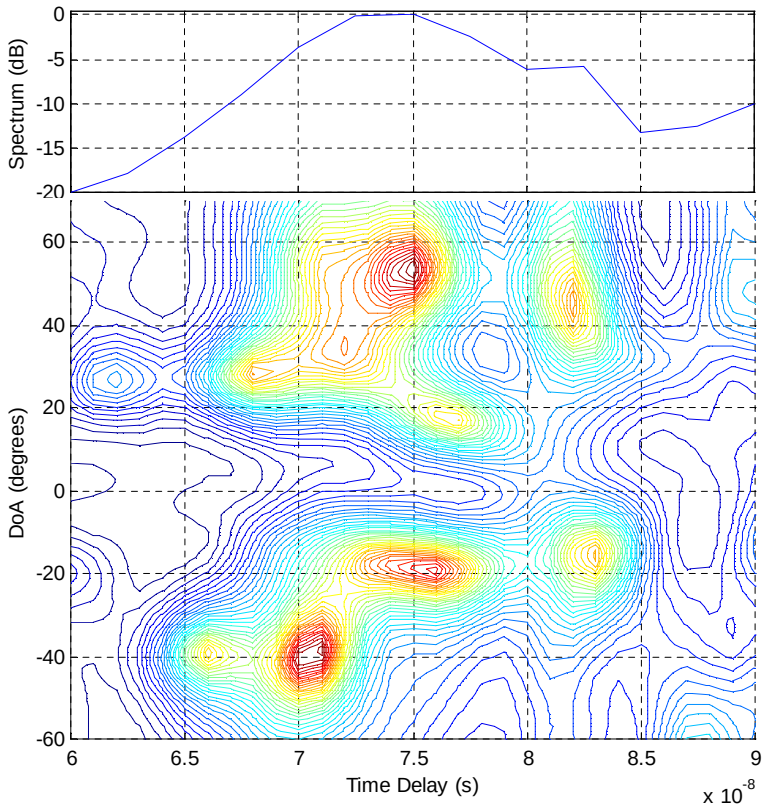

Figure 5.19: NLoS case - Curve at the top: Normalized DFT power spectrum calculated from one antenna data. Curve at the bottom: Joint estimation of time delay and azimuth angle of propagation channel multipath using 2D SS and MUSIC estimator. $M = 8$, $L = 201$, $sub_M = 5$, $sub_L = 101$, $f_c = 2.4$ GHz, $B_w = 400$ MHz, $T = 100$ samples.

5.5 Conclusion

A direction finding system and a SIMO channel sounder are proposed. The sounder is presented with different configurations for the antenna array and is made up of quasi-Yagi elements, LNAs, five-port discriminators and a narrowband acquisition system. The antennas employed are first presented, followed by the description of the multichannel measurement system, which includes the calibration procedure. Calibration is performed to correct the

imperfections of the five-port circuit as well as to compensate for the amplitude and phase of cables and circuits. This calibration procedure is very important, especially for antenna array processing.

In order to test the performance of the five-port circuit as phase discriminator, the propagation channel and antennas are reproduced by cables, phase-shifters and combiners for estimating the DoA and time delay of RF signals. The accurate results confirm the reliability of the circuit in ideal scenarios. A direction finding system is then implemented to test 1D and 2D measurement structures in environments of known geometry. The MUSIC estimator appears sensitive to errors caused by the correlation between incident signals. Thus, measured data has to undergo a decorrelation procedure before using MUSIC in such a case.

A channel sounding system is also tested when a propagation channel is reproduced by directive antennas. Each antenna corresponds to a path and the site of measurements is arranged to avoid parasite multipath signals. The power delay profile is measured in such a case with adequate agreement with the geometry of the transmitters and receiving antenna. The estimates of time delay, azimuth and elevation angles are found jointly by using a 3D process (MUSIC) of high computational cost. This is the main drawback of spectral estimators when the dimension of the spectrum to be computed is high.

The Doppler-shift of a CW signal is measured by the MUSIC/five-port system. Nevertheless, Doppler-shift characterization could not be performed in this work due to the limitation of available generators.

A measurement campaign in a corridor of a building is carried out to

test the SIMO channel sounder in a more realistic condition. Two trials are performed: the first is with line-of-sight between transmitting and receiving antennas and the second is in a non-line-of-sight condition. Both experiments presented coherent estimates of the channel parameters. However, the power estimation technique [7] seems less appropriate for channel sounding applications in a more realistic condition.

The dynamic range of 15 dB observed in Fig. 5.19 is not conclusive, since the power supplied to the transmitter is less than 2 dBm. A number of experiments in different scenarios and with higher power levels for the transmitter should be carried out to measure the dynamic range of the system.

The 2D and 3D versions of spatial smoothing appear to be efficient techniques for recovering the correlation matrix rank, especially the modified 2D-SS proposed in [93]. The association of SS techniques with the MUSIC estimator in this work demonstrates the robustness of these methods in resolving multipath with good resolution, as seen in Fig. 5.19. This is possible because a joint estimation of both DoA and time delay components is performed. The feasibility of estimating a number of paths comparable to the number of array elements is confirmed.

Summary, conclusions and recommendations

The aim of the work reported in this thesis is to contribute toward the development of tools for channel sounding and digital beamforming communication systems. A number of algorithms and circuits known in the literature are assembled to compose the proposed systems, particularly, the five-port discriminator used as a measurement circuit of RF signals. The redundant RF path is a useful means for fighting the unbalance between the circuit outputs when compared to IQ demodulators.

The first part of the study (Chapter 1) consists of a bibliographic research on the physical mechanisms and phenomena found in propagation channels and the best-known propagation models. The need for small-scale characterization of the propagation channel is evident for wideband systems. Channel sounding is therefore essential to the accomplishment of this characterization.

State-of-the-art of main channel sounding techniques is presented, describing their advantages and drawbacks. Among these techniques, the frequency domain multitone technique is chosen as a suitable technique due to its low implementation complexity, the cost of acquisition cards and low

mobility of indoor propagation channels. The proposed channel sounder is then described and its features and performances compared (Appendix A) to the best-known sounders in the literature. The time/angle resolution of the ENST channel sounder determines its main benefit in comparison to most techniques.

Chapter 2 presents a set of algorithms for estimating the azimuth and elevation components of the direction of arrival (DoA), time delay and signal strength for coherent and incoherent signals. The data model is first described for a direction finding system and then extended to the estimation of a channel impulse response (CIR). The model is also extended to the joint estimation of these parameters, including the azimuth component of DoA.

Algorithms used to resolve different stages of the estimation procedure are depicted. Minimum Description Length (MDL) and the algorithm described in [7] are used to estimate the number of sources and power of RF signals. The high resolution estimators MUSIC and unitary-Esprit and their 2D and 3D versions are depicted.

The performances of MUSIC, Esprit and Fourier transform are then compared, as reported in the literature and by means of simulation trials. We conclude that high resolution techniques have better performance than classical Fourier methods, and comparing the Esprit and MUSIC estimators, the former is less sensitive to modeling errors of the steering vector, whereas Esprit has a low computational cost even for systems with an increased number of dimensions.

Both the MUSIC and Esprit algorithms are sensitive to the rank-deficiency of covariance matrices caused by the linear dependence between sources. Spa-

tial Smoothing is then employed for fighting this rank-deficiency before using the MUSIC and Esprit estimators. An extension of this technique for a system of N dimensions is proposed and an adequate performance is found by means of simulation trials.

The third part (Chapter 3) is dedicated to the description, design and use of five-port discriminators implemented in microstrip technology for operating around 2.4 GHz. The five-port is a passive, linear circuit that performs a direct conversion of RF signals and is made up of a five-arm ring and three Schottky diode power detectors. Simulated results show that the five-port inputs are well matched and the isolation between them is only 6 dB.

The power detector is depicted, along with the fitting procedure used for correcting the non-quadratic behaviour of the Schottky diode for high-input power. A resistive circuit is used for matching the power detector input, which results in widening the five-port passband at the expense of increasing the system noise factor. The chapter is concluded with the calibration procedure of the five-port system aimed at correcting the circuit default and compensating for the local oscillator unbalance for each operating frequency.

Chapter 4 presents the proposed digital beamforming system using five-port discriminators aimed at maximising the useful signal strength at the system output as well as attenuating strong interference. An abstract of the best-known beamforming techniques is first presented. Among them, the one-stage schemes LCMV and unconstrained beamformer are studied, as they are less complicated and less computationally heavy in comparison to the other techniques described in Section 4.1.

The Taylor tapering is used as an option for reducing interference by

controlling the sidelobe level and beamwidth of radiation patterns. The BER curves shown at the end of the chapter demonstrate the ability of the system in filtering incident signals in the angle domain and, consequently, providing higher gain (and smaller BER) in the look direction, even with presence of a strong interference level. The minimum detectable signal of -88 dBm obtained in the last experiment for a BER of 10^{-3} and using only 5 array elements proves the adequate sensitivity of the system compared to monochannel five-port systems.

In the last part of this study (Chapter 5), the measurement setup and results of a direction finding system and the ENST channel sounder are presented. The quasi-Yagi antenna and a description of the multichannel measurement system, including the calibration procedure, are presented first. The quasi-Yagi antenna is known to be suitable for array applications, as the mutual-coupling between consecutive elements is considered low. The same algorithm used in Chapter 3 for correcting five-port defaults also compensates the variation of phase and amplitude of signals between cables. This calibration procedure sets a spatial-time reference for the channel sounding and is carried out using QPSK modulated signals transmitted by a reference antenna away from the receiver in far-field condition.

The direction finding system is first tested by means of simulation with cables and RF circuits. The accurate results prove the capacity of the system in measuring the phase-shift between five-ports in "quasi-ideal" conditions. The system is then tested to measure the DoA of directive antennas using MUSIC and 2D-Spatial Smoothing. 7×2 elements are used in the antenna array and the operating frequency is 2.4 GHz. Adequate results are found in

the estimation of 3 coherent and 4 incoherent sources. The biased estimates are mainly due to the small antenna aperture in the vertical axis and to the size of the subarray in the vertical axis, which is identical to the number of elements in this axis, that is $M_Z = sub_{M_Z} = 2$.

For testing SISO and SIMO channel sounders, simulations using cables and directive antennas are carried out. The number of sources is accurately estimated by the MDL algorithm for all trials. However, the Music spectrum estimation appears to be independent on the knowledge of the number of sources for systems with a large number of frequency tones. In such cases, the noise subspace is too large compared to the number of dominant signals and the choice of the noise subspace size is then less important compared to systems with small structures.

Satisfactory results are found for the joint estimation of time delay, azimuth and elevation angles of arrival of the reproduced paths by directive antennas. In this experiment, a URA of 16 elements (8×2) is used and 101 frequency tones sweeping 200 MHz around 2.4 GHz are transmitted. The maximum error is 7° in elevation angle and 1 ns in time delay domain when the MUSIC estimator is used in association with 3D Spatial Smoothing. From the same trial, the power delay profile of this simulated channel is shown with adequate results. Estimation in the time delay domain is always more accurate than angle estimates, as the number of frequency tones is much larger than the number of antennas.

Comparing unitary-Esprit and MUSIC estimates, the former is less biased for three paths, but could not resolve all paths, whereas the latter could. This proves that MUSIC is more robust than Esprit when system complexity

increases and is coherent with the observations reported in Section 2.2.3.

After testing the measurement and estimating tools for channel sounding. Two experiments are carried out in a realistic indoor propagation channel. The first is performed in a LoS condition and the second in an NLoS condition. 400 MHz of band around 2.4 GHz is swept by transmitting 201 tones and 8 elements are used in the uniform linear array. The results of both trials prove the adequate resolution of the system due to the joint estimation of both DoA and time delay components. The feasibility of estimating a number of paths comparable to the number of array elements is also confirmed.

Recommendations

Further works should be directed toward carrying out measurement campaigns in different scenarios in order to enlarge the collected statistical data. Consequently, stochastic models can be tuned to simulate mobile radio channels. Similarly, the performance of channel simulations using deterministic models, such as ray-tracing, can be verified through a comparison to channel soundings.

The present work is limited to stationary measurements, since the PLL of available sweep generators takes a long time to change from the highest frequency to the lowest frequency. This problem can be overcome by performing an alternately progressive and regressive sweep. This soft changing of frequency may allow the measurement of a sufficient number of frequency-sweeps over a period of time for detecting Doppler-shift. Nevertheless, for characterizing outdoor propagation channels where the coherence time is usually smaller, other sounding techniques must be considered, such as the

sliding correlation technique.

The extension to H-polarisation measurements is of interest, as incident signals with horizontal polarisation can be taken into consideration for the power distributions.

The LNA integrated on the array antennas may be replaced by a more adapted amplifier to the present system. The wide bandwidth of the antennas can be more advantageous associated to LNAs of a wider bandwidth. Furthermore, its 20 dB of gain is not enough to mask the five-port noise figure. Amplifiers of higher gain can improve the system sensitivity at the expense of increasing its cost. Concerning the estimation procedure, a number of tests in realistic propagation channels is needed to validate the employed power estimation technique.

The beamforming system may be extended to a 2D spatial filter and must be tested for signals with a more realistic bandwidth. For such, the narrowband acquisition system must be replaced by faster acquisition boards.

Channel characterization that takes into consideration the angular distribution of the multipath in the receiving antennas, as well as in the transmitting antennas, is a recent topic of research. The absence of exhaustive measurements and characterization of MIMO propagation channels indicates the need for upgrading the complexity of the preset system to MIMO channel sounders. This is in process and corresponds to the thesis study of another student at *Ecole Nationale Supérieure des Télécommunications*.

Appendix A

Features of some channel sounders

In Table A.1, a number of channel sounders are described according to the type of channel architecture, sounding technique, carrier frequency, bandwidth, sampling frequency, signal processing technique, dynamic range, system resolution and whether joint spatio-temporal estimation is achieved. UWB channel sounders are not included in the list.

With respect to SIMO schemes, the channel sounder architecture is parallel when system outputs are measured at the same time. Architecture is serial when only one measurement circuit is used to measure all output channels by means of a switch. Regarding the transmitter, the same reasoning is made for multiple input multiple output (MIMO) systems.

The evaluation of the system resolution when joint estimates are performed, such as in the ENST channel sounder, is difficult, as paths may be found with the same time delay or direction of arrival. In Tab. 5.7, the

fifth and eighth paths are separated of 7 ns and 4°, and the first and second paths are separated of 2 ns and 67°. This does not determines the system resolution, but exemplifies the resolution performance.

A number of experiments in different scenarios and with higher power levels for the transmitter should be carried out to measure the dynamic range of the ENST channel sounder.

Table A.1: Features of some channel sounders

	Architecture	*Technique*	*Carrier Frequency*	*Bandwidth*	*Sampling frequency*	*Signal processing technique*	*Joint estimation*	*Dynamic range*	*Resolution*
ENST	parallel SIMO	Multitones	2.4GHz	200MHz/ 400MHz	10Ksps	MUSIC and SS	Yes	-	2-5ns and 5°
RUSK	MIMO with switch	Frequency domain correlation processing	5-6GHz (Hyperlan)	120MHz	320Msps	2D Unitary-ESPRIT and SS	Yes	up to 80dB	1.5ns and 5°
AMERICC	SIMO with switch	Frequency domain correlation processing	2-60GHz	250MHz	1Gsps	Wiener inversion	-	$>$ 40dB	4ns
UMIST	parallel MIMO	CHIRP	1.9 and 2.1GHz (UMTS)	60MHz	1-2.5Msps per channel	SAGE	Yes	40dB	20ns
HUT	SIMO with switch	Direct correlation	2.154GHz	30MHz	2 boards of 120Msps	Beamforming/ Direct correlation	Yes	12dB (spatial)	33ns and 40°
INSA SC	SISO	Sliding correlation	2.45GHz	-	-	Sliding correlation	-	60dB	12ns
INSA SS	MIMO with switch	Spread spectrum	2-4GHz	up to 100MHz	2Gsps	Unitary-ESPRIT/ Spread spectrum	No	up to 60dB	10ns
Virginia	SISO	Direct impulse measurement + SSTDP	27.925GHz	850MHz	1Msps	No need	-	$<$ 78dB	2.35ns

Bibliography

[1] F. R. Souza, B. A. Garcia, G. Neveux, and B. Huyart. Five-port junction: In the way of general public application. In *32nd European Conference on Wireless Technology*, pages 1081–1084, Milan, Italy, Sep. 2002.

[2] J. D. Parsons. *The mobile radio propagation channel.* John Wiley & Sons Ltd, Chichester, U.K., second edition, 2000.

[3] Agilent technologies. *Surface mount zero-bias Schottky detector diodes.* Diode Schottky HSMS2850 - Data Sheet.

[4] F. R. de Sousa. *Application du corrélateur « Five-Port » aux PLLs, à la récupération de porteuse et à un MODEM de télécommunications dans la bande 1,8 - 5,5 GHz.* PhD thesis, Ecole Nationale Supérieure des Télécommunications, Paris, France, 2004.

[5] Agilent technologies. *Schottky Barrier diode video detectors.* Application Note 923.

[6] G. Bienvenu and L. Kopp. Optimality of high resolution array processing using the eigensystem approach. *IEEE Transactions on Acoustics, Speech, and Signal Processing*, 31(5):1235–1248, Oct. 1983.

[7] R. Schmidt. Multiple emitter location and signal parameter estimation. *IEEE Transactions on Antennas and Propagation*, 34(3):276–280, Mar. 1986.

[8] J. Rissanen. Modeling by the shortest data description. *Automatica*, 14:465–471, 1978.

[9] J. Huang and J. Chen. Statistical performance comparison of high-resolution doa estimation methods. In *3rd International Conference on Signal Processing*, volume 1, pages 505–508, Oct. 1996.

[10] T. J. Shan, M. Wax, and T. Kailath. On spatial smoothing for directional of arrival estimation of coherent signals. *IEEE Trans. on Acoust., Speech, Signal Processing*, ASSP-33:806–811, 1985.

[11] S. U. Pillai and B. H. Kwon. Forward/backward spatial smoothing techniques for coherent signal identification. *IEEE Trans. on Acoust., Speech, Signal Processing*, 37:8–15, 1989.

[12] S. Applebaum and D. Chapman. Adaptive arrays with main beam constraints. *IEEE Trans. on Antennas and Propagation*, 24(5):650–662, Sep. 1976.

[13] R. J. Mailloux. *Phased array antenna handbook*. Artech House, Norwood, MA, 1994.

[14] S. Pittet, J. Ekholm, T. J. Hart, N. Ingelbrecht, E. Liew, and Nahoko Mitsuyama. *Forecast: Mobile Services, Worldwide, 2001-2010*. Gartner, 56 Top Gallant Road, Stamford, CT 06902-7700, U.S.A., July 2006.

[15] Lucien Boithias. *Propagation des ondes radioélectriques dans l'environnement terrestre*. Dunod, Paris, France, second edition, 1984.

[16] Alain Glavieux and Michel Joindot. *Communications numériques: Introduction*. Masson, Paris, France, 1996.

[17] John G. Proaki. *Digital communications*. McGraw-Hill, New York, NY, third edition, 1995.

[18] Sylvie Marcos. *Les méthodes à haute résolution : Traitement d'antenne et analyse spectrale*. Hermès, Paris, France, 1998.

[19] P. A. Bello. Characterisation of randomly time-variant linear channels. *IEEE Trans. on Communication Systems*, CS-11:360–393, Dec. 1963.

[20] Theodore S. Rappaport. *Wireless communications: Principles and practice*. Prentice Hall, Upper Saddle River, NJ, second edition, 2002.

[21] L. C. Godara. Application of antenna arrays to mobile communications, part ii: Beam-forming and direction-of-arrival considerations. *Proceedings of the IEEE*, 85(8):1195–1245, Aug. 1997.

[22] B. H. Fleury and P. E. Leuthold. Radiowave propagation in mobile communications: An overview of european research. *IEEE Communications Magazine*, 34(2):70–81, Feb. 1996.

[23] Constantine A. Balanis. *Antenna theory: Analysis and design.* Wiley-Interscience, Hoboken, NJ, third edition, 2005.

[24] J. Laurila. *Semi-blind detection of co-channel signals in mobile communications.* PhD thesis, The Finnish Academies of Technology, Helsinki, Finland, 2000. pp. 166.

[25] H. Hashemi. The indoor radio propagation channel. *Proceedings of the IEEE*, 81(7):943–968, July 1993.

[26] J. B. Andersen, T. S. Rappaport, and S. Yoshida. Propagation measurements and models for wireless communications channels. *Communications Magazine of IEEE*, 33(1):42–49, Jan. 1995.

[27] H. L. Bertoni. *Radio propagation for modern wireless systems.* Prentice Hall, Upper Saddle River, NJ, 2000.

[28] S.-C. Kim, B.J. Guarino, T. M. Willis III Jr., V. Erceg, S. J. Fortune, R. A. Valenzuela, L. W. Thomas, J. Ling, and J. D. Moore. Radio propagation measurements and prediction using three-dimensional ray tracing in urban environments at 908 mhz and 1.9 ghz. *IEEE Transactions on Vehicular Technology*, 48(3):931–946, May 1999.

[29] M. Hata. Empirical formulae for propagation loss in land mobile radio sercvices. *IEEE Transactions on Vehicular Technology*, 29:317–325, 1980.

[30] J. Fuhl, A. F. Molisch, and E. Bonek. A unified channel model for mobile radio systems with smart antennas. *IEEE Proceedings on Radar,*

Sonar and Navigation: Special Issue on Antenna Array Processing Techniques, 145(1):32–41, Feb. 1998.

[31] A. Saleh and R. Valenzuela. A statistical model for indoor multipath propagation. *IEEE Journal on Selected Areas in Communications*, 5(2):128–137, Feb. 1987.

[32] T. Zwick, C. Fischer, and W. Wiesbeck. A stochastic multipath channel model including path directions for indoor environments. *IEEE Journal on Selected Areas in Communications*, 20(6):1178–1192, Aug. 2002.

[33] M. Failli (ed.). Digital land mobile communications. Technical report, COST 207, 1989. Final Report.

[34] V. Perez (ed.). Final propagation model. Technical Report R2020/TDE/PS/DS/P/040/al, RACE UMTS Code Division Testbed (CODIT), June 1994.

[35] R. Gollreiter (ed.). Channel models. Technical Report R2084/ESG/CC3/DS/P/029/bl, RACE Advanced TDMA Mobile Access (ATDMA), May 1994.

[36] W. Braun and U. Dersch. A physical mobile radio channel model. *IEEE Transactions on Vehicular Technology*, 40(2):472–482, May 1991.

[37] R. B. Ertel, P. Gardieri, K. Sowerby, T.S. Rappaport, and J.H. Reed. Overview of spatial channel models for antenna array communication systems. *IEEE Personal Communications*, 5(1):10–22, Feb. 1998.

[38] G. L. Turin et al. A statistical model of urban multipath propagation. *IEEE Trans. on Vehicular Technology*, VT-21:1–9, Feb. 1972.

[39] T. Quiniou. *Conception et realisation de sondeurs spatio-temporels du canal à 1800 MHz. Mesures de propagation à intérieur et à l'extérieur des bâtiments.* PhD thesis, University of Rennes, Rennes, France, 2001.

[40] B J Lipa, B B Nyden, H Seim, and L Stearns. Anomalous seasonde current vectors due to low signal-to-noise ratios. In *2006 Ocean Sciences Meeting*, pages 20–24, Honolulu, HI, Feb. 2006.

[41] J. Guillet. *Caractérisation et modélisation spatio-temporelles du canal de propagation radioélectrique dans le contexte MIMO.* PhD thesis, INSA Rennes, Rennes, France, 2004.

[42] T. S. Rappaport, K. Blankenship, and H. Xu. Mobile and portable radio research group - bradley department of electrical and computer engineering, propagation and radio system design issues in mobile radio systems for the glomo project. Technical report, Virginia Polytechnic Institute and State University, Blacksburg, VA, Jan. 1997.

[43] W.R. Young Jr. and L.Y. Lacy. Echoes in transmission at 450 megacycles from land-to-car radio units. *Proc. IRE*, 38:255–258, Mar. 1950.

[44] C. J. Rieser. Design and implementation of a sampling swept time delay short pulse (sstdsp) wireless channel sounder for lmds. Master's thesis, Virginia Polytechnic Institute and State University, Blacksburg, VA, 2001.

[45] T. Zwick, T. J. Beukema, and H. Nam. Wideband channel sounder with measurements and model for the 60 ghz indoor radio channel. *IEEE Trans. on Vehicular Technology*, 54(4):1266–1277, July 2005.

[46] S. A. Charles, E. A. Ball, T. H. Whittaker, and J. K. Pollard. Channel sounder for 5.5 ghz wireless channels. *Communications, IEE Proceedings*, 150(4):253–258, Aug. 2003.

[47] K. Kalliola, H. Laitinen, P. Vainikainen, M. Toeltsch, J. Laurila, and E. Bonek. 3-d double-directional radio channel characterization for urban macrocellular applications. *IEEE Trans. on Antennas and Propagation*, 51(11):3122–3133, Nov. 2003.

[48] D. C. Cox. Delay doppler characteristics of multipath propagation at 910 mhz in suburban mobile radio environment. *IEEE Trans. on Antennas and Propagation*, 20:625–635, Sep. 1972.

[49] T. Takeuchi and H. Mukai. Ultra wide band channel sounding for indoor wireless propagation environments. In *IEEE Topical Conference on Wireless Communication Technology 2003*, pages 246–247, Oct. 2003.

[50] S. Haese, C. Moullec, P. Coston, and K. Sayegrih. High-resolution spread spectrum channel sounder for wireless communications systems. In *IEEE International Conference on Personal Wireless Communication*, pages 170–173, Feb. 1999.

[51] R. Cosquer. *Conception d'un sondeur de canal MIMO Caractérisation du canal de propagation d'un point de vue directionnel et doublement directionnel*. PhD thesis, INSA Rennes, Rennes, France, 2004.

[52] J. M. Albornoz. A wideband channel sounder. Master's thesis, Graduate School of The Ohio State University, 2001.

[53] V. Y. Vu. *Conception et réalisation d'un sondeur de canal multi-capteur utilisant les corrélateurs cinq-ports pour la mesure de propagation à l'intérieur des bâtiments*. PhD thesis, Ecole Nationale Supérieure des Télécommunications, Paris, France, 2005.

[54] P. F. Wilson, P. B. Papazian, M. G. Cotton, Y. Lo, and S. C. Bundy. Simultaneous wide-band four-antenna wireless channel-sounding measurements at 1920 mhz in a suburban environment. *IEEE Trans. on Vehicular Technology*, 50(1):67–78, Jan. 2001.

[55] P. Truffer and P. E. Leuthold. Wide-band channel sounding at 24 ghz based on a novel fiberoptic synchronization concept. *IEEE Transactions on Microwave Theory and Techniques*, 49(4):692–700, April 2001. Part 1.

[56] J. Austin, W. P. A. Ditmar, W. K. Lam, and E. Vilar. A spread spectrum communications channel sounder. *IEEE Trans. On Communications*, 45(7):840–847, July 1997.

[57] P. F. Wilson, P. B. Papazian, M. G. Cotton, and Y. Lo. Advanced antenna test bed characterization for wideband wireless communications

systems. NTIA Report 99-369, Institute for Telecommunication Sciences, National Telecommunications and Information Administration, U.S. Department of Commerce, Boulder, CO, Aug. 1999.

[58] L. Clavier, M. Rachdi, M. Fryziel, Y. Delignonand V. Le Thuc, C. Garnier, and P. A. Rolland. Wide band 60 ghz indoor channel: characterization and statistical modelling. volume 4, pages 2098–2102, Oct. 2001. VTC fall.

[59] M. H. C. Dias and G. L. Siqueira. Indoor 1.8 ghz aoa-tdoa measurements extending the use of a wideband propagation channel sounder with the synthetic aperture. In *35th European Microwave Conf.*, pages 1191–1194, Paris, France, Oct. 2005.

[60] V. Y. VU, A. J. Braga, B. Huyart, and X. Begaud. Joint toa/doa measurements for spatio-temporal characteristics of 2.4 ghz indoor propagation channel. In *35th European Microwave Conf.*, pages 47–50, Paris, France, Oct. 2005.

[61] G. L. Berger and H. Safer. Channel sounder for the tactical vhf-range. In *MILCOM 97*, pages 1474–1478, Nov. 1997.

[62] S. Salous, P. Fhilippidis, and I. Hawkins. A multi channel sounder architecture for spatial and mimo characterisation of the mobile radio channel. In *MIMO: Communications Systems from Concept to Implementations*. IEE Seminar, Dec. 2001.

[63] S. Salous and V. Hinostroza. Bi-dynamic indoor measurements with high resolution channel sounder. In *The 5th International Symposium*

on Wireless Personal Multimedia Communications, pages 262–266, Oct 2002.

[64] RUSK channel sounder. A system for wide band measurement in radio channels. http://www.vadgmbh.de/english/rusk_e.htm. VAD Video-Audio-Design GmbH - Dresden, Germany. Seen in 05, 21 2006.

[65] J. M. Conrat, J. Y. Thiriet, and P. Pajusco. Americc, the france télécom r&d wideband propagation channel sounder from 2 to 60 ghz. Td(03)003, COST 273, Barcelone, Spain, Jan. 2003.

[66] H. Krim and M. Viberg. Two decades of array signal processing research. *IEEE Signal Processing Magazine*, 13(4):67–94, July 1996.

[67] B. H. Fleury, M. Tschudin, R. Heddergott, D. Dahlhaus, and K. L. Pedersen. Channel parameter estimation in mobile radio environments using the sage algorithm. *IEEE Journal on Selected Areas in Communications*, 17(3):434–450, Mar. 1999.

[68] H. Mewes. Practical comparisons between various high resolution spectral estimation algorithms for radio direction finding. In *9th International Conference on Antennas and Propagation*, volume 1, pages 480–483, Apr. 1995.

[69] A. Paulraj, R. Roy, and T. Kailath. A subspace rotation approach to signal parameter estimation. *Proceedings of the IEEE*, 74(7):1044–1046, July 1986.

[70] R. Roy and T. Kailath. Esprit-estimation of signal parameters via rotational invariance techniques. *IEEE Transactions on Acoustics, Speech, and Signal Processing*, 37(7):984–995, July 1989.

[71] A. Lee. Centrohermitian and skew-centrohermitian matrices. *Linear Algebra Applicat.*, 29:205–210, 1980.

[72] M. Haardt and J. A. Nossek. Unitary esprit: How to obtain an increased estimation accuracy with a reduced computational burden. *IEEE Trans. on Signal Processing*, 43:1232–1242, May 1995.

[73] P. Stoica and A. Nehorai. Performance comparison of subspace rotation and music methods for direction estimation. *IEEE Trans. on Signal Processing*, 39(2):446–453, Feb. 1991.

[74] P. Stoica and T. Soderstrom. Statistical analysis of music and subspace rotation estimates of sinusoidal frequencies. *IEEE Trans. on Signal Processing*, 39(8):1836–1847, Aug. 1991.

[75] E. Lin, L. Bai, and M. Kam. Efficient doa estimation method employing unitary improved polynomial rooting. In *IEEE International Conference on Acoustics, Speech, and Signal Processing*, volume 2, pages 257–260, May 2004.

[76] V. C. Soon and Y. F. Huans. An analysis of esprit under random sensor uncertainties. *IEEE Trans. on Signal Processing*, 40:2353–2358, 1992.

[77] E. M. Al-Ardi, R. M. Shubair, and M. E. Al-Mualla. Investigation of high-resolution doa estimation algorithms for optimal performance of

smart antenna systems. In *4th International Conference on 3G Mobile Communication Technologies*, pages 460–464, June 2003.

[78] B. Ottersten, M. Viberg, and T. Kailath. Performance analysis of the total least squares esprit algorithm. *IEEE Trans. on Signal Processing*, 39(5):1122–1135, May 1991.

[79] X. L. Xu and K. M. Buckley. Bias analysis of the music location estimator. *IEEE Trans. on Signal Processing*, 40:2559–2569, 1992.

[80] Z. Yong and F. Zhenghe. Direction-of-arrival estimation with wavelet-based spatial filtering. In *2nd International Conference on Microwave and Millimeter Wave Technology*, pages 687–690, Sept. 2000.

[81] C. Zhou, F. Haber, and D. L. Jaggard. A resolution measure for the music algorithm and its application to plane wave arrivals contaminated by coherent interference. *IEEE Trans. on Signal Processing*, 39:454–463, 1991.

[82] M. Kaveh and A. J. Barabell. The statistical performance of music and mini-norm algorithms in resolving plane wave in noise. *IEEE Trans. on Acoust., Speech, Signal Processing*, ASSP-34:331–341, 1986.

[83] S. L. Marple Jr. Frequency resolution of fourier and maximum entropy spectral estimates. *Geophysics*, 47(9):1303–1307, Sept. 1982.

[84] H. Akaike. A new look at the statistical model identification. *IEEE Trans. on Automat. Contr.*, AC-19:716–723, 1974.

[85] E. Fishler and H. V. Poor. Estimation of the number of sources in unbalanced arrays via information theoretic criteria. *IEEE Transactions on Signal Processing*, 53(9):3543–3553, Sept. 2005.

[86] A. B. Gershman and V. T. Ermolaev. Optimal subarray size for spatial smoothing. *IEEE Signal Processing Letters*, 2(2), Feb. 1995.

[87] H. Yamada, M. Ohmiya, Y. Ogawa, and K. Itoh. Superresolution techniques for time-domain measurements with a network analyzer. *IEEE Trans. on Antennas and Propagation*, 39:177–183, Feb. 1991.

[88] C. A. Tan, A. R. Nix, and M. A. Beach. Dynamic spatial-temporal propagation measurement and super-resolution channel characterisation at 5.2 ghz in a corridor environment. In *IEEE 56th Vehicular Technology Conference*, volume 2, pages 797–801, Sept. 2002.

[89] A. J. Levy. Fine structures of the urban mobile propagation channel. In *Commsphere*, pages 5.1.1–5.1.6., Herzliya, Israel, Dec. 1991.

[90] P. A. Matthews and B. Mohebbi. Direction of arrival measurements at uhf. *Electron. Lett.*, 25(16):1069–1070, Aug. 1989.

[91] M. Haardt, M. D. Zoltowski, C. P. Mathews, and J. A. Nossek. 2-d unitary esprit for efficient 2-d parameter estimation. In *IEEE International Conference on Acoustics, Speech and Signal Processing*, pages 2096–2099, May 1995.

[92] J. Fuhl, J.-P. Rossi, and E. Bonek. High-resolution 3-d direction-of-arrival determination for urban mobile radio. *IEEE Trans. on Antennas and Propagation*, 45(4):672–682, April 1997.

[93] A. J. Braga, Y. V. Vu, B. Huyart, and J. C. Cousin. Wideband spatio-temporal channel sounder using music and enhanced 2d-ss. In *European Conference Propagation and Systems*, Brest, France, Mar. 2005.

[94] D. H. Johnson and D. E. Dudgeon. *Array signal processing: Concepts and techniques*. Prentice-Hall, Englewood Cliffs, NJ, 1993.

[95] G. Wölfle, R. Wahl, P. Wildbolz, P. Wertz, and F. Landstorfer. Dominant path prediction model for indoor and urban scenarios. Td(04)205, COST 273, Duisburg, Germany, Sep. 2004.

[96] H. S. Kim. *Measurement and model based characterization of indoor wireless channels*. PhD thesis, University of Massachusetts Lowell, Lowell, MA, 2003.

[97] S. O. Tatu, E. Moldovan, K. Wu, and R. G. Bosisio. A new direct millimetre-wave six-port receiver. *IEEE Trans. on Microwave Theory Tech.*, 49(12):2517–2522, Dec. 2001.

[98] G. Neveux, B. Huyart, and J. R. Guisantes. Wide-band rf receiver using the "fiveport" technology. *IEEE Trans. on Vehicular Technology*, 53(5):1441–1451, Sept. 2004.

[99] S. Abou Chakra. *La boucle locale radio et la démodulation directe de signaux larges bandes à 26 GHz*. PhD thesis, Ecole Nationale Supérieure des Télécommunications, Paris, France, 2004.

[100] J. Li, R. G. Bosisio, and K. Wu. A collision avoidance radar using six-port phase/frequency discriminator (spfd). In *IEEE National Telesystems Conf.*, pages 55–58, San Diego, CA, May 1994.

[101] F. R. de Sousa and B. Huyart. A reconfigurable high-frequency phase-locked loop. In *20th IEEE Instrumentation and Measurement Technology Conference*, volume 1, pages 503–507, May 2003.

[102] S. P. Yeo and F. C. Choong. Matched symmetrical five-port microstrip coupler. *IEEE Trans. on Microwave Theory and Techniques*, 49(8):1498–1500, Aug. 2001.

[103] E. Bergeault, G. Geneves, B. Huyart, and L. Jallet. The design of a six-port reflectometer with frequency-independent calibration procedure. In *Conference on Precision Electromagnetic Measurements*, pages 398–399, June 1990.

[104] F. Wiedmann. *Développements pour des applications grand public du réflectomètre six-portes : algorithme de calibrage robuste, réflectomètre à très large bande et réflectomètre intégré MMIC*. PhD thesis, Ecole Nationale Supérieure des Télécommunications, Paris, France, 1997.

[105] G. F. Engen and C. A. Hoer. Applicaton of an arbitrary 6-port junction to power measurement problems. *IEEE Trans. on Instrumentation and Measurement*, IM-21:470–474, Nov. 1972.

[106] S. A. Chahine, B. Huyart, and G. Neveux. An accurate model of five-port reflectometer. In *34th European Microwave Conference*, volume 2, pages 549–552, Oct. 2004.

[107] C. G. Montgomery, R. H. Dicke, and E. M. Purcell. *Principles of microwave circuits*. Peregrinus, London, U.K., 1987.

[108] Agilent technologies. *Impedance matching techniques for mixers and detectors*. Application Note 963.

[109] A. M. Cowley and H. O. Sorensen. Quantitative comparison of solid-state microwave detectors. *IEEE Trans. on Microwave Theory Tech.*, 14:588–602, Dec. 1966.

[110] C. Potter and A. Bullock. Non linearity correction of microwave diode detectors using a repeatable attenuation step. *Microwave Journal*, 36(5):272–279, May 1983.

[111] F. R. de Sousa, B. Huyart, S. Y. C. Catunda, and R. N. de Lima. A to d converters and look-up tables dimensioning for five-port reflectometer based systems. In *20th IEEE Instrumentation and Measurement Technology Conference*, volume 1, pages 743–747, May 2003.

[112] A. Alexiou and M. Haardt. Smart antenna technologies for future wireless systems: trends and challenges. *IEEE Communications Magazine*, 42(9):90–97, Sep. 2004.

[113] W. Li, X. Huang, and H. Leung. Performance evaluation of digital beamforming strategies for satellite communications. *IEEE Trans. on Aerospace and Electronic Systems*, 40(1):12–26, Jan. 2004.

[114] Phased-array antenna systems. http://www.appliedradar.com/. Applied Radar Inc., N. Kingstown, RI. Seen in 09, 01 2006.

[115] V. Hattenberger. *Contribution à l'étude de la formation de vois en numérique: Application à la concéption de récepteurs haut débit utilisant des antennes planaires à rayonnement direct.* PhD thesis, Ecole Polytechnique de l'Université de Nantes, Nantes, 2005.

[116] Y. Zhang, Z. Bao, L. Zhang, and G. Liao. Joint acquisition of pn code and adaptive beamforming weight in spread spectrum systems. *Electronics Letters*, 40(1):52–53, Jan. 2004.

[117] S. A. Jafar and A. Goldsmith. Beamforming capacity and snr maximization for multiple antenna systems. In *IEEE 53rd Vehicular Technology Conference*, volume 1, pages 43–47, May 2001.

[118] V. C. Anderson. Dicanne, a realizable adaptive process. *The Journal of the Acoustical Society of America*, 45(2):398–405, Feb. 1969.

[119] L. C. Godara. *Smart antennas.* CRC Press, Boca Raton, FL, 2004.

[120] J. Butler and R. Lowe. Beam-forming matrix simplifies design of electronically scanned antennas. *Electronic Design*, pages 170–173, Apr. 1961.

[121] J. Blass. Multidirectional antenna: A new approach to stacked beams. In *IRE International Conference Record*, volume 8, 1960. Part 1.

[122] O. L. Frost. An algorithm for linearly constrained adaptive array processing. *proc. IEEE*, 60:926–935, Aug. 1972.

[123] L. J. Griffiths and C. W. Jim. An alternative approach to linearly constrained adaptive beamforming. *IEEE Trans. on Antennas and Propagation*, AP-30:27–34, Jan. 1982.

[124] P. W. Howells. Explorations in fixed and adaptive resolution at ge and surc. *IEE Trans. on Antennas and Propagation*, Ap-24(5):575–584, Sep. 1976.

[125] C. W. Jim. A comparison of two lms constrained optimal array structures. *Proc. IEEE*, 65(12):1730–1731, Dec. 1977.

[126] B. Van Veen and R. Roberts. Partially adaptive beamformer design via output power minimization. *IEEE Trans. on Acoustics, Speech, and Signal Processing*, 35(11):1524–1532, Nov. 1987.

[127] S. Haykin. *Adaptive filter theory.* Information and system sciences. Prentice Hall, Upper Saddle River, NJ, fourth edition, 2002.

[128] B. Widrow et al. Adaptive noise cancelling: Principles and applications. *Proc. IEEE*, 63(12):1692–1716, Dec. 1975.

[129] R. G. Vaughn. On optimum combining at the mobile. *IEEE Trans. on Vehicular Technology*, 37(4):181–188, Nov. 1988.

[130] C. Braun, M. Nilsson, and R. D. Murch. Measurement of the interference rejection capability of smart antennas on mobile telephones. In *IEEE 49th Vehicular Technology Conference*, volume 2, pages 1068–1073, May 1999.

[131] C. B. Dietrich Jr. *Adaptive arrays and diversity antenna configurations for handheld wireless communication terminals*. PhD thesis, Faculty of the Virginia Polytechnic Institute and State University, Blacksburg, VA, 2000.

[132] H. Steyskal. Digital beamforming antenna, an introduction. *Microwave J.*, pages 107–124, Jan. 1987.

[133] B. Van Veen and K. M. Buckley. Beamforming: a versatile approach to spatial filtering. *IEEE ASSP Magazine*, 5(2):4–24, April 1988.

[134] I. S. Reed, J. D. Mallett, and L. E. Brennan. Rapid convergence rate in adaptive arrays. *IEEE Trans. on Aerosp. Electron. Syst.*, AES-10:853–863, 1974.

[135] L. E. Brennan and I. S. Reed. Theory of adaptive radar. *IEEE Trans. on Aerosp. Electron. Syst.*, AES-9:237–252, 1973.

[136] F. Ares, R. S. Elliot, and E. Moreno. Optimised synthesis of shaped line-source antenna beams. *Electronics Letters*, 29(12):1136–1137, June 1993.

[137] C. J. V. der Maas. A simplified calculation for dolph-chebyshev arrays. *Journal of Applied Physics*, 25:121–124, Jan. 1954.

[138] R. C. Hansen. *The handbook of antenna design.* Peter Peregrinus, London, U.K., 1983.

[139] A. J. Braga, V. Y. Vu, B. Huyart, and J. C. Cousin. Beamforming system using five-port discriminators. In *35th European Microwave Conf.*, pages 165–168, Paris, France, Oct. 2005.

[140] W. R. Deal et al. A new quasi-yagi antenna for planar active antenna arrays. *IEEE Trans. on Microwave Theory Tech.*, 48(6):910–918, June 2000.

[141] Y. Qian, W.R. Deal, N. Kaneda, and T. Itoh. Microstrip-fed quasi-yagi antenna with broadband characteristics. *Electronic Letters*, 34(23):2194–2196, Nov. 1998.

[142] Y. Qian, W. R. Deal, N. Kaneda, and T. Itoh. A uniplanar quasi-yagi antenna with wide bandwidth and low mutual coupling characteristics. In *IEEE Antennas and Propagation Society International Symposium*, volume 2, pages 924–927, July 1999.

[143] Hittite Microwave Corporation, Chelmsford, MA. *HMC287MS8 - GaAs MMIC Low Noise Amplifier with AGC, 2.3 - 2.5 GHz.*

[144] G. Neveux, B. Huyart, and J. Rodriguez. Noise figure of a five-port system. In *32nd European Conference on Wireless Technology*, Milan, Italy, Sep. 2002.

[145] A. Braga and G. Cavalcante. Theoretical analysis of a uhf channel in a street city modeled as a deterministic multislit waveguide.

In *SBMO/IEEE MTT-S International Microwave and Optoelectronics Conference*, volume 1, pages 421–424, Aug. 2001.

List of Publications

- Measurement of Direction-of-Arrival of coherent signals using Five-Port reflectometers and quasi-Yagi antennas, Van Yem Vu, A. Judson Braga, Xavier Begaud, Bernard Huyart. IEEE Microwaves and Wireless Component Letters, VOL. 15, NO. 9, September 2005.

- Beamforming system using Five-Port discriminators, A. J. Braga, V. Y. Vu, B. Huyart, and J. C. Cousin, European Microwave Conf. 2005 - Paris.

- Joint TOA/DOA measurements for spatio-temporal characteristics of 2.4 GHZ indoor propagation channel, Van Yem Vu, A. Judson Braga, Bernard Huyart and Xavier Begaud, ECWT 2005 - Paris.

- Smart antennas using Five-Port reflectometer, A. Judson Braga, Van Yem Vu, Bernard Huyart, and J. C. Cousin, IMOC 2005 - Brasilia.

- Wideband spatio-temporal channel sounder using MUSIC and enhanced 3D-SS, A. Judson Braga, Yem Van Vu, Bernard Huyart, and J. C. Cousin, ECPS 2005 - Brest.

- Narrow band direction of arrival measurement using Five-Port reflectometers and quasi-Yagi antennas, Van Yem Vu, A. Judson Braga, Bernard Huyart and Xavier Begaud, ECPS 2005 - Brest.

- Direction of arrival and time delay measurements for multi-path signals using Five-Port reflectometers, Van Yem Vu, A. Judson Braga, Xavier Begaud and Bernard Huyart, APS 2005 - Washington.

- Système de formation de faisceaux utilisant des réflectomètres Cinq-Port, A. Judson Braga, Van Yem Vu, Bernard Huyart, et J. C. Cousin, 14èmes Journées Nationales Microondes 2005 - Nantes.

- Estimation des directions d'arrivée et des retards de propagation par utilisation de la technique Cinq-Port, Van Yem Vu, A. Judson Braga, Xavier Begaud et Bernard Huyart, 14èmes Journées Nationales Microondes 2005 - Nantes.

- Results on DoA finding system based on Five-Port discriminator, A. Judson Braga, V. Yem Vu, Bernard Huyart, and X. Begaud, International Microwave Symposium 2004 - Fort Worth Texas.

- Calibração de um arranjo linear de antenas para estimação de direção de chegada, A. Judson Braga, Gervásio P. S. Cavalcante, Van Yem Vu e Bernard Huyart, XXI Simpósio Brasileiro de Telecomunicações 2004, Belém - Brasil.

- Calibration of frequency propagation channel sounder based on a Five-Port reflectometer, Van Yem Vu, A. Judson Braga, B. Huyart, X. Be-

gaud, F. R de Sousa and Bich Huyen Nguyen, ICEIC 2004 - Hanoi Vietnam.

- Multi-path delay measurement based on Five-Port discriminator, Van Yem Vu, A. Judson Braga, Xavier Begaud and Bernard Huyart, ECWT 2004 - Amsterdan.